Università degli Studi di Udine
Dipartimento di Ingegneria Elettrica,
Gestionale e Meccanica
Dottorato di Ricerca in Ingegneria Elettronica

Ph.D. Thesis

Numerical and experimental methods for the comparison of radiated immunity tests in EMC sites

Candidate
Matteo Cicuttin

Supervisors
Prof. Ruben Specogna
Prof. Francesco Trevisan

Cycle XXVIII — A.Y. 2014-2015

Institute Contacts
Dipartimento di Ingegneria Elettrica, Gestionale e Meccanica
Università degli Studi di Udine
Via delle Scienze, 206
33100 Udine — Italia
+39 0432 558400
http://www.diegm.uniud.it/

Author's Contacts
matteo@matteocicuttin.it

To my grandfather Anselmo,
who definitely helped the seed of the curiosity grow inside me. We all miss you.

Acknowledgements

In the acknowledgements of my master thesis I expressed the hope to have a career that allowed me to continue studying and researching new things, and this thesis definitely represents a huge milestone towards my hopes. However, these hopes would have been much much harder to pursue without all the people that during the three years of my Ph. D. studies supported me and encouraged me in going along this path, so I would like to say an huge "thank you" to all of them.

In particular, I would like to express my gratitude to my supervisors prof. Ruben Specogna and prof. Francesco Trevisan for giving me the immense opportunity of a Ph. D. and for supporting me during the last three years. During that time I learned a lot from them.

I would like also to thank two other people I worked with: Antonio Affanni, for all the hints and the advices he gave to me, and Lorenzo Codecasa, for all the useful discussions I had with him.

Emilab also had a huge role in this doctorate, and granted me great support and resources to pursue my goals. Ing. Silvano Chialina, Ing. Giovanni Solari and all the other people there always had time to help me and to explain me the current best practices in the complex field of the electromagnetic compatibility testing. For this I would like to thank them and to express my gratitude to them.

Thank you to prof. Piergiorgio Alotto and prof. Christophe Geuzaine for the time they dedicated to the review of my thesis and for their comments. Moreover, I would like to thank prof. Geuzaine for his hospitality at University of Liège: I really had a great time there.

During the years I spent at the University of Udine I met some good friends with whom I spent many good times. Nicola, who is always one step ahead of us mere mortals when the topic of the discussion is the C++ language (and software development in general), Luca, who is THE computer security guy (and who hosts `ns2.fuffakiller.it`), and Bernard, who is both a good colleague and a nice person to spend time with (together with Schroedinger and the 903).

I had lot of fun – and a lot of Americani – with the Vi.Ci.Na.Ti.: Riccardo, who always complained for me being late at any appointment, Francesca, with whom I had some instructive discussions about integrals and integration and Laura, who initially was not too sure that we could become friends but at the end she even invited me at her wedding (not as husband, fortunately!). I didn't only have fun with them, they also were always there during difficult times.

I deserve gratitude to my old-time friends Omar and Nicoletta, for their support, for their friendliness and for everything.

Of course, the biggest thanks go to my family, who supported me during all the years

of the university, and to Samantha, for all the wonderful moments we had together. Moreover, I would like to thank her for all the energy she spent (many megajoules) the last two years to keep me focused on the right things and to distract me from the bad ones.

Finally I want to say thank you *again* to the teachers I had at the high school: much of the knowledge and the mindset they gave to me was of primary importance for my doctorate.

Abstract

Electromagnetic compatibility plays a central role in today's manufacturing of electronic products. Unintended radiation by one device could produce various effects on other devices, ranging from innocuous to very dangerous. On the other hand, insufficient immunity to RF energy can cause malfunctions and interruptions in device operation. For these reasons in the past decades lots of regulatory directives were compiled to help manufacturers in producing better-performing devices in terms of electromagnetic compatibility.

The "compatibility" of a product is verified in specific laboratories, where testing is divided in radiated immunity, radiated emissions, conducted immunity and conducted emissions. The first two kinds of tests are about disturbances propagating "in air", while the last two kinds are about disturbances propagating via connecting cables.

Despite being of fundamental importance, neither regulations nor testing provide perfect receipts to build compatible devices; moreover testing needs to be done by means of carefully prepared experiments performed in sites whose performance is well known. Being composed by an anechoic chamber, cables, antennas, receivers and other instrumentation, a site is usually quite complex and it can be difficult to control all the involved variables.

This thesis, which is focused on the radiated part of testing, proposes a novel numerical method useful to predict the performance of electrically large anechoic chambers, a topic currently subject of significant research. The method is based on the concept of *equivalent models*, which allow to substitute complex objects with simpler ones. The subjects of the equivalent modeling are the antennas and the walls of the anechoic chamber, which are the most complex objects from the point of view of the geometry in this kind of simulation and which could heavily impact on its computational requirements. The aim of the proposed technique is to be a complement to the measurements usually made to evaluate the performance of anechoic sites. Since this kind of measurements is very tricky and a misplaced cable could be source of problems, using simulations measurements can be cross-checked against a numerical model, so a laboratory can be more confident about its procedures and its results.

The developed theory and models would be useless without a confirmation of their functionality and applicability, so the thesis includes also an experimental part carried out at Emilab in Amaro. An extensive set of measurements was made in their anechoic chambers to compare with the predictions of the numerical models and to confirm the plausibility of the results.

Finally, the numerical scheme is part of a purpose-built software that allows to simulate quite big sites on rather modest hardware.

Contents

List of Figures

I

Preliminaries

1

Introduction

Every electric device radiates electromagnetic waves as a consequence of its functioning and this fact could produce various effects on other devices, ranging from innocuous to very dangerous. In the recent history, lots of accidents happened because of overlooked electromagnetic compatibility (EMC) issues. Particularly significant events include plane and car crashes due to external signals interfering with on board electronics [NAS95]. Information processing is also concerned with EMC: it is known from the sixties that computers radiate electromagnetic waves that carry signals allowing remote attackers to recover confidential information and cryptographic keys [VE85, Smu90, Age07]. On smaller scales, some devices we use every day are frequently subject to electromagnetic compatibility issues: common examples are microwave ovens disrupting Wi-Fi networks and cellular phones disturbing audio equipment. All those examples highlight the fact that EMC testing is a crucial step in the development of any kind of electronic product.

EMC testing is done in specific labs and usually is divided in two branches, namely *radiation* and *immunity*. Radiation is concerned about the unintentional emissions by devices, while immunity is about the verification of the behavior of a device when irradiated with an electromagnetic field. Aviation, automotive, marine and household devices are all subject to specific directives that prescribe which tests must be done, how, and which are the required immunity levels and the allowed emission levels. Tests consist mostly of measurements that are required to be accurate and repeatable. Accuracy and repeatability are obtained through standardized procedures, carefully controlled measurement conditions and comparisons between multiple laboratories [CBC$^+$14, ISO05].

In the previous discussion two actors are identified, namely the *product manufacturer* and the *test laboratory*. The product manufacturer is required to comply with regulations applicable to its product, but there are no recipes that help him to meet the required standards. Moreover, lab time needed to debug the products found to be non-compliant can be very costly. The test laboratory, on the other hand, needs to be sure about the efficiency of its measurement chain and must be confident about the correctness of the implemented procedures.

Simulation can be a tool helping both the manufacturer and the laboratory with these

issues. The manufacturer can waste less time in debugging and optimize its product with simulation. The laboratory, on the other hand, can do some predictions on the performance of its measurement site and the accuracy of its measurements.

In the recent years the availability of cheap computational power allowed to do the most disparate kinds of numerical simulations. In particular, simulation of anechoic chambers is an attractive topic, since if done correctly it can provide useful data about the site [JY07, Swa08, NSAA09, MK14]. However, the nature of the problem makes its solution particularly challenging: the matrices arising from the discretization of such sites are indefinite and thus iterative solvers are ruled out even if clever preconditioners are employed, making direct solvers the only viable choice. This, in turn, allows the simulation of only electrically small sites (large chambers but at low frequency or small chambers at high frequency) because of the huge memory requirement of this kind of solvers.

1.1 Aims of the thesis

This thesis tries to address the problem of the simulation of electrically large chambers. This objective is pursued in three phases:

- *Extension of the DGA with the tools needed for wave propagation simulation.* DGA is a rather new scheme to solve the PDEs arising from physics. The research presented in this thesis needed a numerical tool to be used as development environment and, despite tens of commercial simulators are available, they have huge costs and are closed-source, so it is impossible to modify them to integrate the developed numerical models. A new numerical code was then developed and DGA was chosen because of the huge expertise of the Udine research group in this method. Some theoretical tools needed to be developed to do high frequency simulations, the most important ones being the plane wave source and the waveguide port. These theoretical developments extended the features available in the existing DGA framework.
- *Development of numerical models and procedures that allow the simulation of large chambers.* As already mentioned, simulation of large chambers is a challenging task. This thesis proposes a novel approach useful to reduce the computational resources required for this kind of simulations by means of equivalent elements, especially equivalent walls and equivalent antennas.
- *Validation of the developed models against measurements performed in a real site.* The main goal of the numerical models presented in this thesis is doing accurate predictions of real measurement, and the third phase covers this topic.

1.2 Structure of the thesis

The thesis is organized in seven chapters. After the introduction, the second chapter describes the DGA method by first reviewing the main literature and then by presenting the main ideas behind it. The spatial discretization is described and then the degrees of freedom are introduced. The discussion then continues with the description of the

discrete differential operators and the constitutive matrices. Finally, the Tonti diagram is introduced.

The third chapter is about the Maxwell's equations. After a brief review of the continuous equations, the discrete geometric equations are described and the discrete wave equation is derived. The chapter closes with a brief review of the problems that arise when solving the wave equation, which are also the problems that led to the research presented in this thesis.

The fourth chapter is about the numerical description of the electromagnetic sources. Plane wave source and equivalent antennas are the two main topics of the chapter and represent the foundation of the method proposed in this thesis.

In the fifth chapters two other formulations of the electromagnetic problem are presented and their features are discussed. In particular, H-field formulation is used to devise an adaptive mesh refinement scheme, while $\boldsymbol{A}$-V formulation is an alternative that can ease the application of voltage sources (i.e. connection of a RF generator to an antenna).

The simulation methods for electrically large anechoic chambers that were developed are discussed in the sixth chapter. The first part is devoted to discuss how to setup the simulations by means of equivalent elements. Then, the measurement setup is described and the comparison between measurements and simulations is presented. Finally, the results are interpreted by taking in consideration all the measurement uncertainties.

The research was supported by a new, in-house developed numerical code. The seventh chapter describes briefly the main features of the code and gives some insights in its inner workings.

1.3 Contributions

The work presented in this thesis was the subject of the following five publications:

- *Plane Wave Excitation for Frequency Domain Electromagnetic Problems by Means of Impedance Boundary Condition*; S. Chialina, M.Cicuttin, L. Codecasa, R. Specogna, F. Trevisan; IEEE Transactions on Magnetics, vol. 51, no. 3, March 2015,
- *Complementary discrete geometric h-field formulation for wave propagation problems*; M. Cicuttin, L. Codecasa, R. Specogna, F. Trevisan; IEEE Transactions on Magnetics, vol. 52, no. 3, March 2016.
- *Excitation by scattering/total field decomposition and Uniaxial PML in the geometric formulation*; M. Cicuttin, L. Codecasa, R. Specogna, F. Trevisan; IEEE Transactions on Magnetics, vol. 52, no. 3, March 2016.
- *Fast uncertainty quantification of fields and global quantities*; A. Affanni, M. Cicuttin, R. Specogna, F. Trevisan; Proceedings of the COMPUMAG 2015 conference, CMP-358.
- *Modeling of anechoic chambers with equivalent materials and equivalent sources*; S. Chialina, M.Cicuttin, L. Codecasa, G. Solari, R. Specogna, F. Trevisan; IEEE Transactions on Electromagnetic Compatibility; in press.

2

Introduction to the Discrete Geometric Approach

The Discrete Geometric Approach (DGA) is a rather recent numerical technique for the solution of partial differential equations arising from physical problems, which is gaining wide acceptance in the last years. The first section of this chapter is devoted to a review of the literature relevant to the DGA, while the second part contains a general overview of the method.

2.1 Literature survey

The theory underlying the DGA has its roots in the works of Tonti [Ton75] and Bossavit [Bos98b], where the authors investigate a deep connection between physics on one hand and geometry and topology on the other. This connection led Tonti to ask himself "*Why starting from differential equations for computational physics?*" [Ton14] and to develop the *finite formulation* of computational physics. The finite formulation is based on a classification, proposed by Tonti, of the physical quantities and the equations of every physical theory. He noted that physical quantities fall into three categories: the *source variables*, which account for "the causes" of a physical phenomena, the *configuration variables*, which account for "the effects" and the *energetic variables*, the last arising from the product of the first two. Moreover, two kinds of relations are encountered: the *balance equations*, which encode the topology of the problem and the *constitutive relations*, which encode the metric of the problem.

Instead of discretizing the differential equations, the finite formulation relies on algebraic equations to describe a physical phenomena. This setting has the notable advantage that the theory is directly translated to both a numerical scheme (the *Cell Method* [Ton01]) by writing the equations in matrix form and solving them with a computer, and to differential equations by means of a limit operation.

After the seminal works of Bossavit and Tonti, a multitude of methods sharing the same fundamental properties arose – for example FIT from Weiland [Wei01] and

DGA from Trevisan and Codecasa [CT05] – but each one addressing specific features. Moreover, geometric interpretation was given to already existing methods: notable contributes in this field were given by Bossavit, with his Generic Finite Difference method [Bos01] and Trevisan and Kettunen [TK06]. In addition, Mattiussi [Mat97] analyzed Finite Elements, Finite Volumes and Finite Differences and, using notions from algebraic topology, pointed out the similarities between them.

The numerical models discussed in this thesis were developed in the context of the DGA. DGA inherits the concepts behind the original Cell Method and extends it in many ways, thanks to the contributions given by Codecasa, Specogna and Trevisan. They initially proposed piecewise uniform basis functions and constitutive matrices for tetrahedral [CT05, CST07] and hexahedral meshes [CS08, CST10b, CDST10]. These constitutive matrices have the remarkable properties of being symmetric, positive definite and consistent: all the previous approaches to constitutive matrices failed at having all the three properties at the same time [Hol83, SW98, TKB99, SSW02]. A new piece was added to DGA in [CST12], where the *Admittance Boundary Condition* was introduced by using *boundary dual grids*. Boundary dual grids offer an easy and clean way, which was then formalized by Codecasa in [Cod14], to deal with boundary and interface conditions. The admittance condition was further extended in [CCC$^+$15b], leading to a technique to apply plane wave excitation to simulations. Boundary grids allowed also the correct modeling of waveguide excitation's in presence of scattering objects near waveguide ports, as detailed in [CCST16b]. The last two works are two of the original contributions of this thesis.

In the past decades considerable effort has been expended in exploiting complementarity of electromagnetic problems for a number of purposes, in particular for adaptive mesh refinement [RBF88, GTB94, Spe10]. Notable results were obtained with static field problems, where bilateral energy bounds are established [Syn57]. DGA offers a particularly convenient setting for the study of complementary formulations and, in the recent years, major contributes regarding complementarity in electrostatics and eddy currents were given by Specogna in [Spe10, Spe13, Spe15, SST08, ST08, DS10]. A wide literature exists about complementarity in eddy current problems but, in this last class of problems, no energy bounds can be established despite they are frequently observed in practical problems (see for example [RQ10]). Complementarity in wave propagation problems, finally, seems to have received far less attention. A bibliographic research on the subject surprisingly gave very few results, as it appears that the only literature available on the subject is from Bossavit [GTB94, Bos98a]. Moreover, Bossavit studies a problem regarding a resonant cavity, which is quite specific. Some contributes regarding complementary in wave propagation were given in [CCST16a] and are covered in Chapter 5.

2.2 Spatial discretization

Differential formulation is based on coordinate systems that associate tuples of numbers to points in space. In this formulation, physical variables are functions *of the point* and thus coordinates allow to relate points in space with the value of the physical field variables. Finite formulation takes a completely different approach: it starts by observing that (1) physical quantities are associated not only to points, but also to other

geometrical entities which are lines, surfaces and volumes and (2) measurements involve *global* quantities.

Definition 1. *Global variables are those physical quantities that are* not *line densities, surface densities or volume densities of other variables.*

The way a quantity is measured leads to make a natural association between the quantity itself and the geometric element on which it is measured. Electromotive force (EMF), for example, is defined to be the line integral of the electrostatic field between two points A and B and is measured by connecting the terminals of a voltmeter to the endpoints A and B of the line; EMF is then a quantity associated to lines. Similarly, electric current is naturally associated to surfaces because it is defined to be the quantity of charge that flows across a surface in a given period of time, and the flow is measured with an amperometer. At this point we could be tempted to think to the expression "global variable" as a synonym of "integral variable", but this is not the case: the potential, for example, is not an integral quantity, however is a global variable because it is not a density of some other variable. Global variables finally are associated to spatial locations by their *support*, which in some way plays the same role of the coordinate system in the continuous domain. The support is given by an appropriate spatial discretization in points, lines, surfaces and volumes obtained through a *primal grid* and a *dual grid*.

2.2.1 Primal grid

We denote as Ω the domain over which the problem is defined. The discretization of Ω is obtained with a grid $\mathcal{G}$ named *primal grid*. The grid can be a general polyhedral grid [CS08, CST10b, CDST10], but in this thesis the discretization of Ω is always achieved by means of *tetrahedral grids*. Tetrahedral meshes are a common choice for a number of reasons: fully automatic tetrahedral mesh generators are readily available (Gmsh, Netgen) and tetrahedral meshes are well suited for a large number of common practical problems. Whichever kind of mesh one chooses, the following definition can be given:

Definition 2. *A primal grid* $\mathcal{G} = \{\mathcal{N}, \mathcal{E}, \mathcal{S}, \mathcal{V}\}$ *is composed by the four sets* $\mathcal{N}$*,* $\mathcal{E}$*,* $\mathcal{S}$ *and* $\mathcal{V}$ *which contain the* nodes*, the* edges*, the* surfaces *and the* volumes *respectively.*

2.2.2 Dual grid

The dual grid $\tilde{\mathcal{G}}$ associated to the primal grid $\mathcal{G}$ is obtained – in the case of tetrahedral meshes – by the barycentric subdivision of the primal grid $\mathcal{G}$. The elements of $\tilde{\mathcal{G}}$ are obtained as follows:

- A *dual grid node* is identified as the barycenter of a primal grid volume. Given a generic volume $v_i \in \mathcal{G}(\mathcal{V})$, its associated dual grid node is denoted as $\tilde{n}_i \in \tilde{\mathcal{G}}(\tilde{\mathcal{N}})$. Note that there is 1-to-1 correspondence between the elements of $\mathcal{G}(\mathcal{V})$ and the elements of $\tilde{\mathcal{G}}(\tilde{\mathcal{N}})$.
- A *dual grid edge* connects two dual nodes. Let $v_i, v_j \in \mathcal{G}(\mathcal{V})$ be two adjacent volumes with the associated dual nodes $\tilde{n}_i, \tilde{n}_j \in \tilde{\mathcal{G}}(\tilde{\mathcal{N}})$. Moreover, let $f_k \in \mathcal{G}(\mathcal{S})$ be the surface that v_i and v_j have in common. The dual edge from n_i to n_j is

composed by the two segments that connect n_i with the barycenter of f_k and the barycenter of f_k with n_j. Note that there is 1-to-1 correspondence between the elements of $\mathcal{G}(\mathcal{S})$ and the elements of $\tilde{\mathcal{G}}(\tilde{\mathcal{E}})$;

- A *dual grid surface* is composed by the collection of the *facets* attached to the primal edge $e_i \in \mathcal{G}(\mathcal{E})$ that the volumes $v_h, \ldots, v_k$ have in common. Let $f_{a,h}, f_{b,h}$ be the primal faces of v_h attached to e_i: a facet of v_h attached to the edge e_i is the surface enclosed by
  - the segment from the barycenter of e_i to the barycenter of $f_{a,h}$
  - the segment from the barycenter of $f_{a,h}$ to the barycenter of v_h
  - the segment from the barycenter of v_h to the barycenter of $f_{b,h}$
  - the segment from the barycenter of $f_{b,h}$ to the barycenter of e_i

  Facets have the remarkable property of being planar. Moreover, elements of $\mathcal{G}(\mathcal{E})$ and the elements of $\tilde{\mathcal{G}}(\tilde{\mathcal{S}})$ are in 1-to-1 correspondence;
- A *dual grid volume* is defined as follows. Consider the cluster of primal volumes $v_h, \ldots, v_k$ sharing the node n_i. Each primal volume is subdivided by the facets in 4 distinct sub-volumes: the collection of sub-volumes attached to n_i form the dual volume. Note that there is 1-to-1 correspondence between the elements of $\mathcal{G}(\mathcal{N})$ and the elements of $\tilde{\mathcal{G}}(\tilde{\mathcal{V}})$.

Definition 3. *A dual grid $\tilde{\mathcal{G}} = \{\tilde{\mathcal{N}}, \tilde{\mathcal{E}}, \tilde{\mathcal{S}}, \tilde{\mathcal{V}}\}$ is composed by the four sets $\tilde{\mathcal{N}}$, $\tilde{\mathcal{E}}$, $\tilde{\mathcal{S}}$ and $\tilde{\mathcal{V}}$ which contain the* dual nodes*, the* dual edges*, the* dual surfaces *and the* dual volumes *respectively, obtained as prescribed by the barycentric subdivision procedure detailed above.*

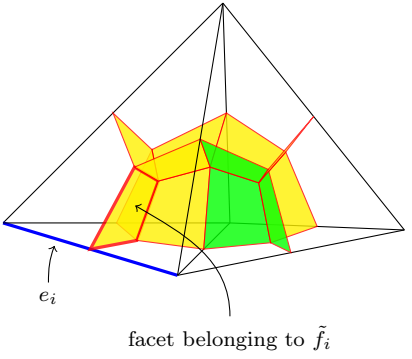

Figure 2.1: The barycentric subdivision of two adjacent tetrahedral volumes. The bold edge e_i and the facet with bold boundary are in 1-to-1 correspondence. The same facet is part of the dual face $\tilde{f}_i$ attached to the primal edge e_i.

2.2.3 Spatial element orientation

Each geometric entity of $\mathcal{G}$ and $\tilde{\mathcal{G}}$ must be oriented, and this can be done in two ways: with *inner orientation* and with *outer orientation* [Ton00]. A geometric entity which

is oriented without taking in consideration its ambient space has inner orientation, otherwise it has outer orientation. For example, the inner orientation of a line is given by its tangent vector and indicates which is the direction of the movement along the line. The outer orientation is the direction of rotation around the line. For a surface, its inner orientation is given by the direction of movement along its boundary, while the outer orientation is given by its normal vector. Inner and outer orientation are linked together by the screw rule (Fig. 2.2).

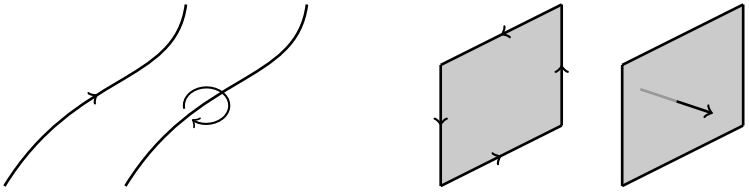

Figure 2.2: Inner and outer orientation of lines and surfaces. The same concepts can be extended to points and volumes.

We establish now an ordering convention for the geometric elements of a mesh (Fig. 2.3). The edges are oriented from the node with lower numbering to node with higher numbering. Faces have always two edges with same orientation: they set the inner orientation of the face. Moreover, faces are numbered as the opposite node: yellow face is f_2. Finally, the outer orientation of the primal faces is induced by their inner orientation using the screw rule.

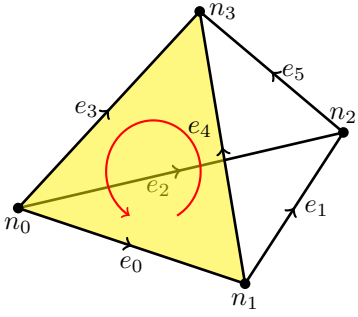

Figure 2.3: Conventional orientation of geometric elements on a tetrahedron.

Dual grid also needs to be oriented, and this is done by recurring to the 1-to-1 pairing between the elements of the two grids and to the two kinds of orientation. So for example, the outer orientation of a primal grid edge sets the inner orientation of the dual face it crosses, while the outer orientation of a primal face sets the inner orientation of the dual edge which crosses it. This process is known as *transfer of orientation.*

2.3 Degrees of freedom

When global variables are associated to the geometric elements of a mesh, they form the *degrees of freedom (DoFs)*. DoFs are obtained by evaluating the physical scalar or vector fields on the geometric elements of the mesh, and are collected in different finite-dimensional arrays of real or complex scalar values $\mathbf{X}_{\mathcal{G}(\mathcal{X})}$ of dimension $card(\mathcal{G}(\mathcal{X}))$, where $\mathcal{X} \in \{\mathcal{N},\ \mathcal{E},\ \mathcal{S},\ \mathcal{V}\}$ (when clear from the context, subscript $\mathcal{G}(\mathcal{X})$ will be omitted). Entries of these arrays are either functions of a point or quantities calculated by means of integration. To give a first idea, we anticipate the quantities of interest in electromagnetism. They can be summarized in the following list:

- Electric scalar potential V_i,
- Electromotive force, line integral of the electric field $\boldsymbol{E}$: $U_i = \int_{e_i} \boldsymbol{E} \cdot d\boldsymbol{l}$,
- Magnetic vector potential, line integral of $\boldsymbol{A}$: $A_i = \int_{e_i} \boldsymbol{A} \cdot d\boldsymbol{l}$,
- Magnetic flux, surface integral of the magnetic field $\boldsymbol{B}$: $\Phi_i = \int_{f_i} \boldsymbol{B} \cdot d\boldsymbol{S}$,
- Magnetomotive force, line integral of magnetic field $\boldsymbol{H}$: $F_i = \int_{\tilde{e}_i} \boldsymbol{H} \cdot d\boldsymbol{l}$,
- Electric flux, surface integral of the displacement field $\boldsymbol{D}$: $\Psi_i = \int_{\tilde{f}_i} \boldsymbol{D} \cdot d\boldsymbol{S}$,
- Electric current, surface integral of the current field $\boldsymbol{J}$: $I_i = \int_{\tilde{f}_i} \boldsymbol{J} \cdot d\boldsymbol{S}$,
- Charge, volume integral of the charge density ρ: $Q_i = \int_{\tilde{v}_i} \rho dv$.

As a convention, the generic degree of freedom X_i is attached to the i-th geometric entity (i.e. face) of the mesh and is also the i-th entry of the array $\mathbf{X}_{\mathcal{G}(\mathcal{X})}$. For example, U_i is the electromotive force attached to the i-th edge of the mesh, while the array $\mathbf{U}$ of dimension $card(\mathcal{G}(\mathcal{E}))$ collects all the electromotive forces attached to the edges of the mesh.

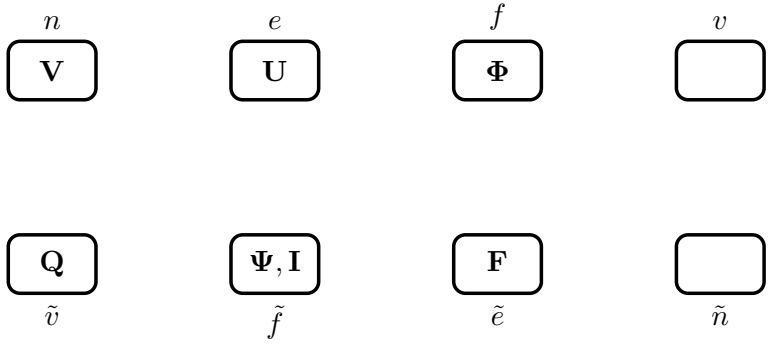

Figure 2.4: Electromagnetic quantities can be associated to the different geometrical entities of the mesh. Full symmetry of the diagram is obtained by adding the magnetic charge $\mathbf{Q}_m$ on the primal volumes, magnetic current $\mathbf{I}_m$ on primal faces, magnetic scalar potential $\mathbf{V}_m$ on the dual nodes and electric vector potential $\mathbf{A}_e$ on the dual edges. However, these quantities were left out because are either – as far as it is known – nonphysical ($\mathbf{Q}_m$, $\mathbf{I}_m$) or not interesting for the problem addressed in this thesis ($\mathbf{V}_m$, $\mathbf{A}_e$).

Quantities that are source variables are associated to the dual grid, while quantities that are configuration variables are associated to the primal grid. This kind of choice is the one originally made by Tonti, however there is no reason that prevents us doing the opposite choice. Exchanging the role of the two grids lead us to the *complementary formulations* discussed in Chapter 5.

2.4 Discrete differential operators

As mentioned in the introduction of this chapter, one kind of equation we find in physical theories are the *balance equations*. A differential operator usually arises in the continuous form of balance equations and thus, in numerical schemes like DGA, we need its discrete counterpart. Discrete counterparts of the differential operators gradient (∇), curl ($\nabla\times$) and divergence ($\nabla\cdot$) are obtained from the fundamental theorem of calculus, the Stokes theorem and the Gauss theorem respectively [Bon15, Ton06]. As we shall see, discrete differential operators are available both on the primal mesh and on the dual mesh and are strictly correlated. Moreover, they encode the topology of the problem: by stretching or twisting the mesh, they do not change. Finally, balance equations obtained that way are exact: discrete differential operators introduce no approximation.

2.4.1 The gradient

Given a line, not necessarily straight, extending from point a to point b and with unit tangent vector $\boldsymbol{t}$, the fundamental theorem of calculus states that

$$\int_L \nabla f \ \cdot \boldsymbol{t} dl = f(b) - f(a).$$

This can be directly transposed to the discrete domain as

$$\begin{aligned} &\mathsf{GRAD} : \mathbf{X}_{\mathcal{N}} \to \mathbf{X}_{\mathcal{E}} \\ &\mathsf{GRAD}(u)_e = \sum_{n \in \mathcal{G}(\mathcal{N})} \mathbf{G}(e,n) \boldsymbol{u}_n \end{aligned}$$

where $\boldsymbol{u}$ is the array of degrees of freedom attached to the nodes and $\mathbf{G}(e,n)$ is the $card(\mathcal{G}(\mathcal{E})) \times card(\mathcal{G}(\mathcal{N}))$ matrix of incidence numbers between nodes and edges, whose entries are

$$\mathbf{G}(e,n) = \begin{cases} -1 & \text{if } e \text{ exits from } n \\ +1 & \text{if } e \text{ enters } n \\ 0 & \text{otherwise} \end{cases}$$

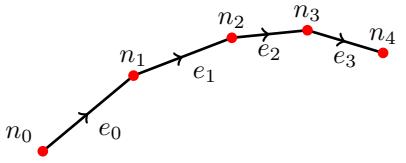

$$\mathbf{G} = \begin{pmatrix} -1 & +1 & & & \\ & -1 & +1 & & \\ & & -1 & +1 & \\ & & & -1 & +1 \end{pmatrix}$$

Figure 2.5: Example of a gradient matrix.

2.4.2 The curl

The Kelvin-Stokes theorem, which relates the curl of a vector field $\boldsymbol{F}$ integrated over a surface Σ to the circulation of $\boldsymbol{F}$ across the boundary of Σ

$$\int_{\Sigma} \nabla \times \boldsymbol{F} \cdot d\boldsymbol{\Sigma} = \oint_{\partial\Sigma} \boldsymbol{F} \cdot d\boldsymbol{r}$$

and the definition of the curl

$$(\nabla \times \boldsymbol{F}) \cdot \boldsymbol{n} = \lim_{S \to 0} \frac{1}{|S|} \oint_{C} \boldsymbol{F} \cdot d\boldsymbol{r}$$

can be directly transposed to the discrete domain as the discrete curl operator

$$\begin{aligned} &\mathsf{CURL} : \mathbf{X}_{\mathcal{E}} \to \mathbf{X}_{\mathcal{S}} \\ &\mathsf{CURL}(u)_f = \sum_{e \in \mathcal{G}(\mathcal{E})} \mathbf{C}(f,e)\boldsymbol{u}_e \end{aligned}$$

where $\boldsymbol{u}$ is the array of degrees of freedom attached to the edges and $\mathbf{C}(f,e)$ is the $card(\mathcal{G}(\mathcal{S})) \times card(\mathcal{G}(\mathcal{E}))$ matrix of incidence numbers between edges and surfaces, whose entries are

$$\mathbf{C}(f,e) = \begin{cases} -1 & \text{if } e \text{ has not the same orientation of } f \\ +1 & \text{if } e \text{ has the same orientation of } f \\ 0 & \text{otherwise} \end{cases}$$

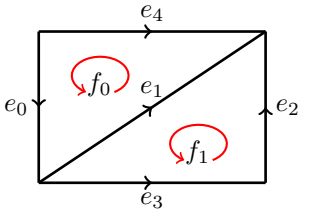

$$\mathbf{C} = \begin{pmatrix} +1 & +1 & & & -1 \\ & -1 & +1 & +1 & \end{pmatrix}$$

Figure 2.6: Example of a curl matrix.

2.4.3 The divergence

The Gauss theorem, which relates the divergence of a vector field $\boldsymbol{F}$ integrated over a volume Ω to the flux of $\boldsymbol{F}$ across the boundary of Ω

$$\int_{\Omega} \nabla \cdot \boldsymbol{F}\, d\Omega = \oint_{\partial\Omega} \boldsymbol{F} \cdot d\boldsymbol{S}$$

and the definition of the divergence

$$\nabla \cdot \boldsymbol{F} = \lim_{V \to 0} \frac{1}{|V|} \int_{S} \boldsymbol{F} \cdot d\boldsymbol{S}$$

can be directly transposed to the discrete domain as the discrete divergence operator

$$\begin{aligned} &\mathsf{DIV} : \mathbf{X}_{\mathcal{S}} \to \mathbf{X}_{\mathcal{V}} \\ &\mathsf{DIV}(u)_v = \sum_{f \in \mathcal{G}(\mathcal{S})} \mathbf{D}(v,f)\boldsymbol{u}_f \end{aligned}$$

where $\boldsymbol{u}$ is the array of degrees of freedom attached to the faces and $\mathbf{D}(v,f)$ is the $card(\mathcal{G}(\mathcal{V})) \times card(\mathcal{G}(\mathcal{S}))$ matrix of incidence number between surfaces and volumes, whose entries are

$$\mathbf{D}(f,e) = \begin{cases} -1 & \text{if } f \text{ points inward of } v \\ +1 & \text{if } f \text{ points outward of } v \end{cases}$$

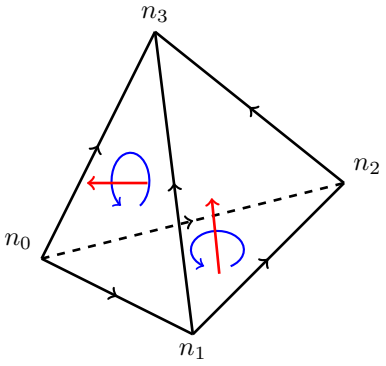

$$\mathbf{D} = \begin{pmatrix} +1 & -1 & +1 & -1 \end{pmatrix}$$

Figure 2.7: Example of a divergence matrix. Face f_i is the one which has not n_i in its vertices.

2.4.4 Dual discrete operators

The discrete differential operators on the dual grid are obtained by the same reasoning used on primal grid. Numerically are computed by transposing the primal ones.

$$\tilde{\mathbf{G}} = \mathbf{D}^T, \quad \tilde{\mathbf{C}} = \mathbf{C}^T, \quad \tilde{\mathbf{D}} = -\mathbf{G}^T.$$

The minus sign in the third relation is due to the nodes being positively oriented as sinks.

2.4.5 Degrees of freedom and discrete operators

From the discussion of the previous section it emerges that discrete operators link quantities on nodes with quantities on edges ($\mathbf{G}$, $\tilde{\mathbf{G}}$), quantities on edges with quantities on surfaces ($\mathbf{C}$, $\tilde{\mathbf{C}}$) and quantities on surfaces with quantities on volumes ($\mathbf{D}$, $\tilde{\mathbf{D}}$): in some way they link lower-dimensional geometric entities with higher-dimensional geometric entities.

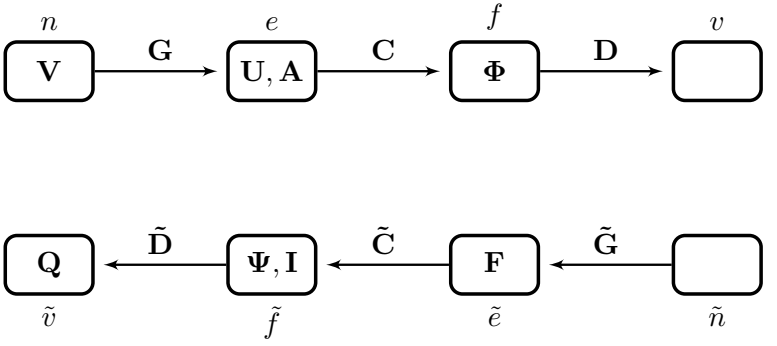

Figure 2.8: Discrete differential operators link quantities on nodes with quantities on edges, quantities on edges with quantities on surfaces and quantities on surfaces with quantities on volumes.

Moreover, by applying a discrete operator to a quantity of one of the two grids the result is a quantity belonging to *the same* grid, as depicted in the diagram of Figure 2.8.

Discrete operators satisfy the relations $\mathbf{CG} = \mathbf{0}$ and $\mathbf{DC} = \mathbf{0}$, which are the discrete counterparts of the well-known vector identities $\nabla \times (\nabla f) = \mathbf{0}$ and $\nabla \cdot (\nabla \times \mathbf{F}) = 0$. Of course the same is true for dual operators, since $\tilde{\mathbf{C}}\tilde{\mathbf{G}} = \mathbf{C}^T\mathbf{D}^T = (\mathbf{DC})^T = \mathbf{0}$ and $\tilde{\mathbf{D}}\tilde{\mathbf{C}} = \mathbf{G}^T\mathbf{C}^T = (\mathbf{CG})^T = \mathbf{0}$.

2.5 Constitutive matrices

Constitutive matrices are responsible to establish the last link missing, which is the one between the quantities defined on entities of the primal grid and the quantities defined on the corresponding entities on dual grid. An example from electromagnetics, as we will see in the next chapter, is the link between electromotive force on the primal edges and the electric flux on the dual faces.

Constitutive matrices (also named *discrete Hodge operators*) in DGA are constructed according the *energetic approach* [CT05] and will allow us to write the *discrete constitutive equations*.

2.5.1 Piecewise uniform basis functions

Start by considering the arrays of degrees of freedom

$$X_i = \int_{r_i} \boldsymbol{x} \cdot d\boldsymbol{r} \tag{2.1}$$

$$Y_i = \int_{\bar{r}_i} \boldsymbol{y} \cdot d\boldsymbol{r} \tag{2.2}$$

where r_i is a primal edge or a primal face and $\bar{r}_i$ is its counterpart (i.e. $\bar{e}_i = \tilde{f}_i$). Fields are recovered from the DoFs by interpolating with the *piecewise uniform vector functions* $\{\boldsymbol{v}_i^r\}$ attached to the geometric entity r_i

$$\boldsymbol{x} = \sum_{i \in \mathcal{R}} \boldsymbol{v}_i^r X_i, \tag{2.3}$$

where $\mathcal{R} \in \{1, \dots, 6\}$ if $r_i = e_i$ and $\mathcal{R} \in \{1, \dots, 4\}$ if $r_i = f_i$. We want these functions comply with some specifications, in particular

- They form a basis: $\int_{r_j} \boldsymbol{v}_i^r \cdot d\boldsymbol{r} = \delta_{ij}$, where δ_{ij} is the Kroneker symbol;
- They represent an uniform field *exactly*, i.e. with no approximation.

The energetic approach is based on the observation that energy quantities are formed by expressions like

$$W = \frac{1}{2} \int_{v_k} \boldsymbol{x}' \cdot \boldsymbol{y} \, dv, \tag{2.4}$$

where $v_k \in \mathcal{G}(\mathcal{V})$. Assume, for now, that the fields $\boldsymbol{x}'$ and $\boldsymbol{y}$ are unrelated. By using the basis functions, we can rewrite the expression as

$$W = \frac{1}{2} \int_{v_k} \sum_{i \in \mathcal{R}} \boldsymbol{v}_i^r X_i' \cdot \boldsymbol{y} \, dv = \frac{1}{2} \sum_{i \in \mathcal{R}} X_i' \int_{v_k} \boldsymbol{v}_i^r \cdot \boldsymbol{y} \, dv \tag{2.5}$$

In the last equation the quantity $\int_{v_k} \boldsymbol{v}_i^r \cdot \boldsymbol{y} \, dv$ appears. We require to the relation

$$Y_i = \int_{v_k} \boldsymbol{v}_i^r \cdot \boldsymbol{y} \, dv \tag{2.6}$$

to hold exactly at least for uniform fields. We can then rewrite the energy functional using the degrees of freedom

$$W = \frac{1}{2} \sum_i X_i' Y_i \tag{2.7}$$

Moreover, if $\boldsymbol{y}$ is an uniform field it can be taken out of the integral, obtaining

$$Y_i = \boldsymbol{y} \cdot \int_{v_k} \boldsymbol{v}_i^r \; dv. \tag{2.8}$$

From this last equation another requirement is derived for the basis functions. Since a degree of freedom is a quantity obtained by integrating a field over its corresponding geometric entity (2.2), we require that

$$\int_{v_k} \boldsymbol{v}_i^r \; dv = \int_{\bar{r}_i} d\boldsymbol{r} = \bar{\boldsymbol{r}}_i, \tag{2.9}$$

where $\bar{\boldsymbol{r}}_i$ is the vector associated to the geometric entity $\bar{r}_i$. The requirement expressed in (2.9) is called *consistency condition* [Bos01].

2.5.2 Computing the matrices

Until now fields $\boldsymbol{x}'$ and $\boldsymbol{y}$ have been treated as unrelated. This assumption is now dropped, and from now on the fields will be considered related by the constitutive equation $\boldsymbol{y} \approx \boldsymbol{m}\boldsymbol{x}$, where $\boldsymbol{m}$ is a tensor. Thus, it is possible to write

$$\boldsymbol{y} \approx \boldsymbol{m}\boldsymbol{x} = \boldsymbol{m} \sum_{j \in \mathcal{R}} \boldsymbol{v}_j^r X_j. \tag{2.10}$$

By substituting the last equation in (2.5) we obtain

$$W = \frac{1}{2} \sum_{i \in \mathcal{R}} X_i' \int_{v_k} \boldsymbol{v}_i^r \cdot \boldsymbol{m} \sum_{j \in \mathcal{R}} \boldsymbol{v}_j^r X_j \; dv \tag{2.11}$$

and, comparing (2.11) with (2.7) we obtain

$$Y_i = \sum_{j \in \mathcal{R}} \int_{v_k} \boldsymbol{v}_i^r \cdot \boldsymbol{m}\boldsymbol{v}_j^r dv \; X_j. \tag{2.12}$$

Finally, matrix entries are calculated as

$$M_{ij} = \int_{v_k} \boldsymbol{v}_i^r \cdot \boldsymbol{m}\boldsymbol{v}_j^r dv, \tag{2.13}$$

allowing to write the discrete constitutive relation between arrays of DoFs

$$\mathbf{Y} = \mathbf{M}\mathbf{X}. \tag{2.14}$$

2.5.3 Consistency

The constitutive matrices built according to the energetic approach have the property of being *consistent*, which means that they map exactly circulations onto fluxes and vice-versa [CST10a]. Consistency results in the commutativity of the following diagram:

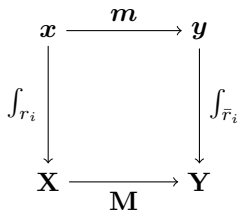

The meaning of the diagram is that degrees of freedom in $\mathbf{Y}$ can be computed either by first multiplying $\boldsymbol{x}$ by $\boldsymbol{m}$ and then integrating or by first integrating and then multiplying $\mathbf{X}$ by $\mathbf{M}$: the result will be exactly the same. Consistency, however, holds only for uniform fields and thus constitutive matrices are the source of approximation in the DGA method.

2.6 The big picture

In the previous sections a number of concepts were introduced, in particular

- the spatial discretization, obtained by means of two grids in duality,
- the degrees of freedom, which relate physical quantities to geometric elements,
- the discrete differential operators, which encode the topology of a problem,
- the constitutive matrices, which encode the metric and the material properties of a problem.

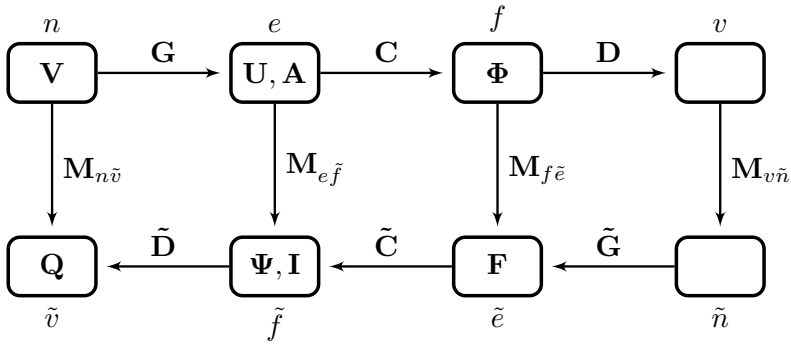

Figure 2.9: Constitutive matrices, also called discrete Hodge operators, link primal complex and dual complex. The depicted diagram is called Tonti's diagram.

We also started building a diagram (Figures 2.4 and 2.8), which we can now complete (Figure 2.9) by adding the constitutive matrices (also called *discrete Hodge operators*). We obtain the so-called *Tonti's diagram*, which summarizes all the geometrical and topological relations between the quantities involved in the Maxwell equations and in the constitutive relations.

II

Frequency Domain Discrete Geometric Approach

3

The electromagnetic wave propagation problem

Electromagnetic field, in the classical setting, is described by the Maxwell's equations. They are named after their author James Clerk Maxwell, who collected all the laws of electricity and magnetism known in the XIX century and extended them [Max91]. This chapter is devoted to a quick description of the Maxwell's equations. In the first part, the continuous equations are presented, both in the integral and in the differential form. Time-harmonic version is then described, and wave equation is obtained. Boundary conditions for the electromagnetic wave equation are then discussed. In the second part the discrete equations in the DGA formalism are discussed, the discrete wave equation is derived and the boundary conditions are shown. In a final section a brief overview of the difficulties that arise in the numerical solution is given.

3.1 Maxwell's equations

Faraday law. This law is due to Michael Faraday who discovered electromagnetic induction in 1831. Informally, it states that if an electric circuit links a time-varying magnetic field, in that circuit an electromotive force of magnitude equal to the opposite of the variation of magnetic field is observed. The relation it establishes between the electric field $\boldsymbol{E}$ on the boundary $\partial\Sigma$ of the surface Σ and the magnetic field $\boldsymbol{B}$ across Σ is

$$\oint_{\partial\Sigma} \boldsymbol{E} \cdot d\boldsymbol{l} = -\frac{d}{dt} \int_{\Sigma} \boldsymbol{B} \cdot d\boldsymbol{S}.$$

Ampère law. Due to André-Marie Ampère who formulated it in 1826, the law states that the circulation of the magnetic field along a closed line is equal to the sum of the currents linked by the line, or

$$\oint_{\partial\Sigma} \boldsymbol{H} \cdot d\boldsymbol{l} = \int_{\Sigma} \boldsymbol{J} \cdot d\boldsymbol{S}.$$

Gauss electric law This law is due to Carl Friedrich Gauss who formulated it in 1835. It states that the net electric flux across any closed surface $\partial\Omega$ is equal to the net electric charge enclosed in the volume Ω bounded by that surface, or

$$\oint_{\partial\Omega} \boldsymbol{D} \cdot d\boldsymbol{S} = \int_{\Omega} \rho dV.$$

Gauss magnetic law This law establishes the absence of magnetic monopoles by the fact that the flux of magnetic field $\boldsymbol{B}$ is identically zero across any closed surface, or

$$\oint_{\partial\Omega} \boldsymbol{B} \cdot d\boldsymbol{S} = 0.$$

However, these four laws are insufficient to derive the wave-like nature of the electromagnetic field. What is missing from these laws is the *displacement current*, an idea conceived by Maxwell in 1861. Displacement current is the rate of change of electric displacement field $\boldsymbol{D}$ but, despite having the dimensions of a current density, is not due to moving charges but to a time-varying electric field. Displacement current has an associated magnetic field and is accounted for by an additional term in the Ampère law, which becomes the Ampère–Maxwell law

$$\oint_{\partial\Sigma} \boldsymbol{H} \cdot d\boldsymbol{l} = \int_{\Sigma} \boldsymbol{J} \cdot d\boldsymbol{S} + \frac{d}{dt} \int_{\Sigma} \boldsymbol{D} \cdot d\boldsymbol{S}.$$

3.1.1 Time-harmonic equations and wave propagation

For the purposes of this work, we are interested to study wave propagation at single frequency, so the time-harmonic version of the Maxwell equations is now introduced. Time-harmonic Maxwell equations, like the time-dependent ones, involve five vector fields, namely:

- the electric field $\boldsymbol{e}$,
- the electric displacement field $\boldsymbol{d}$,
- the magnetic induction field $\boldsymbol{b}$,
- the magnetic field $\boldsymbol{h}$,
- the current density field $\boldsymbol{j}$,

where the dependence on position vector $\boldsymbol{r}$ is considered implicit. In the time-harmonic setting, at the angular frequency ω and with an implicit time dependence of $e^{i\omega t}$, Maxwell's equations are commonly written as

$$\nabla \cdot \boldsymbol{d} = \rho, \qquad \text{(Gauss' electric law)} \tag{3.1}$$

$$\nabla \cdot \boldsymbol{b} = 0, \qquad \text{(Gauss' magnetic law)} \tag{3.2}$$

$$\nabla \times \boldsymbol{e} = -i\omega \boldsymbol{b}, \qquad \text{(Faraday–Neumann law)} \tag{3.3}$$

$$\nabla \times \boldsymbol{h} = i\omega \boldsymbol{d} + \boldsymbol{j}. \qquad \text{(Ampère–Maxwell law)} \tag{3.4}$$

Divergence theorem and Kelvin–Stokes theorem were used to switch from integral form to the differential form. The complex-valued vector fields involved in the equations are related by three constitutive equations, namely:

$$\boldsymbol{d} = \boldsymbol{\varepsilon}\boldsymbol{e}, \qquad \text{(Electric constitutive equation)} \tag{3.5}$$

$$\boldsymbol{h} = \boldsymbol{\nu}\boldsymbol{b}, \qquad \text{(Magnetic constitutive equation)} \tag{3.6}$$

$$\boldsymbol{j} = \boldsymbol{\sigma}\boldsymbol{e}, \qquad \text{(Ohm's law)} \tag{3.7}$$

where $\boldsymbol{\varepsilon}$, $\boldsymbol{\nu}$ and $\boldsymbol{\sigma}$ are the complex-valued, symmetric and positive definite material tensors. These equations account for the properties of the materials where the electromagnetic phenomena take place.

Assuming a domain without conductors ($\boldsymbol{\sigma} = 0$), equation (3.3) can be solved for $\boldsymbol{b}$. Substituting $\boldsymbol{b}$ in (3.6) and substituting this last result together with (3.5) in (3.4), the equation

$$\nabla \times \boldsymbol{\nu}\nabla \times \boldsymbol{e} - \omega^2 \boldsymbol{\varepsilon}\boldsymbol{e} = -i\omega \boldsymbol{j}, \tag{3.8}$$

can be obtained. Assuming that the materials are linear, isotropic and homogeneous, the material properties become the scalars $\mu = \mu_r \mu_0$ and $\varepsilon = \varepsilon_r \varepsilon_0$. The wavenumber $\kappa^2 = -\omega^2 \mu\varepsilon$ is then defined. Assuming that there are no sources, by using the vector identity $\nabla(\nabla \cdot \boldsymbol{A}) - \nabla \times \nabla \times \boldsymbol{A} = \nabla^2 \boldsymbol{A}$ we can obtain the vector Helmholtz equation

$$\nabla^2 \boldsymbol{e} - \kappa^2 \boldsymbol{e} = \boldsymbol{0}, \tag{3.9}$$

which is the mathematical description of wave propagation in frequency domain. The equation that will be solved numerically, however, will be the (3.8) because it is more general than (3.9).

3.1.2 Boundary conditions

The problem described by (3.8) and defined in the domain Ω with outward normal $\boldsymbol{n}$ is usually solved subject to specific boundary conditions applied on $\partial\Omega$. The two most common are the Dirichlet boundary condition ($\boldsymbol{n} \times \boldsymbol{e} = \boldsymbol{0}$) and the Neumann boundary condition ($\boldsymbol{n} \times \boldsymbol{h} = \boldsymbol{0}$). The former condition is also known as *Perfect Electric Conductor* (PEC) condition and imposes that the tangential component of the electric field must vanish at the boundary, while the latter is also known as *Perfect Magnetic Conductor* (PMC) condition and imposes that the tangential component of the electric field must vanish at the boundary. To draw an analogy with the circuital world, PEC is analogous to a perfect short circuit while PMC is analogous to a perfect open.

Radiation condition

Often it is necessary to deal with problems defined in unbounded regions, for this reason a condition on the fields at infinity needs to be enforced. This is done by means of what is known as *radiation condition*. Numerically this kind of condition will be translated to the *admittance boundary condition* and will be discussed in Section 3.2.4.

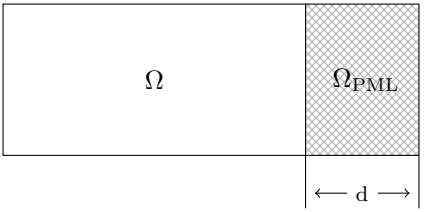

Figure 3.1: A domain Ω terminated with a PML Ω_{PML} on the right. An arrangement like this can be useful in the simulation of waveguides.

Perfectly Matched Layers

PMLs are not a kind of boundary condition, however they are a very effective way to terminate the computational domain in numerical simulations where waves are involved. They offer better performance than a simple radiation condition, because can handle radiation incident at any angle. A great number of variants have been proposed in literature, not only for electromagnetics but also for acoustics and elastodynamics [Taf98, Ber94, MYW14, Bas03]. In general, PMLs can be seen as artificial absorbing materials, characterized by an anisotropic behaviour. This behaviour is encoded in the constitutive relations in form of specific tensors

$$\bar{\bar{s}} = \begin{bmatrix} \frac{s_y s_z}{s_x} & 0 & 0 \\ 0 & \frac{s_x s_z}{s_y} & 0 \\ 0 & 0 & \frac{s_x s_y}{s_z} \end{bmatrix},$$

where the terms $s_\xi, \xi \in \{x, y, z\}$ have the form

$$s_\xi = \kappa_\xi + \frac{\sigma_\xi}{i\omega\epsilon_0}. \tag{3.10}$$

Usually the term κ_ξ is taken equal to 1, while the term σ_ξ is a function of the coordinate ξ, which allows for a spatial scaling of the PML parameters along the direction of ξ. It has been shown from practice that the most effective type of scaling is the *polynomial scaling* [Ber94], which takes the form

$$\sigma_\xi(\xi) = \left(\frac{\xi}{d}\right)^m \sigma_{\xi,\max}. \tag{3.11}$$

As detailed in [Taf98], suitable values for m have been found to be in the range between 3 and 4, while the optimal value of $\sigma_{\xi,\max}$ has been found to be

$$\sigma_{\xi,\text{opt}} = \frac{m+1}{150\pi\sqrt{\epsilon_r}\Delta\xi}, \tag{3.12}$$

where $\Delta\xi$ is the discretization step in the direction of ξ. The tensor is introduced in the

constitutive relations as

$$\boldsymbol{d} = \epsilon\, \bar{\bar{s}}\, \boldsymbol{e}, \tag{3.13}$$

$$\boldsymbol{b} = \mu\, \bar{\bar{s}}\, \boldsymbol{h}, \tag{3.14}$$

so the Maxwell's equations in the PML region become

$$\nabla \times \boldsymbol{e} = -j\omega\mu\, \bar{\bar{s}}\, \boldsymbol{h}, \tag{3.15}$$

$$\nabla \times \boldsymbol{h} = j\omega\epsilon\, \bar{\bar{s}}\, \boldsymbol{e}. \tag{3.16}$$

From now on we will refer to the PML material parameters as $\bar{\bar{\epsilon}} = \epsilon\, \bar{\bar{s}}$ and $\bar{\bar{\mu}} = \mu\, \bar{\bar{s}}$.

3.2 Maxwell's equations in the discrete domain

Our task is now to translate the continuous electromagnetic wave propagation problem to the discrete setting, using the Discrete Geometric Approach detailed in Chapter 2. Our discussion will start from the discrete Maxwell equations together with the discrete constitutive relations. Wave propagation equation is then derived and boundary conditions are discussed.

3.2.1 Discrete Maxwell equations

In the present section the four discrete Maxwell equations are discussed. From now on, degrees of freedom pertaining to the dual complex will be marked with a tilde (like $\tilde{\mathbf{Y}}$): this notation helps in avoiding ambiguities, especially when complementary formulation is discussed in Chapter 5.

Faraday–Neumann law. Since in the discrete domain we deal with integral quantities, the discrete Faraday–Neumann law involves the electromotive forces $\mathbf{U}$, which are the line integrals of $\boldsymbol{e}$ on the primal edges and the magnetic fluxes $\mathbf{\Phi}$, which are the surface integrals of $\boldsymbol{b}$ on the primal faces. By direct analogy with (3.3), we can write

$$\mathbf{C}\mathbf{U} = -i\omega\mathbf{\Phi}. \tag{3.17}$$

Ampère–Maxwell law. This law involves the magnetomotive forces $\tilde{\mathbf{F}}$, which are the line integrals of $\boldsymbol{h}$ on the dual edges, the electric fluxes $\tilde{\mathbf{\Psi}}$ which are the surface integrals of $\boldsymbol{d}$ on the dual faces and the electric currents $\tilde{\mathbf{I}}$, integrals of $\boldsymbol{j}$ on dual faces. By direct analogy with (3.4), we can write

$$\tilde{\mathbf{C}}\tilde{\mathbf{F}} = i\omega\tilde{\mathbf{\Psi}} + \tilde{\mathbf{I}}. \tag{3.18}$$

Gauss electric law. This law involves $\tilde{\mathbf{\Psi}}$ and the charge $\tilde{\mathbf{Q}}$ contained in a given dual volume. By direct analogy with (3.1), we can write

$$\tilde{\mathbf{D}}\tilde{\mathbf{\Psi}} = \tilde{\mathbf{Q}}. \tag{3.19}$$

Gauss magnetic law. This law involves $\mathbf{\Phi}$. By direct analogy with (3.1), we can write

$$\mathbf{D\Phi} = \mathbf{0}. \tag{3.20}$$

We note that these equations involve quantities associated to both grids. The quantities on the dual grid are $\tilde{\mathbf{\Psi}}$, $\tilde{\mathbf{I}}$ and $\tilde{\mathbf{Q}}$, and are associated to the *source variables* of the electromagnetic field. Quantities $\mathbf{U}$ and $\mathbf{\Phi}$, on the other hand, are associated to the *configuration variables* of the electromagnetic field. According to [Ton14], source variables account for *causes* of physical phenomena, while configuration variables account for *effects*. The product of source and configuration variables give rise to *energetic* variables.

3.2.2 Discrete constitutive relations

The discrete constitutive relations relate quantities associated to the primal grid to quantities associated to the dual grid. They are:

$$\tilde{\mathbf{\Psi}} = \mathbf{M}_\varepsilon \mathbf{U}, \tag{3.21}$$

$$\tilde{\mathbf{F}} = \mathbf{M}_\nu \mathbf{\Phi}, \tag{3.22}$$

$$\tilde{\mathbf{I}} = \mathbf{M}_\sigma \mathbf{U}. \tag{3.23}$$

Consistency implies that for uniform fields the constitutive relations are exact, and the following diagrams commute:

$$\begin{array}{ccc} \boldsymbol{e} & \xrightarrow{\boldsymbol{\varepsilon}} & \boldsymbol{d} \\ \downarrow{\scriptstyle \int_{e_i}} & & \downarrow{\scriptstyle \int_{\tilde{f}_i}} \\ \mathbf{U} & \xrightarrow[\mathbf{M}_\varepsilon]{} & \tilde{\mathbf{\Psi}} \end{array} \qquad \begin{array}{ccc} \boldsymbol{b} & \xrightarrow{\boldsymbol{\nu}} & \boldsymbol{h} \\ \downarrow{\scriptstyle \int_{f_i}} & & \downarrow{\scriptstyle \int_{\tilde{e}_i}} \\ \mathbf{\Phi} & \xrightarrow[\mathbf{M}_\nu]{} & \tilde{\mathbf{F}} \end{array} \qquad \begin{array}{ccc} \boldsymbol{e} & \xrightarrow{\boldsymbol{\sigma}} & \boldsymbol{j} \\ \downarrow{\scriptstyle \int_{e_i}} & & \downarrow{\scriptstyle \int_{\tilde{f}_i}} \\ \mathbf{U} & \xrightarrow[\mathbf{M}_\sigma]{} & \tilde{\mathbf{I}} \end{array}$$

3.2.3 Discrete wave propagation problem

Using the same steps as the ones used to derive (3.8), we can derive from discrete Maxwell equations the discrete wave propagation equation

$$(\tilde{\mathbf{C}}\mathbf{M}_\nu\mathbf{C} - \omega^2\mu_0\varepsilon_0\mathbf{M}_\varepsilon)\mathbf{U} = -i\omega\mu_0\tilde{\mathbf{I}}, \tag{3.24}$$

where $\mathbf{U}$ is the array of the unknown electromotive forces associated to the primal edge of the mesh, while $\tilde{\tilde{\mathbf{I}}}$ is the array of the currents on the dual faces of the mesh.

3.2.4 Boundary conditions

To solve (3.24) we must be able to impose the appropriate boundary conditions. As in the continuous case there is the PEC (Perfect Electric Conductor) boundary condition,

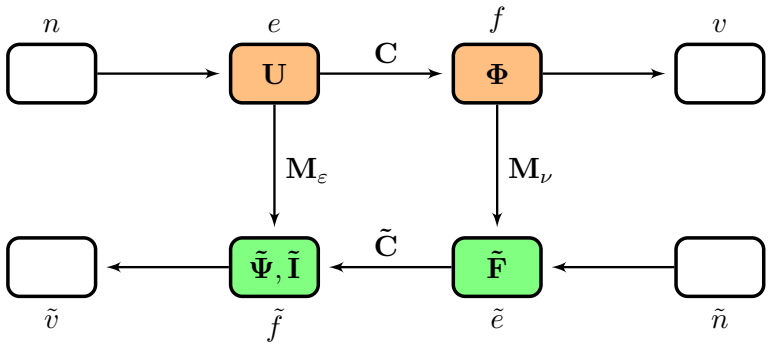

Figure 3.2: Tonti's diagram of the E-field formulation of the wave propagation problem. Electromotive forces and magnetic fluxes are on the primal grid and are linked by the Faraday–Neumann law, while magnetomotive forces and electric fluxes are on the dual grid and are linked by the Ampére–Maxwell law. Constitutive matrices link the two grids.

the PMC (Perfect Magnetic Conductor) boundary condition and the radiation condition.

Perfect Electric Conductor. Since the array of DoFs $\mathbf{U}$ includes the DoFs associated to boundary edges of the grid, it is sufficient to force to zero these unknowns. This could be done by removing from the matrix the rows and the columns corresponding to the boundary edges and by doing the same with the corresponding entries in the unknown array $\mathbf{U}$ and in the right hand side (see for example [TV03]).

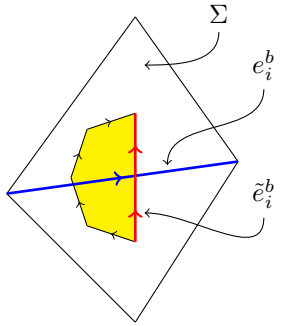

Figure 3.3: Geometric entities on a boundary. The primal edge e_i^b (blue) has a dual boundary edge $\tilde{e}_i^b$ in 1-to-1 correspondence (red) and a dual face $\tilde{f}_i$, also in 1-to-1 correspondence (yellow).

Perfect Magnetic Conductor. To apply this condition it is required to set to zero the magnetomotive forces on the boundary dual edges where it is applied. To see why, the balance of the Ampère–Maxwell equation is rewritten considering also the magnetomotive forces $\tilde{\mathbf{F}}^b$ on dual boundary edges (marked in red in Fig. 3.3):

$$\tilde{\mathbf{C}}\tilde{\mathbf{F}} - \tilde{\mathbf{F}}^b = i\omega\tilde{\mathbf{\Psi}} + \tilde{\mathbf{I}}. \tag{3.25}$$

However, in the PMC case $\tilde{\mathbf{F}}^b$ is zero because we want the tangent component of the magnetic field to be zero, so nothing changes in (3.24). This means that if (3.24) is solved as is, the PMC boundary condition is implicit. The minus sign before the $\tilde{\mathbf{F}}^b$ term is due to the fact that (Fig. 3.3) the dual face (yellow) is oriented by the outer orientation of the primal edge (blue). However, the cross product between the primal boundary edge vector and the dual boundary edge vectors (red) must be oriented as the outward normal and thus the dual edge has the opposite orientation of the dual face, and this is reflected in the minus sign.

Admittance boundary condition. This kind of condition, usually known as *impedance boundary condition*, was first proposed in the realm of DGA in [CST12]. The idea on which it is based is that, by definition of impedance/admittance, electric field and magnetic field must be constrained to a certain ratio on the boundaries where it is applied. What admittance boundary condition actually does is constraining the tangential components of the fields, as prescribed by the relation

$$\boldsymbol{h} \times \boldsymbol{n} = Y((\boldsymbol{n} \times \boldsymbol{e}) \times \boldsymbol{n}), \tag{3.26}$$

where Y is the wave admittance parameter. This is achieved by means of a specific admittance matrix $\mathbf{M}_Y$ built according to the already mentioned energetic approach, but applied on boundary elements. If $\tilde{\mathbf{F}}^b$ is the array of magnetomotive forces on the dual boundary edges and $\mathbf{U}^b$ the one associated to the electromotive forces on the primal boundary edges, the admittance boundary condition is written as

$$\tilde{\mathbf{F}}^b = \mathbf{M}_Y \mathbf{U}^b, \tag{3.27}$$

which is the discrete equivalent of (3.26). The condition is introduced by using (3.25) to derive the wave propagation equation

$$(\tilde{\mathbf{C}}\mathbf{M}_\nu\mathbf{C} - \omega^2\mu_0\varepsilon_0\mathbf{M}_\varepsilon)\mathbf{U} + i\omega\mu_0\tilde{\mathbf{F}}^b = -i\omega\mu_0\tilde{\mathbf{I}}, \tag{3.28}$$

and then by substituting (3.27). This procedure leads to the new equation [CST12]:

$$(\tilde{\mathbf{C}}\mathbf{M}_\nu\mathbf{C} - \omega^2\mu_0\varepsilon_0\mathbf{M}_\varepsilon + i\omega\mu_0\mathbf{M}_Y)\mathbf{U} = -i\omega\mu_0\tilde{\mathbf{I}}, \tag{3.29}$$

where $\mathbf{M}_Y$ now operates on the whole array $\mathbf{U}$ and has nonzero entries only in correspondence of the boundary edges where the admittance condition is applied. Looking at (3.27) and at (3.29), we see that the "controlled quantity" is the magnetomotive force on dual edges, while the unknown quantity is the electromotive forces on primal edges: this is why admittance is used instead of the more common impedance.

3.3 Solution of the wave propagation problem

Solving numerically the problem (3.29) is quite challenging and, despite there is an extensive literature on the topic, the problem appears to be far from being closed. The system matrix is complex symmetric but is not positive definite and, in particular, the problems arise from the term $\tilde{\mathbf{C}}\mathbf{M}_\nu\mathbf{C}$ which is not full-rank. All the common Krylov

iterative schemes (like BiCGStab, GMRES, SYMMLQ, ...) fail to converge and, for this reason, in the last two decades various techniques have been proposed.

One of the techniques goes under the name of *regularization* and was introduced by several authors in a number of variants [CW02, SF13]. The idea is to substitute the curl-curl operator with the laplacian operator which, from the point of view of the iterative methods, is quite well-behaved and in fact fairly good convergence is observed. However, this kind of approach has also its drawbacks: applying it to DGA requires a substantial modification of the matrix assembly process, because in this case doing local assembly is not trivial. Moreover, sparsity is heavily deteriorated because the number of nonzeros is about ten times of the non-regularized case. Finally, convergence is lost again if PMLs are employed, precluding the possibility to solve a wide class of problems.

Another class of apparently successful methods are the multigrid solvers [LT06, BO08, MNN09, Not10, CGG$^+$13]. Multigrid solvers iterate between a number of different "grids" to find a solution. The grids of the various levels are obtained from the original one by two approaches: the *geometric approach* and the *algebraic approach*. The geometric approach, as the name implies, requires the knowledge of the discretization of the problem domain. Algebraic approach, on the other hand, derives all the information it needs from the problem matrix. Different multigrid solvers are required if the problem has nodal unknowns (electrostatics) or edge unknowns (eddy currents, wave propagation), however it seems that "blackbox" and simple to use algebraic multigrid codes work only for nodal unknowns.

Despite that in the developed code it is possible to choose from a number of solvers, in practice only direct solvers are employed for wave propagation problems. In particular, Intel PARDISO and MUMPS are two good choices. Unfortunately, direct solvers limit greatly the size of the solvable problems because of their $O(n^2)$ memory usage. For example, on a machine with 32GB of RAM problems with a maximum of about 1.3M unknowns can be handled in in-core mode. Out-of-core mode allows handling bigger problems, but at the expense of greatly increased computation times. Finally, MUMPS can mitigate the issues because it can run on parallel distributed memory machines, but it is not really a solution because of the limited availability of this kind of machines to the general public.

These issues led us to the development of the equivalent model method presented in this thesis: keeping the number of unknowns as low as possible and keeping the matrix as sparse as possible seemed a good strategy to deal with problems defined in electrically large domains, like the anechoic chambers.

A promising approach is domain decomposition. Direct solvers are kept, but the computational domain is sliced in n subproblems of tractable dimension. Each subproblem is solved separately and then data is exchanged between subdomains until convergence is reached. Matrix inversion is required only at the first step, at the subsequent steps only backsubstitutions are made. The drawback is that n factorizations must be kept in memory, however they require far less space than the space required by the factorization of the full matrix. A preliminary implementation of domain decomposition as described in [TVT$^+$15] was integrated in the EMT code and is a current subject of investigation (Fig. 3.4), together with Model Order Reduction [PGHS15].

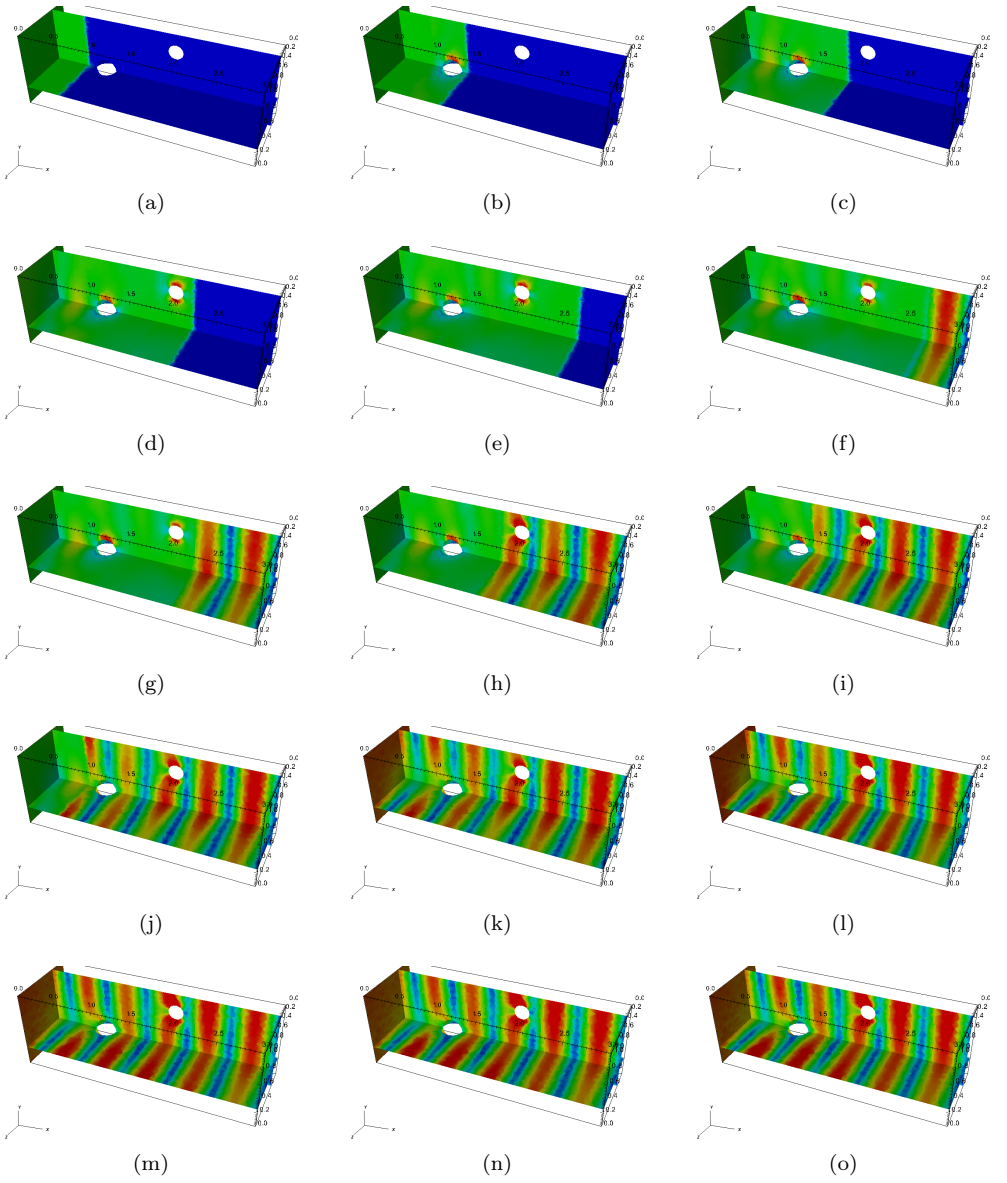

Figure 3.4: Domain decomposition applied on a test problem (6 slices). A plane wave is applied at the leftmost surface of a structure containing two perfectly conducting objects. PEC boundary condition above, below and on the rightmost surface and PMC on the sides. Figures (a) until (k) show the first 11 steps of the iteration, then steps 15, 20, 25, and 30 are depicted.

4

Sources of the electromagnetic field

Sources in electromagnetic problems can be imposed in a multitude of ways. This chapter is devoted to the discussion of some kind of sources and how they are formalized in the DGA. Three original contributions will be presented. The first is the *plane wave excitation* [CCC+15b], which allows to apply a plane wave source to the boundary of a domain. The second is a way to model arbitrary radiators by means of equivalent objects [CCC+15a]. The third is a technique to apply excitation to waveguides compatible with the presence of multiple modes at the port [CCST16b].

4.1 Plane wave source

This kind of boundary condition is useful to simulate a plane wave entering the domain Ω through a specific portion Σ of the boundary $\partial\Omega$ and it is an extension of the admittance boundary condition of [CST12]. Moreover, this kind of condition is a fundamental tool to introduce in the DGA domain decomposition techniques like the one described in [TVT+15].

Two values are associated to this source, namely the vector $\boldsymbol{h}^-$ representing the source magnetic field, and the scalar Y representing the wave impedance. Actually, if $\boldsymbol{h}^-$ is set to $\mathbf{0}$, the original admittance boundary condition is obtained.

The plane wave boundary condition is composed by a "source" part and an "admittance" part because, in addition to acting as source, it must allow energy to leave Ω: it is well known that an electromagnetic wave travelling in space that encounters some kind of object experiences reflection (or scattering), and this must be considered in this kind of boundary condition by allowing the scattered wave to exit.

Assuming Ω oriented by the outward normal $\boldsymbol{n}$, this behaviour is obtained by splitting the electric field $\boldsymbol{e}$ and the magnetic field $\boldsymbol{h}$ across Σ in two separate components

- the component *entering* Σ, due to the imposed excitation and given by the fields $\boldsymbol{e}^-, \boldsymbol{h}^-$ and directed towards $-\boldsymbol{n}$;

- the component *exiting* Σ, given by $\boldsymbol{e}^+, \boldsymbol{h}^+$ and due to the reflections, directed towards $\boldsymbol{n}$.

such that

$$\boldsymbol{e} = \boldsymbol{e}^+ + \boldsymbol{e}^-, \tag{4.1}$$

$$\boldsymbol{h} = \boldsymbol{h}^+ + \boldsymbol{h}^-. \tag{4.2}$$

The plane wave source applied on Σ is characterized by a given wave admittance Y with respect to the normal direction $\boldsymbol{n}$ (3.26), such that

$$\boldsymbol{h}^+ \times \boldsymbol{n} = Y((\boldsymbol{n} \times \boldsymbol{e}^+) \times \boldsymbol{n}), \tag{4.3}$$

$$\boldsymbol{h}^- \times \boldsymbol{n} = -Y((\boldsymbol{n} \times \boldsymbol{e}^-) \times \boldsymbol{n}), \tag{4.4}$$

hold. Equations (4.3) and (4.4) establish a relation between the tangential components of the fields, and the fact that the wave vector direction is exactly $\boldsymbol{n}$ has important consequences, as it will be explained later. In the following it will be shown how, from the considerations made, the plane wave source is incorporated in the problem (3.24).

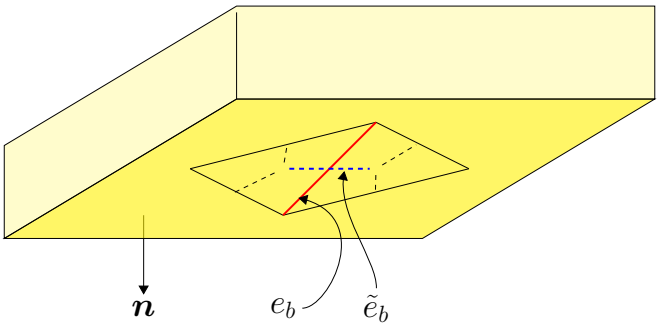

Figure 4.1: Admittance boundary condition imposes a constraint between the quantities associated to the boundary primal edges (e_b) and boundary dual edges ($\tilde{e}_b$).

The left hand side of (4.3) can be rewritten decomposing $\boldsymbol{h}^+$ in its normal component $\boldsymbol{h}_n^+$ and in its tangential component $\boldsymbol{h}_t^+$

$$\boldsymbol{h}^+ \times \boldsymbol{n} = (\boldsymbol{h}_n^+ + \boldsymbol{h}_t^+) \times \boldsymbol{n} = \boldsymbol{h}_t^+ \times \boldsymbol{n}, \tag{4.5}$$

and (4.3) becomes

$$\boldsymbol{h}_t^+ \times \boldsymbol{n} = Y \boldsymbol{e}_t^+. \tag{4.6}$$

This last formula highlights the fact that the admittance boundary condition constrains the *tangential components* of the electric and magnetic fields exiting Ω to be proportional to each other by the factor Y, the wave admittance of Σ. The direct implication is that this kind of condition is accurate only for waves exiting Ω *with normal incidence*.

According to [CST12], boundary condition for the exiting component of the field are

written as

$$\tilde{\mathbf{F}}^{b^+} = \mathbf{M}_Y \mathbf{U}^{b^+}, \tag{4.7}$$

where $\tilde{\mathbf{F}}^{b^+}$ and $\mathbf{U}^{b^+}$ are the magnetomotive and electromotive forces due to the *exiting* wave. Moreover, $\mathbf{M}_Y$ satisfies (4.7) *exactly* when the tangential components of the electric field are piecewise uniform on each element of Σ.

A similar reasoning can be carried out for the field component entering Ω. In this case (4.4) is considered, yielding

$$\boldsymbol{h}_t^- \times \boldsymbol{n} = -Y \boldsymbol{e}_t^-, \tag{4.8}$$

where the minus sign is due to the normal oriented in direction opposite to the direction in which the wave propagates. Again, (4.8) can be directly translated in discrete form

$$\tilde{\mathbf{F}}^{b^-} = -\mathbf{M}_Y \mathbf{U}^{b^-}, \tag{4.9}$$

where $\tilde{\mathbf{F}}^{b^-}$ and $\mathbf{U}^-$ are the magnetomotive and electromotive forces due to the *entering* wave. This second equation, as will be shown below, involves known quantities and is used to impose the excitation on Σ. Again, it relates exactly the tangential components of the electric and magnetic fields, so it permits to apply a plane wave with normal incidence to Σ.

4.1.1 Obtaining the linear system

Since the fields are decomposed in entering and exiting components, it holds that

$$\tilde{\mathbf{F}}^{b} = \tilde{\mathbf{F}}^{b^+} + \tilde{\mathbf{F}}^{b^-}, \tag{4.10}$$

$$\mathbf{U} = \mathbf{U}^+ + \mathbf{U}^-. \tag{4.11}$$

The array $\mathbf{U}$ is formed by two contributes, $\mathbf{U}^-$ and $\mathbf{U}^+$. The electromotive force due to the imposed excitation, which is fully known, is expressed by $\mathbf{U}^-$ and is nonzero only in correspondence of the entries of the primal boundary edges of Σ. The array $\mathbf{U}^+$, on the other hand, is unknown and, in correspondence of the primal edges of Σ, it accounts for the electromotive force due to the wave exiting Ω. Starting from (4.10) and using (4.7) and (4.11), plane wave boundary condition is deduced

$$\begin{aligned} \tilde{\mathbf{F}}^{b} &= \tilde{\mathbf{F}}^{b^+} + \tilde{\mathbf{F}}^{b^-} = \mathbf{M}_Y \mathbf{U}^+ + \tilde{\mathbf{F}}^{b^-} = \\ &= \mathbf{M}_Y (\mathbf{U} - \mathbf{U}^-) + \tilde{\mathbf{F}}^{b^-} = \\ &= \mathbf{M}_Y \mathbf{U} + \mathbf{M}_Y \mathbf{U}^- + \tilde{\mathbf{F}}^{b^-} \\ &= \mathbf{M}_Y \mathbf{U} + 2\tilde{\mathbf{F}}^{b^-}. \end{aligned} \tag{4.12}$$

Finally, by substituting $\tilde{\mathbf{F}}^{b}$ from (4.12) in (3.28) and neglecting the current term, we obtain

$$(\tilde{\mathbf{C}} \mathbf{M}_\nu \mathbf{C} - \omega^2 \mu_0 \varepsilon_0 \mathbf{M}_\varepsilon + i\omega\mu_0 \mathbf{M}_Y)\mathbf{U} = -2i\mu_0 \omega \tilde{\mathbf{F}}^{b^-}, \tag{4.13}$$

which allows to apply a magnetic field excitation, computing the entries $F_i^{b^-}$ of $\tilde{\mathbf{F}}^{b^-}$ as

$$F_i^{b^-} = \int_{\tilde{e}_{b_i}} \boldsymbol{h}^- \cdot d\boldsymbol{l}. \tag{4.14}$$

where $\tilde{e}_{b_i}$ are the boundary dual edges of Σ. Otherwise, if an electric field excitation is desired, (4.9) can be used to obtain

$$\tilde{\mathbf{C}}\mathbf{M}_\nu\mathbf{C} - \omega^2\mu_0\varepsilon_0\mathbf{M}_\varepsilon + i\omega\mu_0\mathbf{M}_Y = 2i\mu_0\omega\mathbf{M}_Y\mathbf{U}^{b^-}, \tag{4.15}$$

and computing the entries $U_i^{b^-}$ of $\mathbf{U}^{b^-}$ as

$$U_i^{b^-} = \int_{e_{b_i}} \boldsymbol{e}^- \cdot d\boldsymbol{l}, \tag{4.16}$$

where e_{b_i} are the primal edges of Σ.

4.2 Equivalent antennas

In some applications it is necessary to have a good representation of the electromagnetic field radiated by an object (like an antenna) only at a certain distance from it, while all what happens near it is of no interest. In this case it is possible to avoid modelling all the details of the object, reducing drastically the number of elements required in the simulation mesh. In this section it will be shown how such a model is built: the idea is to substitute an arbitrarily complex object with a *reference sphere* radiating a field with the same characteristics of the field radiated by the original object. Of course the original field must be computed by other means. In the case of an antenna, simulators like NEC [BP81] can be used. However, the only important thing is to have a way to compute the field produced by the object on the boundaries of the reference sphere.

The proposed model achieves its goal by partitioning the domain Ω in two regions $\Omega_\mathcal{S}$ and $\Omega_\mathcal{T}$ such that $\Omega_\mathcal{S} \cup \Omega_\mathcal{T} = \Omega$ and $\Omega_\mathcal{S} \cap \Omega_\mathcal{T} = \emptyset$. The region $\Omega_\mathcal{S}$ is the one

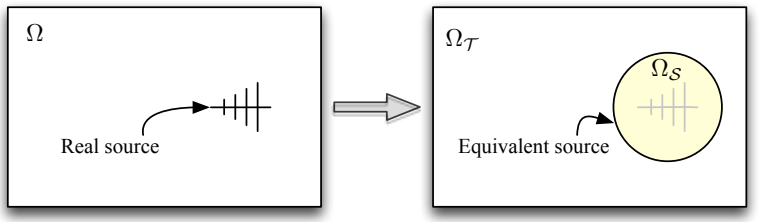

Figure 4.2: The real source (left) is transformed in an empty sphere (right). Because the field of the original source is projected onto the surface of the sphere, it radiates a field equivalent to the original one.

that contains the radiator, while the region $\Omega_\mathcal{T}$ is the remaining part. Moreover, in the region $\Omega_\mathcal{T}$ the *total field* is calculated, while in the region $\Omega_\mathcal{S}$ only the *scattering field* is

computed (Fig. 4.2). This kind of subdivision makes it possible to evaluate the reaction of the environment to the field radiated by the radiator itself. The separation of $\Omega_{\mathcal{T}}$ and $\Omega_{\mathcal{S}}$ is obtained by introducing a *boundary dual grid* [AK07, Cod14] on the interface Σ between the two regions $\Omega_{\mathcal{T}}$ and $\Omega_{\mathcal{S}}$. Associated to this grid are the degrees of freedom of the electromotive forces and the magnetomotive forces on Σ, which account for the "jump" between the scattered field regime and the total field regime. This jump is obtained through proper adjustment of the discrete Maxwell equations and the constitutive relations on the elements of Σ. The adjustment consists in projecting on Σ the fields due to the radiation of the original source: in the following sections it will be shown how the source can be introduced *locally* (i.e. element-wise). Global equations are then obtained by *assembling* the local contributes in the usual way. In the following discussion local quantities will be denoted with the superscript v, except for the matrix $\mathbf{C}$, which we assume the local one unless otherwise noted. Moreover, we choose that the edges of Σ belong to $\Omega_{\mathcal{S}}$. This means that tetrahedra in $\Omega_{\mathcal{S}}$ and touching Σ are the only affected by the modified Maxwell equations shown below. Every other tetrahedra in Ω is treated as usual. This choice mathematically is completely equivalent to its dual (the edges of Σ belong to $\Omega_{\mathcal{T}}$), however it allows for a cleaner and more intuitive software implementation.

4.2.1 Ampère–Maxwell law

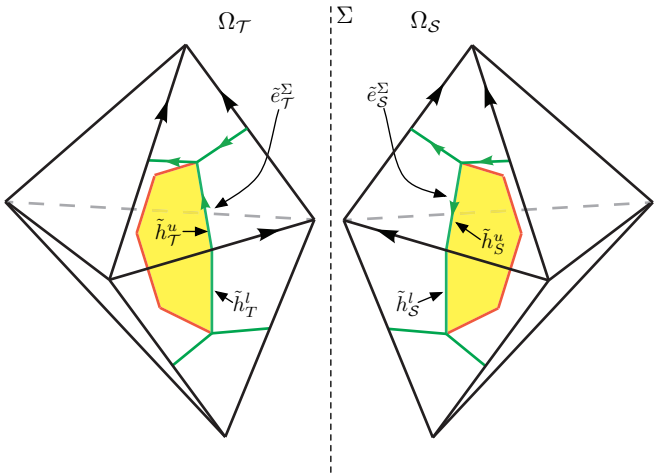

Figure 4.3: A cluster of tetrahedra having Σ in common where *boundary dual edges* are shown. Since half dual edges $\tilde{h}^{u}_{\mathcal{T}}$ and $\tilde{h}^{u}_{\mathcal{S}}$ are the same edge but with opposite orientation, the associated magnetomotive forces $F_{\mathcal{T}}$ and $F_{\mathcal{S}}$ sum to zero. But since $F_{\mathcal{S}} = F_{\mathcal{S}s} + F_{\mathcal{S}r}$, also $F_{\mathcal{T}} + F_{\mathcal{S}s} = -F_{\mathcal{S}r}$ holds.

Consider, in relation to Fig. 4.3, the boundary dual edges $\tilde{e}^{\Sigma}_{\mathcal{T}}$ and $\tilde{e}^{\Sigma}_{\mathcal{S}}$, each spanning two tetrahedra. Both $\tilde{e}^{\Sigma}_{\mathcal{T}}$ and $\tilde{e}^{\Sigma}_{\mathcal{S}}$ can be split in two parts, which we call *half edges*, such that $\tilde{e}^{\Sigma}_{\mathcal{T}} = \tilde{h}^{u}_{\mathcal{T}} \cup \tilde{h}^{l}_{\mathcal{T}}$ and $\tilde{e}^{\Sigma}_{\mathcal{S}} = \tilde{h}^{u}_{\mathcal{S}} \cup \tilde{h}^{l}_{\mathcal{S}}$. Each half edge belongs to a single tetrahedron,

for example $\tilde{h}^u_{\mathcal{T}}$ belongs to the upper tetrahedron in $\Omega_{\mathcal{T}}$ while $\tilde{h}^l_{\mathcal{S}}$ belongs to the lower tetrahedron in $\Omega_{\mathcal{S}}$ (Fig. 4.3). To write the contribute to the Ampère–Maxwell law for the single tetrahedron v, only the half edges belonging to v must be considered. Reasoning on the two upper tetrahedra in Fig. 4.3, Ampère–Maxwell law is obtained by observing that the magnetomotive force $F_{\mathcal{T}}$ on $\tilde{h}^u_{\mathcal{T}}$ and $F_{\mathcal{S}}$ on $\tilde{h}^u_{\mathcal{S}}$ must satisfy the relation $F^{\Sigma}_{\mathcal{T}} + F^{\Sigma}_{\mathcal{S}} = 0$ because $\tilde{h}^u_{\mathcal{T}}$ and $\tilde{h}^u_{\mathcal{S}}$ are in fact the same edge but with opposite orientation. However, since we impose the excitation on the scattering subdomain, the magnetomotive force $F_{\mathcal{S}}$ can be further decomposed in the unknown scattered contribute $F_{\mathcal{S}s}$ and in the known radiated contribute $F_{\mathcal{S}r}$. This implies that the balance of the magnetomotive forces must satisfy the condition $F_{\mathcal{T}} + F_{\mathcal{S}s} = -F_{\mathcal{S}r}$. Thus, the local Ampère–Maxwell law for a tetrahedron v in $\Omega_{\mathcal{S}}$ touching Σ is written as

$$\tilde{\mathbf{C}}\tilde{\mathbf{F}}^v - \tilde{\mathbf{F}}^v_r = i\omega\tilde{\mathbf{\Psi}}^v, \tag{4.17}$$

where the term $\tilde{\mathbf{F}}^v_r$ collects the magnetomotive forces on the half edges of v due to the excitation.

4.2.2 Faraday–Neumann law

To derive the expression for the Faraday–Neumann law, tetrahedra on the interface Σ have to be studied. In particular, two cases are identified:

- Volume element with an edge lying on Σ
- Volume element with a face lying on Σ

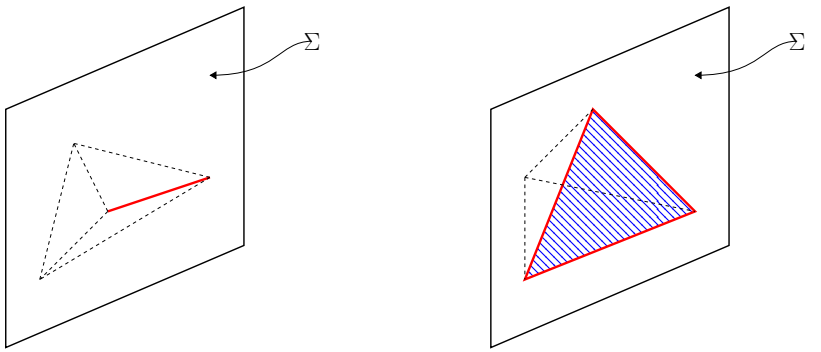

Figure 4.4: The two cases of interest of elements touching Σ: the *edge* case on the left side and the *face* case on the right side.

The case of an edge on Σ

Consider a volume element v lying on Σ, which edges are $e_1, \ldots, e_6$ and their electromotive forces are collected in the array $\mathbf{U}^v = (U^v_1, \ldots, U^v_6)$. Assume, without loss of generality, that the edge on Σ is e_1, so $v \cap \Sigma = e_1$ (Fig. 4.4). The electromotive force U^v_1 on e_1 can be decomposed in a scattering component U^v_{1s}, unknown, and a radiated

component U^v_{1r}, known and due to the radiating element, such that $U^v_1 = U^v_{1s} + U^v_{1r}$. The Faraday–Neumann law accounting for this is written as

$$\mathbf{C}\begin{pmatrix} U^v_{1s}+U^v_{1r} \\ U^v_2 \\ U^v_3 \\ U^v_4 \\ U^v_5 \\ U^v_6 \end{pmatrix} = \mathbf{C}\begin{pmatrix} U^v_{1s} \\ U^v_2 \\ U^v_3 \\ U^v_4 \\ U^v_5 \\ U^v_6 \end{pmatrix} + \mathbf{C}\begin{pmatrix} U^v_{1r} \\ 0 \\ 0 \\ 0 \\ 0 \\ 0 \end{pmatrix} = i\omega\mathbf{\Phi}^v, \tag{4.18}$$

or, in compact array form

$$\mathbf{C}\left(\mathbf{U}^v_r + \mathbf{U}^v_s\right) = i\omega\mathbf{\Phi}^v, \tag{4.19}$$

where the known and unknown quantities are separated.

The case of a face on Σ

Consider a volume element v lying on Σ, the faces of which are $f_1, \ldots, f_4$ and their magnetic fluxes are collected in the array $\mathbf{\Phi}^v = (\phi^v_1, \ldots, \phi^v_4)$. Assume, without loss of generality, that the face on Σ is f_1, so $v \cap \Sigma = f_1$ (Fig. 4.4). Assume also that the edges surrounding f_1 are e_1, e_2, e_3. Both electromotive forces U^v_1, U^v_2, U^v_3 and flux ϕ^v_1 on f_1 can be decomposed in an unknown scattering component and in a known radiated component, obtaining $U^v_k = U^v_{k,s} + U^v_{k,r}$ with $k \in \{1,2,3\}$ and $\phi^v_1 = \phi^v_{1s} + \phi^v_{1r}$. In this case both sides of the Faraday–Neumann law are modified, as follows:

$$\mathbf{C}\begin{pmatrix} U^v_{1s}+U^v_{1r} \\ U^v_{2s}+U^v_{2r} \\ U^v_{3s}+U^v_{3r} \\ U^v_4 \\ U^v_5 \\ U^v_6 \end{pmatrix} = -i\omega\begin{pmatrix} \phi^v_{1s}+\phi^v_{1r} \\ \phi^v_2 \\ \phi^v_3 \\ \phi^v_4 \end{pmatrix}. \tag{4.20}$$

Separating known and unknown quantities and writing the equation in compact form we obtain

$$\mathbf{C}\left(\mathbf{U}^v_r + \mathbf{U}^v_s\right) = -i\omega\left(\mathbf{\Phi}^v_r + \mathbf{\Phi}^v_s\right). \tag{4.21}$$

We note that (4.19) is only a particular case of (4.21) because the last one remains valid also in the first case by setting to zero the radiated contributes of the geometric elements not touching Σ (Fig.4.4).

4.2.3 Constitutive relations

Almost the same reasoning carried out for the Faraday–Neumann law has to be made for the constitutive relations when dealing with volume elements lying on Σ. There are again two cases, the one of the edge on Σ and the one of the face on Σ.

The case of a face on Σ

In this case both electromotive forces and magnetic fluxes are split in radiated and scattered contributes, obtaining

$$\tilde{\mathbf{\Psi}}^v = \mathbf{M}^v_\varepsilon \begin{pmatrix} U^v_{1s}+U^v_{1r} \\ U^v_{2s}+U^v_{2r} \\ U^v_{3s}+U^v_{3r} \\ U^v_4 \\ U^v_5 \\ U^v_6 \end{pmatrix} = \mathbf{M}^v_\varepsilon \begin{pmatrix} U^v_{1s} \\ U^v_{2s} \\ U^v_{3s} \\ U^v_4 \\ U^v_5 \\ U^v_6 \end{pmatrix} + \mathbf{M}^v_\varepsilon \begin{pmatrix} U^v_{1r} \\ U^v_{2r} \\ U^v_{3r} \\ 0 \\ 0 \\ 0 \end{pmatrix}, \tag{4.22}$$

$$\tilde{\mathbf{F}}^v = \mathbf{M}^v_\nu \begin{pmatrix} \phi^v_{1s}+\phi^v_{1r} \\ \phi^v_2 \\ \phi^v_3 \\ \phi^v_4 \end{pmatrix} = \mathbf{M}^v_\nu \begin{pmatrix} \phi^v_{1s} \\ \phi^v_2 \\ \phi^v_3 \\ \phi^v_4 \end{pmatrix} + \mathbf{M}^v_\nu \begin{pmatrix} \phi^v_{1r} \\ 0 \\ 0 \\ 0 \end{pmatrix}, \tag{4.23}$$

or, written in compact form,

$$\tilde{\mathbf{\Psi}}^v = \mathbf{M}^v_\varepsilon(\mathbf{U}^v_s + \mathbf{U}^v_r), \tag{4.24}$$

$$\tilde{\mathbf{F}}^v = \mathbf{M}^v_\nu(\mathbf{\Phi}^v_s + \mathbf{\Phi}^v_r). \tag{4.25}$$

The case of an edge on Σ

As in the case of the Faraday–Neumann law, in this case there are no magnetic fluxes across Σ and only one voltage along an edge on Σ. Constitutive relations (4.24) and (4.25) continue to remain valid by setting to zero the radiated contribute of the entries corresponding to geometric entities not on Σ (Fig. 4.4).

4.2.4 From local equations to the global equation

Until now we reasoned in terms of single mesh volumes, so an assembly phase must be carried out in order to obtain the global equation. Consider (4.17), (4.21), (4.24) and (4.25): by solving (4.17) for $(\mathbf{\Phi}^v_r + \mathbf{\Phi}^v_s)$ then substituting (4.24), (4.17), (4.25) and rearranging, the expression

$$\mathbf{K}^v\mathbf{U}^v_s = -\mathbf{K}^v\mathbf{U}^v_r - i\omega\tilde{\mathbf{F}}^v_r, \tag{4.26}$$

is obtained, where $\mathbf{K}^v = \tilde{\mathbf{C}}\mathbf{M}^v_\nu\mathbf{C} - \omega^2\mathbf{M}^v_\varepsilon$. Assembling element by element in the usual way, the equation

$$\mathbf{K}\mathbf{U} = -\mathbf{K}\mathbf{U}_r - i\omega\tilde{\mathbf{F}}_r, \tag{4.27}$$

is obtained, where all the matrices involved are *global*. The unknowns $\mathbf{U}^v_s$ from (4.26) are now part of the unknown $\mathbf{U}$ in (4.27) and appear in the positions corresponding to the primal edges of Σ. Moreover, the terms $\mathbf{U}_r$ and $\tilde{\mathbf{F}}_r$ are nonzero only in correspondence of the primal edges of Σ and the dual edges of Σ respectively. By introducing the terms due to the impedance boundary conditions and plane wave excitation (4.12), the full

equation is obtained

$$\mathbf{K}\mathbf{U} + i\omega\mathbf{M}_Y = -\mathbf{K}\mathbf{U}_r - i\omega\tilde{\mathbf{F}}_r - 2i\omega\tilde{\mathbf{F}}^{b^-}. \tag{4.28}$$

4.2.5 Numerical validation

Given an antenna of arbitrary shape, radiated electric and magnetic fields can be computed in each point of space by means of tools like NEC or other, more advanced, simulators. In our case we used a dipole, for which the radiated electromagnetic field is known in closed form [Bal05]:

$$E_\theta = \frac{i\eta I_0 e^{-ikr}}{2\pi r}\left[\frac{\cos\left(\frac{kL}{2}\cos\theta\right) - cos\left(\frac{kL}{2}\right)}{\sin\theta}\right], \tag{4.29}$$

$$H_\phi = \frac{E_\theta}{\eta}, \tag{4.30}$$

where η is the impedance of free space, I_0 is the excitation current at the feedpoint, k is the propagation constant, L is the dipole length and r is the distance. In (4.29) and (4.30) it is assumed that the dipole lies along the z axis of a Cartesian reference system and its center is in the origin. However this is not a limitation: in EMT, arbitrary rotations of the virtual dipole are obtained by means of quaternions (see Appendix A). Once the field is known, it can be used to compute the values of the electromotive forces across the primal edges of the interface Σ and the magnetomotive forces across its dual edges by the usual line integration.

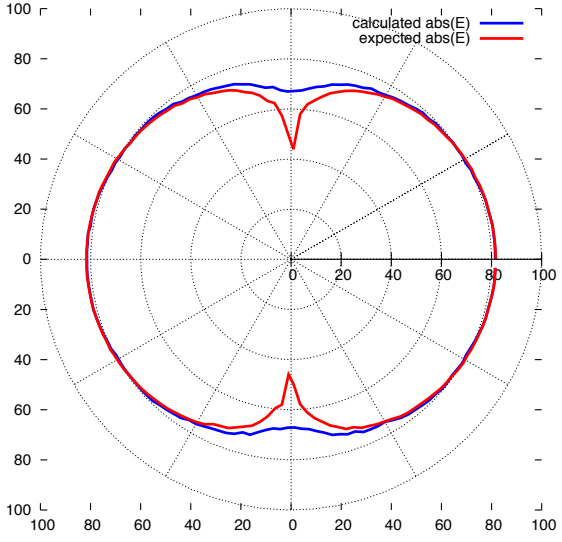

Figure 4.5: Comparison between the expected field and the field produced by the equivalent model at $f = 230$ MHz. The field is expressed in $dB\mu V/m$.

4.2.6 Numerical results

The diameter of the sphere representing the equivalent radiator and the average edge length of tetrahedra in its surroundings must be properly tuned, according to the operating frequency. To obtain reasonable performance, the diameter should be comparable with the wavelength λ and the edge length should be comparable with $\lambda/10$. However, these are only rough indications: in our experiments, a single mesh tuned for the center frequency proved to be adequate between $\lambda = 3.3m$ and $\lambda = 0.77m$. To validate the equivalent model, a cube of side $l = 5m$ was considered, while the radiator was represented by a sphere of radius $r = 0.75m$ placed in the center of the cube. The boundary conditions on the six faces of the cube were set to *impedance boundary condition* with $Z = \sqrt{\mu_0/\epsilon_0}$. Electromagnetic wave propagation problem was solved and the field was evaluated at $r = 2.5m$ (Figure 4.5).

4.3 Waveguide modes

In Section 4.1 it was shown how a *plane wave* source can be modeled in numerical techniques like the DGA. This kind of excitation, however, finds limited application in simulating waveguides. In particular, it can be used for that purpose only at waveguide ports where the contributions of high-order modes can be neglected, otherwise since these modes have different impedances, reflections occur. A more general approach is then required, and the total field/scattered field decomposition already used for equivalent antennas appears to be a good candidate. Waveguide is divided in a scattered field region $\Omega_{\mathcal{S}}$ and a total field region $\Omega_{\mathcal{T}}$ and the excitation is imposed on the interface Σ between them (Figure 4.6). However, we must also deal with the domain truncation which, if not handled, it gives rise to unwanted reflections too. These reflections are avoided by terminating $\Omega_{\mathcal{S}}$ and $\Omega_{\mathcal{T}}$ with PML [Taf98], as depicted in Fig. 4.6. This kind of arrangement allows the presence of multiple modes and also the presence of objects producing scatterings in the surroundings of the interface Σ. In addition, if only the computation of scattered field or total field is needed, the parts of $\Omega_{\mathcal{T}}$ or $\Omega_{\mathcal{S}}$ which are not PML can be omitted without compromising the effectiveness of the method. The excitation is applied on the *interface* Σ between $\Omega_{\mathcal{S}}$ and $\Omega_{\mathcal{T}}$ by means of a dual boundary grid, which allows to access the degrees of freedom $\tilde{\mathbf{F}}^{\Sigma}$ associated to the magnetomotive forces on Σ.

Values of electromotive forces and magnetomotive forces on the primal and dual edges of Σ are calculate according to

$$U_i^{\Sigma} = \int_{e_i} \boldsymbol{e}_m \cdot d\boldsymbol{l} \quad \text{and} \quad F_i^{\Sigma} = \int_{\tilde{e}_i} \boldsymbol{h}_m \cdot d\boldsymbol{l},$$

where $\boldsymbol{e}_m$ and $\boldsymbol{h}_m$ are the fields of the specific mode to be applied on Σ. In case of rectangular or circular waveguides they are known in closed form, however the guide can be of an arbitrary shape. In this last case a 2D eigenvalue problem must be solved in order to determine $\boldsymbol{e}_m$ and $\boldsymbol{h}_m$.

The technique just discussed can be readily transferred to FIT [Wei01], Cell Method [Ton14] and other methods involving dual cell complexes.

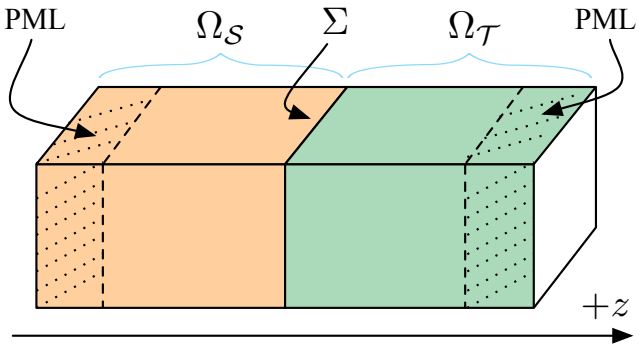

Figure 4.6: Structure used in the simulation of waveguides. In Ω_S the scattered field is computed, while in Ω_T the total field is computed. PML regions absorb waves that otherwise will be reflected by the truncation of the domain.

4.3.1 Numerical results

The simulations were performed with the EMT code on Mac OS X 10.9.5 running on a Core i7 3615QM with 16 GB of RAM, Clang/LLVM 3.5 compiler and MKL PARDISO solver. To test the technique two numerical experiments were prepared. The first one was the simulation of a section of rectangular waveguide (Fig. 4.7), discretized with a mesh that included 178 280 tetrahedra yielding a problem of 192 242 unknowns.

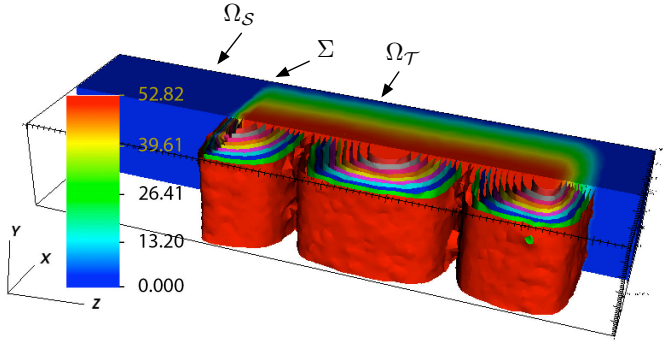

Figure 4.7: The waveguide subject of the simulation is depicted, including PMLs, scattering region Ω_S and total field region Ω_T. The TE_{10} mode excitation is applied on Σ. Dimensions are given in text. Scale shows the magnitude of the electric field in V/m (solid color region).

Such a toy problem was useful to check the correctness of the results against analytic solutions. In this case assembly took 1.84 seconds while solver took 6.44 seconds. The waveguide dimensions were $a = 60$mm (in x direction) and $b = 30$mm (in y direction), which give a cutoff frequency for the TE_{10} mode of about 2.5 GHz. PML regions length was 30mm, and were implemented according to the Uniaxial PML technique, as described in [Taf98]. The length of scattered field region was 30mm and waveguide (total

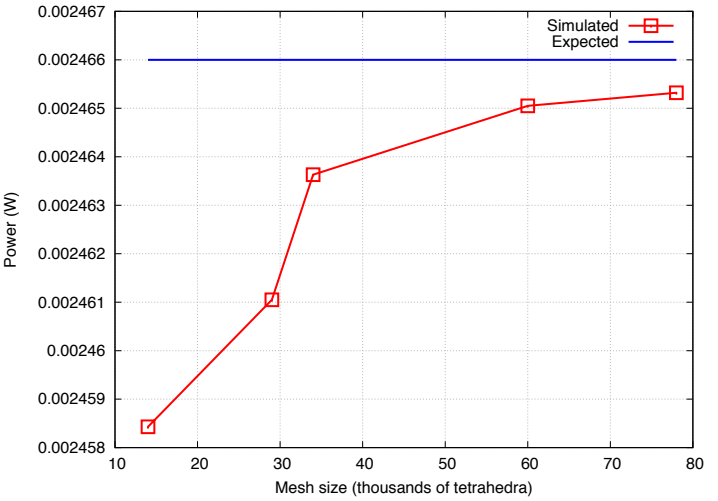

Figure 4.8: Problem 1: Mesh size (number of tetrahedra) vs. power flowing in $\Omega_{\mathcal{T}}$ towards positive z. Simulated power is compared with expected theoretical power.

field) region length was 100mm. Finally, the operating frequency was $f = 3.8$ GHz. The computed field configuration was in accordance with analytic problem solution. As an additional test, power flowing in Σ was computed for different mesh sizes (Fig. 4.8). The flux of the Poynting vector on the interface Σ is computed as

$$P = \frac{1}{2\eta} \boldsymbol{e}_{\Sigma}, \tag{4.31}$$

where $\boldsymbol{e}_{\Sigma}$ is the electric field evaluated on Σ and η is the characteristic impedance of the considered mode.

As a second example, a perfectly conductive sphere of radius $r = 5$mm was placed inside the waveguide of the previous example, near the port providing the TE_{10} excitation (Figure 4.9). In this case operating frequency was $f = 4.7$ GHz. The reflections due to the scatterer are visible in the $\Omega_{\mathcal{S}}$ region depicted in (Figure 4.9) together with the transition from the total field to the scattered field.

The proposed approach was validated against a highly accurate in-house developed FEM code (Fig. 4.10) of the second order and using edge-elements. Our approach has the advantage that, unlike FEM, provides a strong geometrical foundation for the treatment of boundary and interface conditions. The advantage is given by the boundary dual grids (Figure 4.3), which allow the manipulation of all the quantities related to the boundaries of the simulation domain without using interpolation [CCC+15b, CST12, AK07, Cod14].

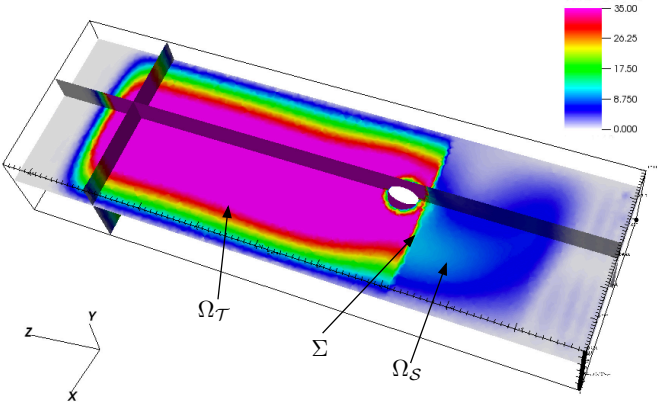

Figure 4.9: Scattering field produced in $\Omega_{\mathcal{S}}$ by a perfectly conductive sphere of radius $r = 5$mm, placed off-center ($x = 25$mm, $y = 20$mm, $z = 67$mm, origin marked O) near the port.

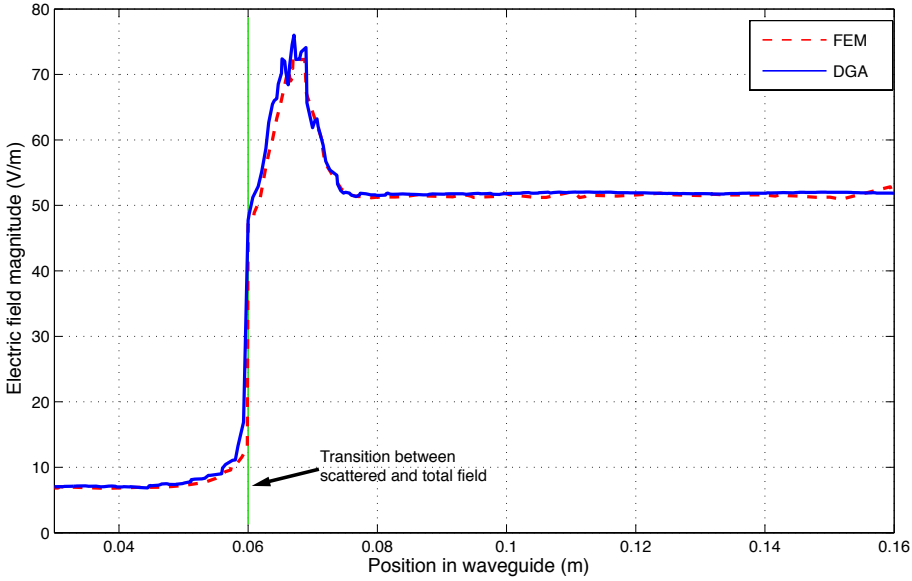

Figure 4.10: Problem 2: The technique was compared against a FEM code. The magnitude of electric field in the scattering and total regions (excluding PML parts) is depicted. Electric field was sampled in the line extending from (0.03, 0.015, 0.03) to (0.03, 0.015, 0.16).

4.4 Current sources

Since DGA makes use of the dual grid and currents are associated to dual faces, it is rather simple to impose current sources. Given a total-field computational domain Ω and a subdomain $\Omega_c \in \Omega$ where a current density $\boldsymbol{j}_c$ is defined, the values of the degrees

of freedom associated to the dual faces in Ω_c are computed as

$$I_i = \int_{\tilde{f}_i} \boldsymbol{j}_c \cdot d\boldsymbol{S},\ \forall \tilde{f}_i \in \Omega_c. \tag{4.32}$$

However, in wave propagation this way of imposing currents is nonphysical because of the skin effect. Currents can be treated more efficiently (in terms of both number of elements and physical accuracy) modelling them as *surface currents*.

A surface current arises when there is a discontinuity in the tangential component of the magnetic field. For example, between the two regions Ω and Ω_c sharing an interface Σ_c, the relation between the current and the magnetic fields is

$$\boldsymbol{n} \times (\boldsymbol{h} - \boldsymbol{h}_c) = \boldsymbol{j}_s. \tag{4.33}$$

If the field in Ω_c is assumed to be zero, the relation above can be rewritten as

$$\boldsymbol{n} \times \boldsymbol{h} = \boldsymbol{j}_s, \tag{4.34}$$

which can be treated as a boundary condition to be applied on Σ_c. In DGA, boundary conditions on the tangential magnetic field are imposed by setting the appropriate values for the degrees of freedom associated to the dual boundary edges. Therefore, cross-multiplying (4.34) by $\boldsymbol{n}$, we can compute the values of the magnetomotive forces on Σ_c due to $\boldsymbol{j}_s$ as

$$F_i = \int_{\tilde{e}_i} \boldsymbol{j}_s \times \boldsymbol{n}\, d\boldsymbol{l},\ \forall \tilde{e}_i \in \Sigma_c. \tag{4.35}$$

Of course, by introducing surface currents, the interior of Ω_c does not need to be meshed.

4.5 Discussion

This chapter described a number of useful electromagnetic sources to be used in the DGA numerical scheme. The most important ones are the Plane Wave boundary condition, the equivalent antenna and the waveguide port condition. With these extensions, the DGA method provides the tools to cover the majority of the needs when a source has to be imposed in a frequency domain wave propagation problem.

5

Alternative formulations

This chapter is devoted to the discussion of other formulations of the electromagnetic wave propagation problem. In particular, the H-field formulation and the $\boldsymbol{A} - V$ formulation are discussed. The first one is *complementary* to the E-field formulation, while the second is somewhat more flexible than the E- or H- field formulation because it allows to access the potentials.

5.1 The H-field formulation

In the previous section the wave equation (3.8) was derived from Maxwell's equations (3.3) and (3.4). The unknown quantity in (3.8) is the complex-valued vector function $\boldsymbol{e}$. However, an alternative wave equation can be derived by solving (3.4) for $\boldsymbol{e}$ and substituting. The equation for the H-field formulation is

$$\nabla \times \boldsymbol{\xi} \nabla \times \boldsymbol{h} - \omega^2 \varepsilon_0 \mu_0 \boldsymbol{\mu} \boldsymbol{h} = \varepsilon_0 \nabla \times \boldsymbol{\xi} \boldsymbol{j}, \tag{5.1}$$

where the unknown quantity is now the complex-valued vector function $\boldsymbol{h}$ and $\boldsymbol{\xi} = \boldsymbol{\varepsilon}^{-1}$. Having both formulations (3.8) and (5.1) seems to be *apparently* useless, since (5.1) gives the same information as (3.8): electric field $\boldsymbol{e}$ is readily recovered by plugging the resulting $\boldsymbol{h}$ and the source $\boldsymbol{j}$ in

$$\boldsymbol{e} = \boldsymbol{\xi} \frac{\nabla \times \boldsymbol{h} - \boldsymbol{j}}{i\omega}. \tag{5.2}$$

However, this is true only in the continuous setting. In the discrete setting, as we will see, the recovered electric field is slightly different from the one obtained with the discrete E-field formulation. This feature of the discrete formulations will be exploited to devise an adaptive refinement scheme, as will be detailed in Section 5.2. The E-field formulation and the H-field formulation are thus said to be *complementary* and, as already discussed in Section 2.1, are part of a topic of great interest. We will investigate the topic by using the two formulations to build an adaptive refinement scheme based on the approximation lying in the constitutive laws [GTB94]. As already discussed

in Chapter 2, discrete constitutive equations are only approximate: the comparison of the error made by the two formulations gives a good indication about where the mesh requires refinement.

Boundary conditions Also in the H-field formulations we have PEC, PMC and radiation boundary conditions. However, they are applied differently. In particular, the PEC condition is now applied as a Neumann-type boundary condition, while the PMC condition is a Dirichlet-type condition. This will be evident after the discussion of the discrete formulation: since the magnetic field in the H-field formulation will be associated to the primal edges, forcing to zero an unknown associated to a boundary primal edge means that the tangent component of magnetic field is zero there. Similarly, the same happens for the electric field, associated to the dual edges. Moreover, in the case of the radiation condition, admittance appeared in the E-field formulation, while impedance appears in H-field formulation.

5.1.1 Discrete H-field problem

In the DGA framework the H-field formulation is obtained by swapping the role of the simplicial and the barycentric grids. Maxwell equations are then rewritten as

$$\tilde{\mathbf{C}}\tilde{\mathbf{U}} = -i\omega\tilde{\mathbf{\Phi}}, \tag{5.3}$$

$$\mathbf{C}\mathbf{F} = i\omega\mathbf{\Psi} + \mathbf{I}, \tag{5.4}$$

$$\mathbf{D}\mathbf{\Psi} = \mathbf{Q}, \tag{5.5}$$

$$\tilde{\mathbf{D}}\tilde{\mathbf{\Phi}} = \mathbf{0}. \tag{5.6}$$

This leads to the association of magnetic voltages with the edges of a primal simplicial grid and of the electromotive forces with the edges of the dual barycentric grid. Using the same procedure used to obtain the E-field discrete wave propagation equation, we can obtain

$$(\tilde{\mathbf{C}}\mathbf{M}_\xi\mathbf{C} + \omega^2\mu_0\varepsilon_0\mathbf{M}_\mu)\mathbf{F} = \varepsilon_0\mathbf{C}\mathbf{M}_\xi\mathbf{I}. \tag{5.7}$$

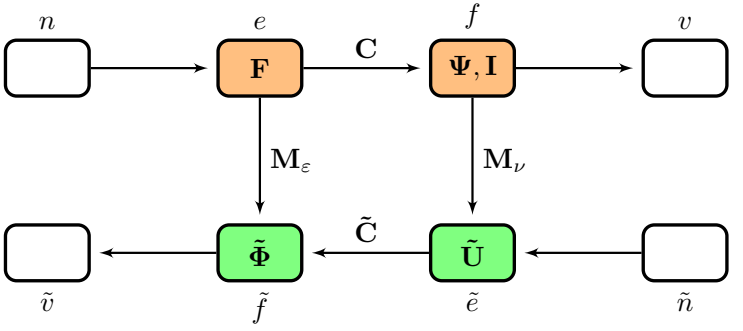

Figure 5.1: Tonti's diagram of the H-field formulation. With respect to Figure 3.2, the role of the geometric elements is exchanged.

5.1.2 The impedance boundary condition

At a boundary $\partial\Omega$ where an impedance boundary condition with characteristic impedance Z is desired, the equation

$$Z(r)((\boldsymbol{n}\times\boldsymbol{h})\times\boldsymbol{n}) = \boldsymbol{n}\times\boldsymbol{e}, \tag{5.8}$$

must hold. Moreover, for the properties of the boundary element basis functions $\boldsymbol{v}_i^{e^b}(\boldsymbol{r})$ [CST12], the equation

$$(\boldsymbol{n}\times\boldsymbol{h})\times\boldsymbol{n} = \sum_{i=0}^{\mathcal{E}} \boldsymbol{v}_i^{e^b}(\boldsymbol{r})F_i^b, \tag{5.9}$$

holds.

5.1.3 Impedance constitutive matrix

The constitutive impedance matrix $\mathbf{M}_Z$ is obtained by the energetic approach [CST12, CT05] in a way similar to the one used to derive $\mathbf{M}_Y$. Let $\boldsymbol{e'}$ and $\boldsymbol{h}$ be two independent fields. We compute the flux of the vector $\boldsymbol{e'}\times\boldsymbol{h}$ across the surface $\partial\Omega$:

$$\begin{aligned}
\int_{\partial\Omega} \boldsymbol{e'}\times\boldsymbol{h}^*\cdot\boldsymbol{n}ds &= \int_{\partial\Omega} \boldsymbol{n}\times\boldsymbol{e'}\cdot\boldsymbol{h}^* ds = \\
&= \int_{\partial\Omega} (\boldsymbol{n}\times\boldsymbol{e'})\cdot(\boldsymbol{n}\times\boldsymbol{h}\times\boldsymbol{n})^* ds = \\
&= \int_{\partial\Omega} (\boldsymbol{n}\times\boldsymbol{e'})\cdot(\sum_{i=0}^{\mathcal{E}} \boldsymbol{v}_i^{e^b}(\boldsymbol{r})F_i^b)^* ds = \\
&= \sum_{i=0}^{\mathcal{E}} F_i^{b^*} \int_{\partial\Omega} (\boldsymbol{n}\times\boldsymbol{e'})\cdot\boldsymbol{v}_i^{e^b}(\boldsymbol{r}) ds = \\
&= \sum_{i=0}^{\mathcal{E}} F_i^{b^*} \int_{\partial\Omega} (\boldsymbol{v}_i^{e^b}(\boldsymbol{r})\times\boldsymbol{n})\cdot\boldsymbol{e'} ds = \\
&= -\sum_{i=0}^{\mathcal{E}} F_i^{b^*} \int_{\partial\Omega} (\boldsymbol{n}\times\boldsymbol{v}_i^{e^b}(\boldsymbol{r}))\cdot\boldsymbol{e'} ds = \\
&= -\sum_{i=0}^{\mathcal{E}} F_i^{b^*} \sum_{j=0}^{\mathcal{F}} \int_{f_j^b} (\boldsymbol{n}\times\boldsymbol{v}_i^{e^b}(\boldsymbol{r}))\cdot\boldsymbol{e'} ds = \\
&= -\sum_{i=0}^{\mathcal{E}} F_i^{b^*} U_i^b = -\boldsymbol{F}^{b'^H}\boldsymbol{U}^{\boldsymbol{b'}}.
\end{aligned} \tag{5.10}$$

As opposed to admittance boundary condition, a minus sign appears, and it can be explained as following: the edges e^b and $\tilde{e}^b$ belonging to $\partial\Omega$ (Figure 5.2) are always oriented such that the vector $e^b\times\tilde{e}^b$ has the same orientation as $\boldsymbol{n}$. In the E-field formulation, since the *emf*s are associated to the primal edges while the *mmf*s are associated to the dual edges, the vector $\boldsymbol{e'}\times\boldsymbol{h}$ has also the same orientation as $\boldsymbol{n}$. In

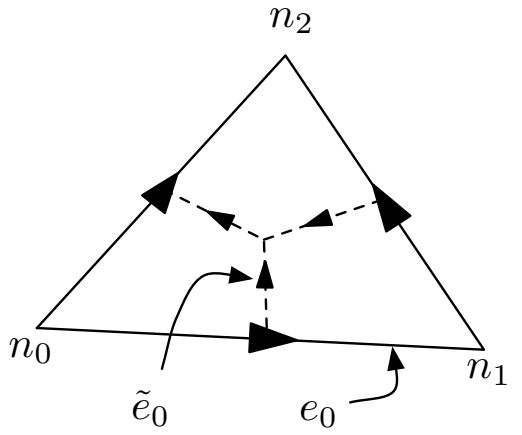

Figure 5.2: Orientation of the edges on a boundary $\partial\Omega$. When $\boldsymbol{e}$ is associated to primal edges and $\boldsymbol{h}$ to the dual edges, $e_i^b \times \tilde{e}_i^b$ and $\boldsymbol{e} \times \boldsymbol{h}$ have the same orientation. Swapping the grids, $e_i^b \times \tilde{e}_i^b$ has the orientation of $\boldsymbol{h} \times \boldsymbol{e}$ = -($\boldsymbol{e} \times \boldsymbol{h}$).

the H-field formulation, having exchanged the roles of $\mathcal{G}$ and $\tilde{\mathcal{G}}$, the *emf*s are associated to the dual edges $\tilde{e}^b$ while the *mmf*s to the primal edges e^b. As a consequence, in the H-field formulation the vector $\boldsymbol{e'} \times \boldsymbol{h}$ has the orientation of $-\boldsymbol{n}$ while $e^b \times \tilde{e}^b$ has the orientation of $\boldsymbol{n}$ and thus the minus sign is required. We proceed by using (5.8) and (5.9) to obtain

$$\int_{\partial\Omega} \boldsymbol{e'} \times \boldsymbol{h}^* \cdot \boldsymbol{n} ds = \tag{5.11}$$

$$= \int_{\partial\Omega} \left(Z(\boldsymbol{r}) \sum_{i=0}^{\mathcal{E}} \boldsymbol{v}_i^{e^b}(\boldsymbol{r}) F_i^b \right) \left(\sum_{j=0}^{\mathcal{E}} \boldsymbol{v}_j^{e^b}(\boldsymbol{r}) F_j^b \right)^* = \tag{5.12}$$

$$= \boldsymbol{F}^{b^H} (\mathbf{M}_{\boldsymbol{Z}} \boldsymbol{F}^b) \tag{5.13}$$

so $\boldsymbol{U}^b = -\mathbf{M}_{\boldsymbol{Z}} \boldsymbol{F}^b$ holds. The entries of the impedance matrix are finally calculated as

$$(\mathbf{M}_Z)_{ij} = \int_{\partial\Omega} Z(\boldsymbol{r}) (\boldsymbol{v}_i^{e^b}(\boldsymbol{r}) \cdot \boldsymbol{v}_j^{e^b}(\boldsymbol{r})) ds. \tag{5.14}$$

To introduce the impedance boundary condition together with the plane wave excitation in (5.1), it is sufficient to carry out the same reasoning employed in the E-field case. In this case, electromotive forces on boundary edges need to be considered in the Faraday–Neumann law as

$$\tilde{\mathbf{C}}\tilde{\mathbf{U}} - \tilde{\mathbf{U}}^b = -i\omega\tilde{\mathbf{\Phi}}, \tag{5.15}$$

obtaining the new H-field wave propagation problem

$$(\tilde{\mathbf{C}}\mathbf{M}_\xi\mathbf{C} - \omega^2\mu_0\varepsilon_0\mathbf{M}_\mu + i\omega\varepsilon_0\mathbf{M}_Z)\mathbf{F} = 2i\varepsilon_0\omega\tilde{\mathbf{U}} + \varepsilon_0\tilde{\mathbf{C}}\mathbf{M}_\xi\mathbf{I}. \tag{5.16}$$

5.2 An adaptive refinement scheme

It is a known fact that in the discrete domain constitutive laws are approximated and thus $\boldsymbol{b}$ is not equal to $\boldsymbol{\mu h}$, as well as $\boldsymbol{d}$ is not equal to $\boldsymbol{\epsilon e}$. For this reason, as already noted by Bossavit, "*this inconsistency in the constitutive laws can be used as an error estimator*" [GTB94]. Thus we propose an adaptive mesh refinement scheme based on the comparison of the electromagnetic energies calculated from the E-field formulation and H-field formulation. The main idea behind the scheme is to refine the mesh in the subregions of Ω where the relative error between calculated energies is maximal (Fig. 5.5), since "*subdivision of the guilty elements and their neighbors, cannot fail to improve the result*" [Bos98a, pp. 336-337]. The entire idea can be summarized in the following iterative procedure:

1. solve problems (3.24) and (5.7),
2. interpolate fields in the mesh volumes v_i with piecewise constant basis functions [CT05], obtaining:
   - primal fields $\boldsymbol{e}_{p,i}$, $\boldsymbol{h}_{p,i}$,
   - dual fields $\boldsymbol{e}_{d,i}$ and $\boldsymbol{h}_{d,i}$.
3. for each v_i, let:
   - $\Delta\boldsymbol{e}_i \;=\; \boldsymbol{e}_{p,i} \;-\; \boldsymbol{e}_{d,i}$,
   - $\Delta\boldsymbol{h}_i \;=\; \boldsymbol{h}_{p,i} \;-\; \boldsymbol{h}_{d,i}$,

   then compute
   $$\Delta w_i = \delta \int_{v_i} \Delta\boldsymbol{e}_i \cdot \epsilon\Delta\boldsymbol{e}_i \, dv \;+\; (1-\delta) \int_{v_i} \Delta\boldsymbol{h}_i \cdot \mu\Delta\boldsymbol{h}_i \, dv. \tag{5.17}$$
   The quantity Δw_i represents the absolute energy error between the two formulations in the ith element, while δ is a coefficient in range $[0, \ldots, 1]$.
4. let $\mathcal{T}$ be the set of the tetrahedra in which Ω is discretized:
   - compute
   $$w_{p,i} = \delta \int_{v_i} \boldsymbol{e}_{p,i} \cdot \epsilon\boldsymbol{e}_{p,i} \, dv + (1-\delta) \int_{v_i} \boldsymbol{h}_{p,i} \cdot \mu\boldsymbol{h}_{p,i} \, dv,$$
   - compute the relative error $\eta(t) = \Delta w_i / w_{p,i}$ for each $v_i \in \mathcal{T}$.
5. assign the tetrahedra of Ω to two sets $\mathcal{T}_h$ and $\mathcal{T}_l$, where the first set contains the $k \cdot 100\%$ of the tetrahedra and maximizes the error, while the second set contains the other tetrahedra. Otherwise stated:
   let $k \in [0,1]$ and $\eta(\mathcal{X}) = \sum_{x \in \mathcal{X}} \eta(x)$:
   (a) make a set $\mathcal{T}_h \subset \mathcal{T}$ such that
   $card\,(\mathcal{T}_h) = k \cdot card\,(\mathcal{T})$ and $\eta(\mathcal{T}_h)$ is maximized,

(b) make a set $\mathcal{T}_l = \mathcal{T} \setminus \mathcal{T}_h$ that contains the remaining tetrahedra,

6. for each tetrahedron $v_i \in \mathcal{T}_h$, divide its radius by r_h,

7. for each tetrahedron $v_i \in \mathcal{T}_l$, divide its radius by r_l.

Good results were obtained by setting $k = 0.1$, $r_h = 3$ and $r_l = 1.2$. The *error weighting coefficient* δ is used to privilege the magnetic energy error ($\delta = 1$) or the electric energy error ($\delta = 0$) in the refinement process. In the first case the refinement captures the rapid variations of $\boldsymbol{e}$, while in the second case the rapid variations of $\boldsymbol{h}$. This could be useful in some cases, for example in presence of strong standing waves (Fig. 5.3).

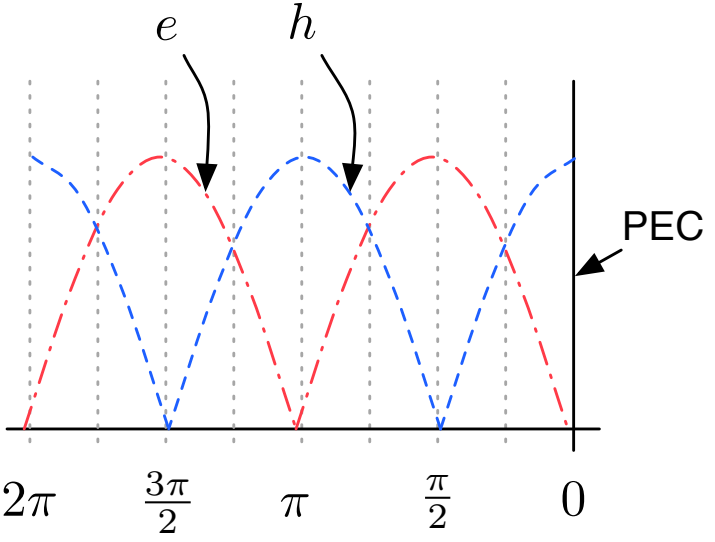

Figure 5.3: Standing wave that forms when a plane wave hits a PEC wall. If magnetic field is the quantity of interest, refinement should be done around $\frac{\pi}{2}$ and $\frac{3\pi}{2}$, where the field variations are higher. Electric field, however, would require maximal refinement around 0, π and 2π. Thus, setting $\delta = 0.5$, would lead to a rather uniform refinement while setting $\delta = 0$ or $\delta = 1$ will favour magnetic field or electric field respectively.

The proposed algorithm uses relative error to detect the areas that need to be refined however, even though this worked in the analyzed cases, this can result in a bad choice for certain field configurations, in particular when very high differences in the field magnitude are present. In these cases absolute error can be a better choice, and is selected by choosing $w_{p,i} = 1$ in the step 4 of the algorithm.

5.2.1 Numerical results

We investigated numerically, for a number of wave propagation problems, the convergence behaviour of the two formulations by calculating some energetic quantities at each

refinement step, specifically the electric energy

$$w_e = \frac{1}{4}\int_\Omega \epsilon|\boldsymbol{e}|^2 dv, \tag{5.18}$$

and the magnetic energy

$$w_m = \frac{1}{4}\int_\Omega \mu|\boldsymbol{h}|^2 dv, \tag{5.19}$$

As an example (Fig. 5.4), the electric energy of a plane wave travelling in a box of $1m \times 1m \times 1m$ and with an interface with $\Gamma = 0.25$ at the end was calculated. At the

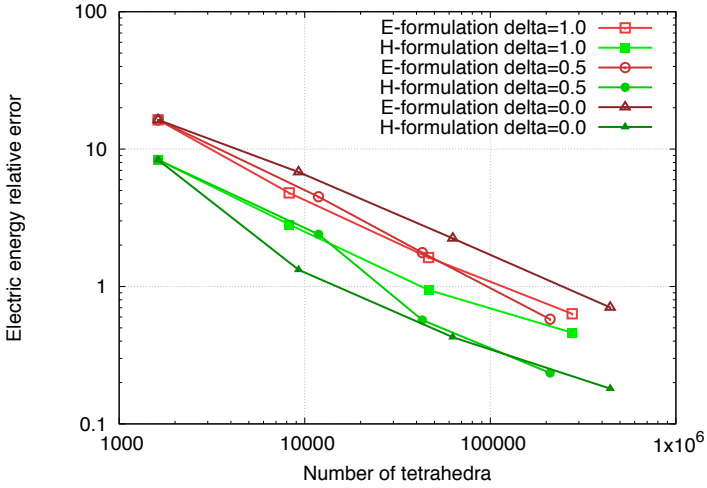

Figure 5.4: Comparison of electric energy convergence of the two formulations using different error weighting coefficients: number of tetrahedra vs. absolute energy error. The expected electric energy value is $w_e = 2.35 \cdot 10^{-12}$ J.

second step the refinement procedure produced a mesh of about 8000 elements in the cases $\delta = 0$ and $\delta = 1$, while it produced a mesh of about 12000 elements with $\delta = 0.5$ (uniform refinement). In the case where $\delta = 1$ we observed almost the same accuracy of the case $\delta = 0.5$, despite a 33% reduction of the number of elements (Fig. 5.4). At the third step the procedure produced a mesh of about 44000 elements in the cases where $\delta = 1$ and $\delta = 0.5$, while it produced a mesh of about 62000 elements in the case $\delta = 0$; with equal number of elements the refinement based on electric energy error is slightly more precise than uniform refinement. Such test problem was chosen to have analytic expressions for the energetic quantities, however the same behaviour was observed in more complex problems, as for example in waveguides with scattering objects inside (Fig. 5.5), thus suggesting some effectiveness of the proposed technique.

Energetic quantities across the domain boundaries were also calculated but, despite the calculation converges to the correct value, inconclusive results were obtained (Fig. 5.6).

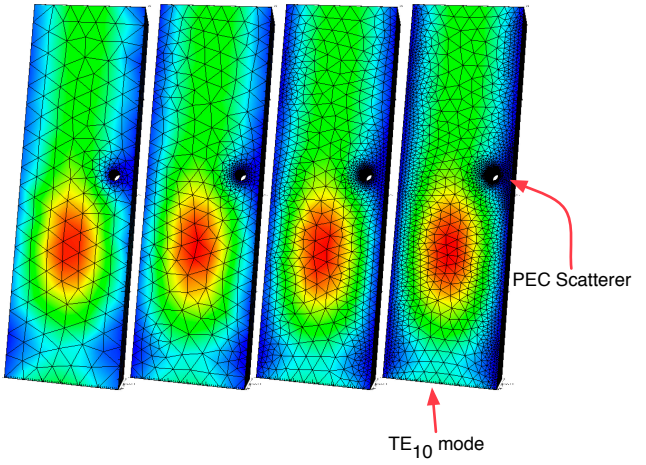

Figure 5.5: Four steps of adaptive mesh refinement on a section of rectangular waveguide excited with TE_{10} mode and a scatterer inside. Parameters were $r_h = 3.0, r_l = 1.2, \delta = 1.0$. The adaptive scheme correctly refines the mesh near boundaries, where the variation of the field is higher.

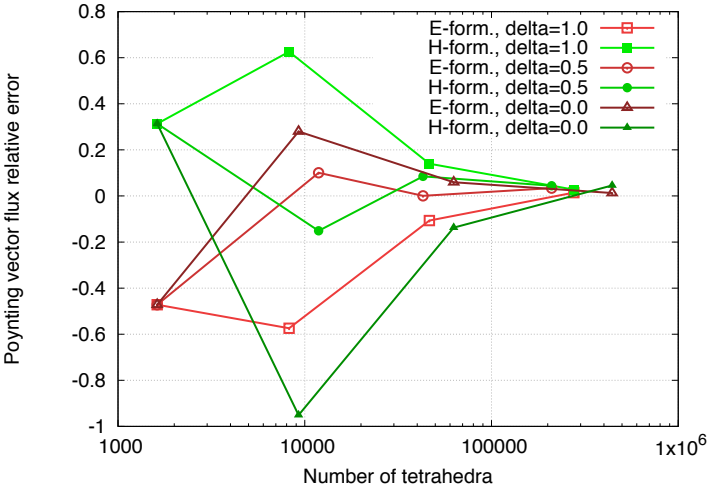

Figure 5.6: Comparison of Poynting vector flux convergence of the two formulations using different error weighting coefficients: number of tetrahedra vs. absolute flux error. The expected power flowing across $\partial\Omega$ is $1.244 \cdot 10^{-3}$ W.

5.3 The A-V formulation

The $\boldsymbol{A} - V$ formulation is perhaps the most general formulation that can be used for the solution of electromagnetic problems. Its applicability ranges from classical electrodynamics to quantum mechanics and, for this reason, is of great interest [Che14]. Moreover, exploiting the well known Helmholtz theorem to split the electromagnetic field generated by current $\boldsymbol{j}$ and charge ρ in an irrotational part and a solenoidal part, it simplifies a lot the calculation of the electromagnetic field [Mid03], [Pap88] and [Che14].

From a numerical point of view, the $\boldsymbol{A} - V$ formulation is interesting because it permits to directly access the potentials, allowing for example to apply voltage excitation to antennas. The drawback is that the number of unknowns is larger than in E-field formulation (for tetrahedral meshes between 1.2 and 1.3 times larger), however this problem can be mitigated by particular gaugings, for example the $\boldsymbol{A}^*$ gauge.

5.3.1 Derivation of the formulation

Since the Gauss magnetic law (3.2) establishes the solenoidal nature of the magnetic field, $\boldsymbol{b}$ can be written in terms of a magnetic vector potential $\boldsymbol{a}$. The vector potential is related to the magnetic induction field $\boldsymbol{b}$ as

$$\boldsymbol{b} = \nabla \times \boldsymbol{a}. \tag{5.20}$$

Because $\nabla \cdot (\nabla \times \boldsymbol{a}) = \boldsymbol{0}$ holds for every field $\boldsymbol{a}$, (3.2) is always satisfied. Substituting (5.20) in the Faraday–Neumann law (3.3), the relation

$$\nabla \times \boldsymbol{e} = -i\omega \nabla \times \boldsymbol{a}, \tag{5.21}$$

is obtained, which can be rearranged and rewritten as

$$\nabla \times (\boldsymbol{e} + i\omega \boldsymbol{a}) = \boldsymbol{0}. \tag{5.22}$$

This last result shows that the quantity $\boldsymbol{e} + i\omega\boldsymbol{a}$ is irrotational and, if the domain under study is simply connected, it can be derived from a scalar potential function ϕ, resulting in the following expression for $\boldsymbol{e}$

$$\boldsymbol{e} = -i\omega \boldsymbol{a} - \nabla V, \tag{5.23}$$

which always satisfies the Faraday–Neumann law (3.3). Electric and magnetic fields can then be derived from (5.20) and (5.23). However, the other two Maxwell equations remain to be satisfied. Using the constitutive relations, (5.20) and (5.23) are substituted in (3.4) and (3.1), obtaining the so-called ungauged $\boldsymbol{A} - V$ formulation

$$\nabla \times \boldsymbol{\mu}^{-1} \nabla \times \boldsymbol{a} - \omega^2 \boldsymbol{\varepsilon} \boldsymbol{a} - i\omega \boldsymbol{\varepsilon} \nabla V = \boldsymbol{j}, \tag{5.24}$$

$$-i\omega \nabla \cdot \boldsymbol{\varepsilon} \boldsymbol{a} - \nabla \cdot \boldsymbol{\varepsilon} \nabla V = \rho. \tag{5.25}$$

From an algebraic point of view, the equations of the $\boldsymbol{A} - V$ formulation appear to be far more complicated than the ones of the E- and H- field formulations, however by applying the opportune gauge transformations (Coulomb gauge or Lorenz gauge),

(5.24) and (5.25) can be reduced to a pair of uncoupled Helmholtz equations of much simpler solution. The usual boundary conditions can be applied to (5.24) and (5.25), in particular:

- Dirichlet condition $\boldsymbol{n} \times \boldsymbol{a} = \boldsymbol{0}, V = 0$, which is the perfect electric conductor,
- Dirichlet condition on the potentials $V = V_0$, which represents a voltage source,
- Neumann condition $\boldsymbol{n} \times \boldsymbol{h} = \boldsymbol{0}$, which is the perfect magnetic conductor,
- Impedance condition $Z\boldsymbol{h}_t = \boldsymbol{n} \times \boldsymbol{e}_t$.

5.4 A-V formulation in DGA

Equations (5.24) and (5.25) can be directly translated to the discrete domain as

$$(\tilde{\mathbf{C}}\mathbf{M}_\nu\mathbf{C} - \omega^2\mathbf{M}_\varepsilon)\mathbf{A} - i\omega\mathbf{M}_\varepsilon\mathbf{G}\mathbf{V} = \tilde{\mathbf{I}}, \tag{5.26}$$

$$i\omega\tilde{\mathbf{D}}\mathbf{M}_\varepsilon\mathbf{A} + \tilde{\mathbf{D}}\mathbf{M}_\varepsilon\mathbf{G}\mathbf{V} = \tilde{\mathbf{Q}}, \tag{5.27}$$

which are equivalent to the symmetric linear system

$$\begin{pmatrix} \tilde{\mathbf{C}}\mathbf{M}_\nu\mathbf{C} - \omega^2\mathbf{M}_\varepsilon & -i\omega\mathbf{M}_\varepsilon\mathbf{G} \\ i\omega\tilde{\mathbf{D}}\mathbf{M}_\varepsilon & \tilde{\mathbf{D}}\mathbf{M}_\varepsilon\mathbf{G} \end{pmatrix} \begin{pmatrix} \mathbf{A} \\ \mathbf{V} \end{pmatrix} = \begin{pmatrix} \tilde{\mathbf{I}} \\ \tilde{\mathbf{Q}} \end{pmatrix}. \tag{5.28}$$

The unknowns of the array $\mathbf{A}$ are associated to the primal edges, while the unknowns of the array $\mathbf{V}$ are associated to the primal nodes. Boundary conditions can be applied as usual, however admittance condition is now written as $\tilde{\mathbf{F}}^b = -\mathbf{M}_Y(i\omega\mathbf{A} + \mathbf{G}\mathbf{V})$.

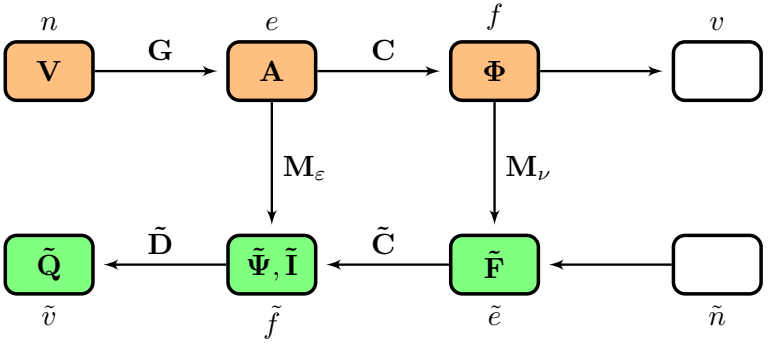

Figure 5.7: Tonti's diagram of the A-V formulation.

III

Applications

6

Applications to Electromagnetic Compatibility Testing

This chapter is dedicated to a discussion on how to apply the developed techniques to the simulation of entire anechoic chambers. The chapter starts by discussing how to use the port boundary condition to simulate a piece of anechoic wall to study its electromagnetic properties. Understanding a small piece of the wall will allow us to derive its equivalent impedance and then to obtain a simplified equivalent model. Then, the modeling of the antennas is discussed and the results of Section 4.2 will be used to derive equivalent antenna models. In a subsequent section two numerical models of two different chambers with transmitters inside are shown. The models reflect real experiments that were made at Emilab, an EMC lab in Amaro, near Udine. Experiments are then discussed and their results are compared with the numerical simulations. Finally, a discussion about using numerical simulations to validate measurements is made.

6.1 Study of anechoic chamber walls

Anechoic chamber walls present a rich geometry, being composed by a large number of absorbing cones and ferrite tiles (Fig. 6.1). Absorbing cones are made by a special foam with embedded graphite and are used to absorb high frequency radiation (above $\sim$ 1 GHz), while ferrite tiles absorb low frequency radiation. A whole anechoic wall can be imagined as composed by a number of basic elements, which we call *unitary cells* (Fig. 6.1) and which consist of four distinct regions: from left to right, the first region represents the air in front of the cones, the second accommodates the absorbing cones, the third is air again and the fourth is where the ferrite tiles are placed. An anechoic wall is then a rather complex object, which is almost impossible to simulate in its entirety because of the already mentioned numerical and mathematical issues arising when solving wave propagation problems. We are then looking for a far simpler

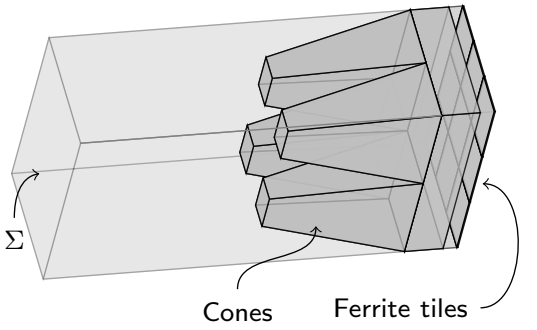

Figure 6.1: The *unitary cell*, which consists of the surface Σ where excitation is applied, air (light gray), cones (dark gray) and ferrites (surface at the right).

equivalent model able to represent an anechoic wall with quite good accuracy. Since the purpose of an anechoic wall is to look like free space to electromagnetic radiation, our idea is to substitute the whole wall with a boundary condition simulating the impedance of the free space. However the anechoic wall is not perfect and it does not look exactly like free space, thus we need a method to determine the right equivalent impedance frequency by frequency.

6.1.1 Obtaining the equivalent wall model

The equivalent impedance of an entire wall can computed by simulating just the unit cell. With reference to Fig. 6.1, in the simulation the leftmost surface Σ represents a plane wave source, where a plane wave of angular frequency ω and wave vector normal to Σ is forced. Moreover, electric field is directed from the bottom to the top of the cell. Above and below the cell a PEC boundary condition is imposed, while on the sides a PMC condition is imposed. This arrangement of conditions acts like a *periodic boundary condition* so, studying the unitary cell is equivalent to study an infinite wall. The whole arrangement forms the computational domain Ω where the numerical problem is defined. The numerical simulation of the unitary cell under the conditions just described allows to compute the wave impedance on a plane Π (Fig. 6.2) parallel to Σ, internal to Ω and not intersecting the cone region.

Wave impedance calculation

Once the problem (4.13) is solved in the domain Ω representing the unitary cell, wave impedance can be calculated everywhere in Ω. In our application it is calculated on a plane Π placed at $z = 0$, parallel to the boundary wall (Fig. 6.2). A grid of 20×20 points was defined on the plane Π and then the tetrahedrons containing these points were identified. For each tetrahedron $T_1, \ldots, T_n$ wave impedance values $Z_1, \ldots, Z_n$ were

calculated. Finally, wave impedance on Π was obtained from

$$Z_{\Pi} = \frac{1}{n}\sum_{i=1}^{n} Z_n, \tag{6.1}$$

where the average is performed for numerical robustness reasons. Using a standard formula from transmission line theory, Z_{Π} on Π was then translated to the right side of the unitary cell, obtaining $Z_{\Pi'}$ [Col]

$$Z_{\Pi'}(z) = Z_c \frac{Z_{\Pi} - iZ_c \tan(\beta z)}{Z_c - iZ_{\Pi} \tan(\beta z)}, \tag{6.2}$$

where $Z_c = \sqrt{\mu/\epsilon}$ is the characteristic impedance of the space where the wave propagates. $Z_{\Pi'}(z)$ is a function of z, the distance of Π' from Π. This impedance translation is needed to have an equivalent model with the same physical dimensions of the non-equivalent one.

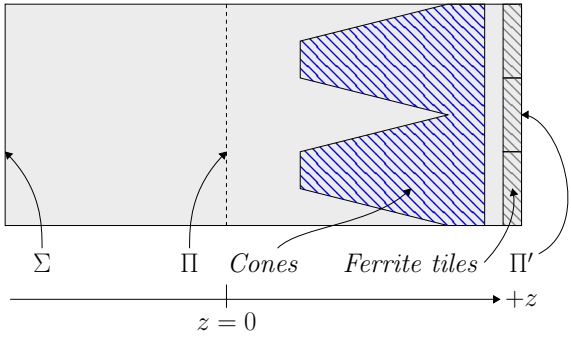

Figure 6.2: Sectional view of the cone-ferrite assembly. The excitation Σ, the impedance calculation plane Π and the impedance de-embedding plane Π' are indicated.

6.1.2 Numerical results

Two models of the unitary cell were developed, one with full details and one composed entirely by air and terminated by an impedance calculated as in (6.2). Moreover, the mesh for the first model was chosen in order to have some tens of elements per wavelength and to represent with good accuracy all the geometric features, while the second model was chosen just to have at least 10 elements per wavelength.

Simulation was performed on the first model, imposing a plane wave excitation on Σ with an incident electric field of 1 V/m. Wave impedance was computed on the plane Π, sampling Π on 400 evenly spaced points distributed on the already mentioned 20×20 grid. Impedance $Z_{\Pi'}$ was then calculated according to (6.2) and used as boundary condition on the second, simplified model. Finally the excitation condition was used again to impose a plane wave with the same characteristics of the previous experiment on the boundary Σ of the simplified model. The resulting electric fields were then

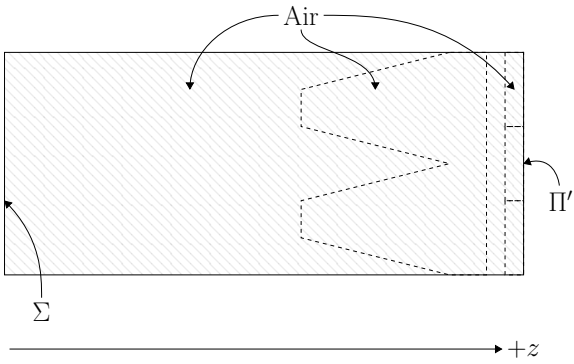

Figure 6.3: Sectional view of the equivalent model. The whole volume of the equivalent cell is made of air and the de-embedded impedance condition is applied on the plane Π'.

compared, and numerical results (Fig. 6.4, 6.5) confirm the good quality of the equivalent simplified model since the error was below 5% in most of the zone of interest, despite the drastic reduction (20 times) of the number of elements.

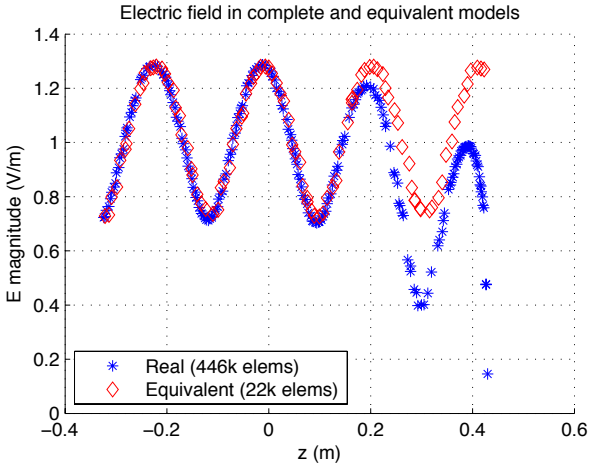

Figure 6.4: Electric field comparison between full and equivalent model.

Simulations were performed on Mac OS X 10.9.2 running on an Intel Core i7 3615QM with 16GB of RAM. Clang/LLVM 3.4 compiler and MKL PARDISO solver were used. The full model mesh included about 446000 tetrahedrons, which gave rise to a problem of 485572 unknowns. Assembly took $8.34s$, while the solver took $55.22s$. The simplified model consisted of about 22000 tetrahedrons, which gave rise to a problem of 26624 unknowns: assembly time was $0.45s$ while the solver took $0.48s$.

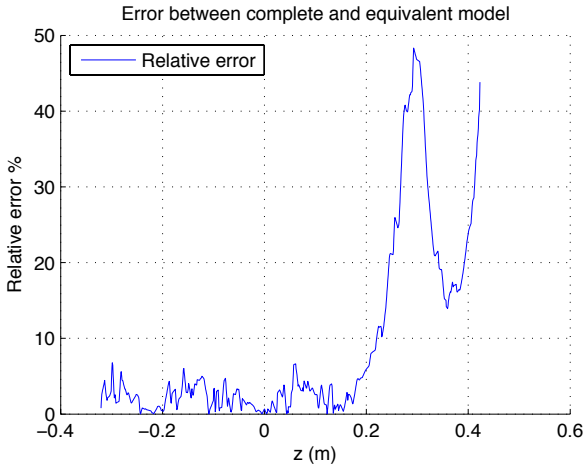

Figure 6.5: Percent relative error made by the equivalent model compared with the full one.

6.2 Modeling of equivalent antennas

In the experiments we made, two antennas were involved. The transmitting antenna was a dipole, while the receiving antenna was a biconical in the first experiment and a dipole in the second. Receiving antenna was not considered in the anechoic chamber model: electromagnetic field was computed in each point and then evaluated at the point corresponding to the antenna center. Transmitting antenna, on the other hand, was modeled as a sphere using the technique described in Section 4.2. The field radiated by the dipole was computed analytically using (4.29) and (4.30). The calculation required the knowledge of the antenna current I_0, which was measured as explained in the section about the actual experimental setups.

6.3 Full anechoic chamber modeling and simulation

Before building the models of the whole anechoic chambers, we had to deal with some practical problems. In particular, since measurements had to be done without interfering with the already scheduled activities of the laboratory, some planning was required to identify which instruments were needed, when they were available and for how much time. Moreover, available computing resources had to be taken into account since they limited the maximum frequency at which the experiments could be done. This brief planning phase led us to decide to make two experiments, one in a chamber used for CE compliance testing and the other in a chamber used for automotive testing. The aim of the first experiment was to measure the field magnitude at specified points inside the chamber, while the aim of the second experiment was to evaluate the magnitude of a standing wave forming under a table inside a chamber. It was also decided to use a dipole as transmitting antenna, to simplify and speed up the modeling phase. The dipole was built for the purpose and consisted in two copper rods of 57 cm connected directly to the feeding coaxial cable. A ferrite was then placed near the feedpoint as balun. For the

first experiment, it was decided that the measurements had to be done between 90 and 390 MHz at steps of 10 MHz in horizontal and vertical polarization, while for the second experiment between 200 and 250 MHz. The frequency ranges we chose allowed to use a single mesh for all the simulations in the frequency range. The first mesh consisted in a box with a sphere inside, representing the transmitter at the prescribed position. The second mesh was also a box with a sphere inside, but in addition it contained the table were devices under test are usually placed. Meshes were generated using Netgen software. After creating the meshes, the computation of equivalent impedance (Fig. 6.6) was done according to the procedure described in the previous section, which is detailed in the following steps

- simulation of the unit cell
- impedance calculation and translation
- simulation of the equivalent unit cell
- comparison of the fields calculated with the two models
- if the relative error is below 5%, the calculated impedance is accepted as valid

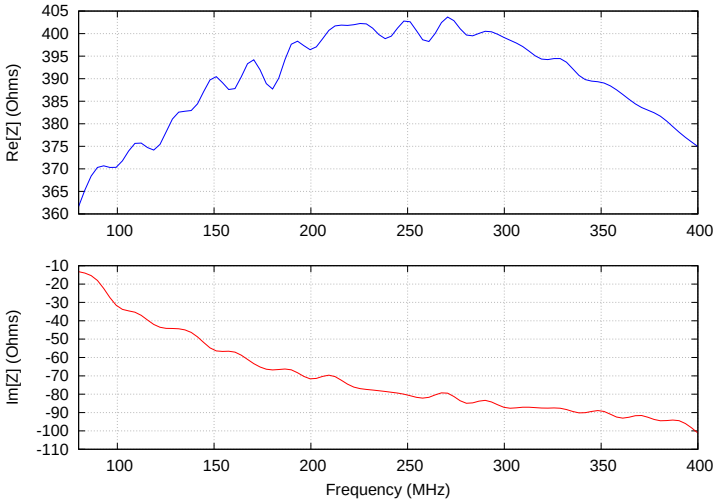

Figure 6.6: Equivalent wall impedance computed with the technique described. The values were then used as impedance boundary condition in the full chamber simulations. These impedance values give a return loss better than 25 dB in the whole measurement range.

The material parameters of cones and ferrites which were used in the unit cell models were obtained by private communication with the vendor. Data was provided as a table containing the values of ε', ε'', μ' and μ'' at steps of 4 MHz. Linear interpolation was used to recover the intermediate values.

6.4 Comparison of the models with experimental data

One of the goals of the developed code is to allow the validation of real-world measurements using numerical simulations. For this reason, two experiments were prepared and carried out in the anechoic chambers of the *Emilab* EMC laboratory in Amaro (Udine). In this section, experiments will be described in all their details and then the experimental data will be presented and discussed. The first experiment allowed for a large-scale comparison between measurements and simulation, while the second was rather limited because the anechoic chamber schedule didn't allow to do otherwise.

6.4.1 Experimental setup

The first experiment was conducted in a semi-anechoic room manufactured by ETS-Lindgren. Its dimensions in x (length), y (width) and z (height) are of 8.64m, 5.6m and 5.68m respectively. The experiment consisted in the measurement of the electric field produced by a RF radiator placed inside the room. The radiator consisted in a comb generator connected to the specifically designed dipole already mentioned. On the receiver side, a biconic antenna was attached to an EMI receiver (Fig. 6.7). Transmitting and receiving antennae were placed at a distance of three meters one from each other, at the heights of 1m, 1.5m and 2m in all possible combinations. Measurements were made from 90 to 390 MHz at steps of 10 MHz in both polarizations, for a total of 558 data points.

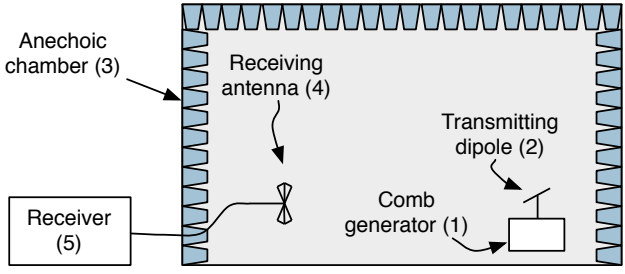

Figure 6.7: Setup used to measure the field radiated by the comb generator (1) attached to the test dipole (2) within the anechoic chamber (3) containing receiving antenna (4). Outside the chamber there is the EMI receiver (5).

The second experiment was conducted in another semi-anechoic room of dimensions $5.7m \times 4.9m \times 3.3m$, but intended for automotive compliance testing. This kind of room is characterized by the presence of a table of prescribed [CIS08b, ISO08] dimensions where the device under test is usually placed. The table is made of wood, with a copper sheet placed above the table. Moreover, the copper sheet is connected to the room floor by means of some copper strips. The transmitting dipole was placed at one meter from the table, in horizontal position and at an height of one meter (Fig. 6.8). Receiving antenna was also a dipole and was used to measure the field along the dot-dash line in (Fig. 6.8). In particular, field was sampled at 25, 50, 75, 100 and 125 cm from the grounding strips, at the points marked in red.

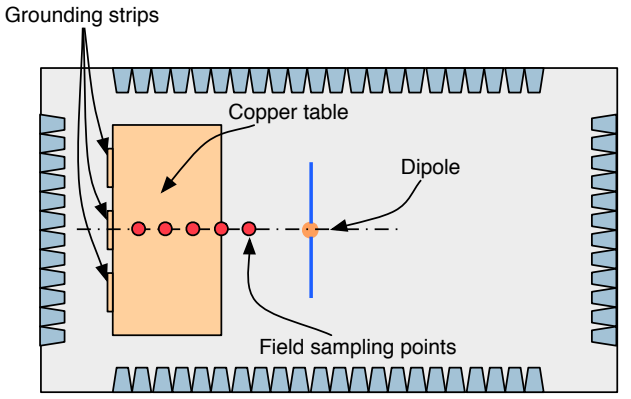

Figure 6.8: Setup used for the second experiment.

Several instruments were employed in both measurements, in particular:

- Comb generator
- Hewlett-Packard 8591EM spectrum analyzer
- Agilent 9038A EMI receiver
- Ad-hoc transmitting dipole
- Schwarzbeck UBAA9114 biconical antenna
- Hewlett-Packard 8753E vector network analyzer (VNA)

6.4.2 Measurement chain uncertainty calculation

To define a mathematical model of the measurement process, the entire measurement chain can be schematically illustrated as in Fig. 6.9.

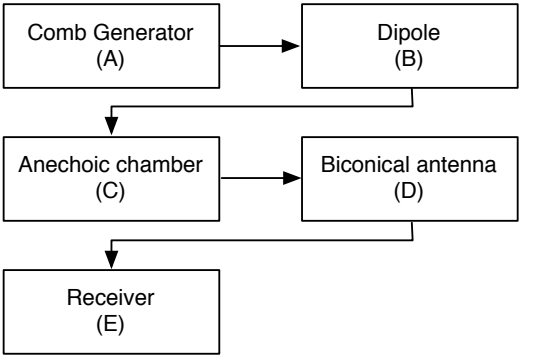

Figure 6.9: Schematic representation of the components involved in the measurement chain.

Table 6.1: Summary of the uncertainty contributes x_i in the measurements.

Symbol (x_i)	Meaning	Uncertainty	Probability distribution	Norm. factor	$u_i(x_i)$	c_i	$c_i u_i(x_i)$
R_i	Receiver reading	0.1	normal 1	1.00	0.10	1.00	0.10
L_{ar}	Receiver-antenna cable attenuation	0.2	normal 2	2.00	0.10	1.00	0.10
AF	UBAA9114 antenna factor	0.5	normal 2	2.00	0.25	1.00	0.25
	Receiver Corrections						
V_{sw}	Sine wave voltage	0.4	normal 2	2.00	0.20	1.00	0.20
L_{mar}	Antenna-receiver mismatch	0.1	U-shape	1.41	0.07	1.00	0.07
	Biconical antenna corrections						
AF_i	AF frequency interpolation	0.3	rectangular	1.73	0.17	1.00	0.17
AF_h	AF height deviation	1.5	rectangular	1.73	0.87	1.00	0.87
AF_{dir}	Directivity difference	0.5	rectangular	1.73	0.29	1.00	0.29
	Site corrections						
dSA	Site imperfections (max)	3.0	triangular	2.45	1.22	1.00	1.22
dH	Table height	0.1	rectangular	2.00	0.05	1.00	0.05
Rr	Repeatability	0.5	normal 1	1.00	0.50	1.00	0.50
	Transmitter corrections						
TXi	Comb level	0.5	rectangular	1.73	0.29	1.00	0.29
$dMta$	Mismatch: antenna-comb generator	0.24	U-shape	1.41	0.17	1.00	0.17
Gtx	TX antenna gain	2.0	rectangular	1.73	1.15	1.00	1.15
u_t	Total uncertainty ($\sqrt{\sum_i (c_i u(x_i))^2}$)						2.03
u_e	Expanded uncertainty (k=2) [dB]						4.05

From the already mentioned comb generator, marked as (A), the signal goes to the dipole (B), which radiates the electromagnetic field in the semi-anechoic chamber (C). The semi-anechoic chamber is an EMC site that mimics the *Open Area Test Site* (OATS in the following), whose primary characteristic is a metallic ground plane which behaves as a reflective surface. The mirror effect implies that on the receiving antenna the signal is the sum of a direct wave and a reflected wave which, in turn, produces different signal levels at different receiving antenna positions. Moreover, in a real anechoic chamber, there are multiple secondary signal paths due to the reflections on the walls and on the ceiling. These effects are considered as site imperfections and are taken into account in the *Normalized Site Attenuation*, a parameter measured using standard procedures [CIS08a]. Because of these effects, the field measurement at fixed positions, as we made in our experiments, is particularly challenging. At the chosen measurement points, the signal is received with a biconical antenna (D) and transferred to the receiver (E), which gives the experimental reading. Each block depicted in Fig. 6.9 contributes to the measurement uncertainty, in particular the measured amplitude of the electric field $|\boldsymbol{e}_m|$

$$|\boldsymbol{e}_m| = \sum_i x_i, \tag{6.3}$$

is given by the sum of the factors x_i expressed in logarithmic scale, which are reported in Table 6.1. While some of them have a quite intuitive meaning (reported in Table 6.1) others deserve special attention, in particular:

- Uncertainty on antenna factor AF: since the AF is measured on a discrete set of frequency, there is an error due to interpolation, denoted as AF_i. Moreover, the antenna factor changes with antenna height and antenna axis direction, these effects are denoted by AF_h and AF_{dir}.
- Site imperfections dSA: the site imperfections are accounted for by the *Normalized Site Attenuation* [CIS08a].

Moreover, some other important parameters were set to zero and thus omitted from Table 6.1, in particular:

- Noise floor V_{nf}: The uncertainty due to the noise floor was considered negligible since all the measurements had an adequate signal-to-noise ratio ($> 10dB$).
- Cross-polarization A_{cp} and unbalance A_{bal}: these two contributes are set to zero because of antenna specifications.

Once all the factors and their uncertainties are known, the total uncertainty u_t and the extended uncertainty $u_e = 2u_t$ are calculated as [Joi08]

$$u_t = \sqrt{\sum_i \left[c_i u(x_i)\right]^2}, \tag{6.4}$$

where c_i is the sensitivity coefficient of the i-th contribute x_i, while $u_i(x_i)$ is its uncertainty value. The sensitivity coefficient is calculated as [Joi08]

$$c_i = \frac{\partial |\boldsymbol{e}_m|}{\partial x_i}. \tag{6.5}$$

6.4.3 Dipole antenna characterization

During the experiments the dipole antenna was placed at different heights and in different positions, as already detailed before. At each position, the influence of the metallic floor of the anechoic room is different and results in slight changes of the antenna impedance. Characterization thus consisted in the measurement of its impedance for each position. That measurement was taken just after each repositioning of the antenna, in order to have exactly the same configuration seen by the generator.

6.4.4 Antenna current measurement

Antenna current had to be measured for each frequency and for each antenna position, to derive the value I_0 needed for the computation of the dipole field (4.29). After a number of failed attempts, it turned out that the most reliable way to measure the antenna current I_0 is by an indirect measurement, using the forward power P_i delivered by the generator, the reflection coefficient Γ and the impedance Z obtained during antenna characterization:

$$I_0 = \sqrt{\frac{P_i(1-\Gamma^2)}{Z}}. \tag{6.6}$$

The power delivered by the comb generator was measured using a spectrum analyzer before starting the experiments and was checked again at the end, to ensure that the battery discharge didn't change the power levels. In each experiment the difference was not measurable.

6.4.5 Experiment 1: CE room

In this subsection, experimental data for the first experiment will be presented. Data is divided in six measurement groups: the first three refer to the horizontal polarization, while the last three refer to the vertical polarization. For each group, the transmitting antenna position is kept fixed while the receiving antenna is moved in height. Power levels delivered by the comb generator are summarized in Fig. 6.10. Fig. 6.11 summarizes the dipole impedance measured in the different configurations.

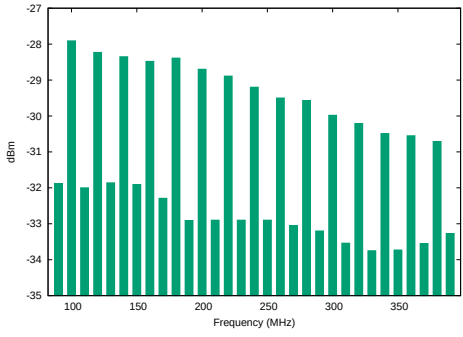

Figure 6.10: Comb generator spectrum measured at the beginning of the experiment.

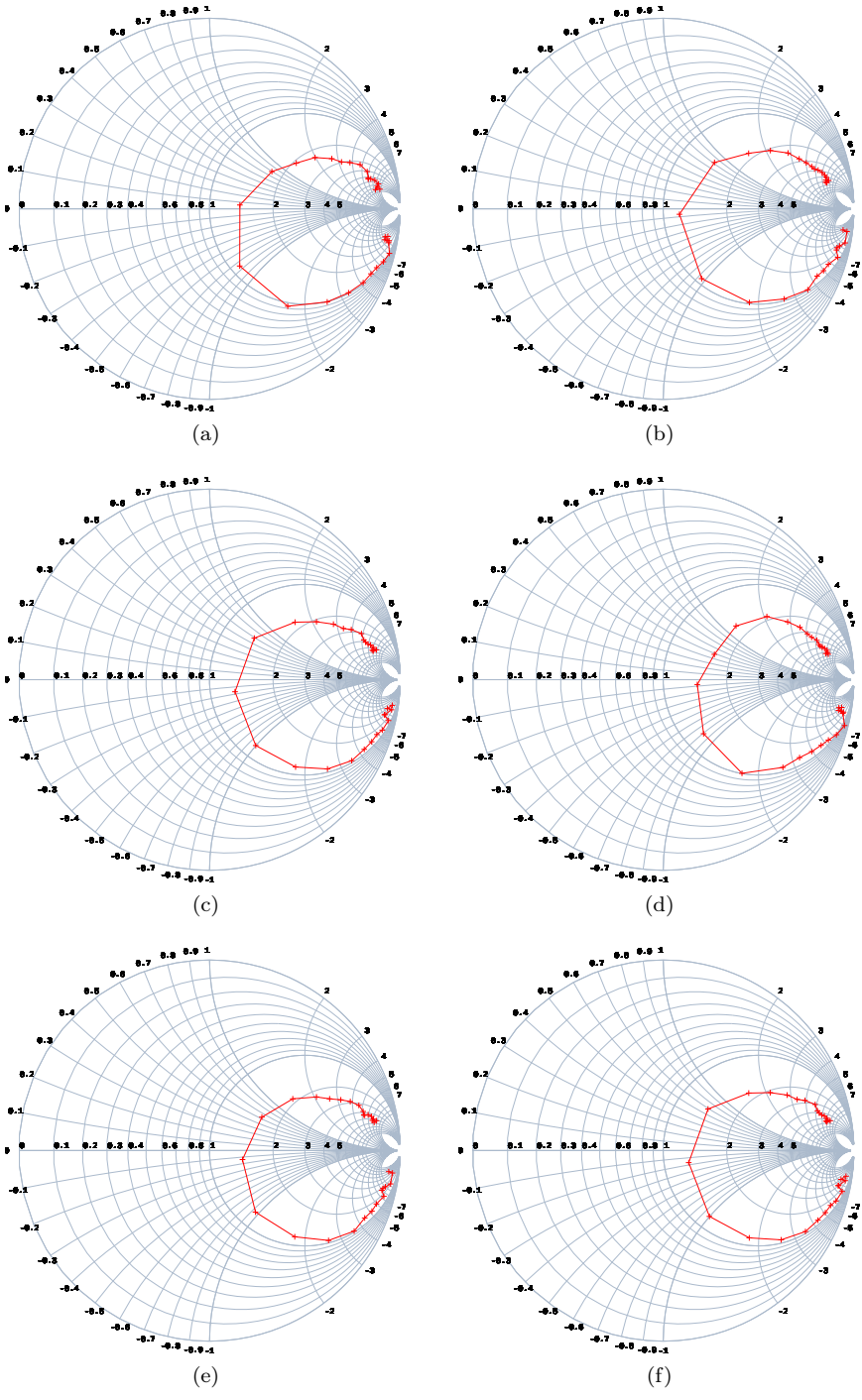

(a) (b) (c) (d) (e) (f)

Figure 6.11: Antenna impedance measured in the six configurations: 1m H, 1.5m H, 2m H, 1m V, 1.5m V and 2m V.

MG1: transmitter at h=1m, horizontal polarization

In this group of measurements, the transmitting antenna was placed at an height of 1 meter and the measurements were taken at an height of 1, 1.5 and 2 meters.

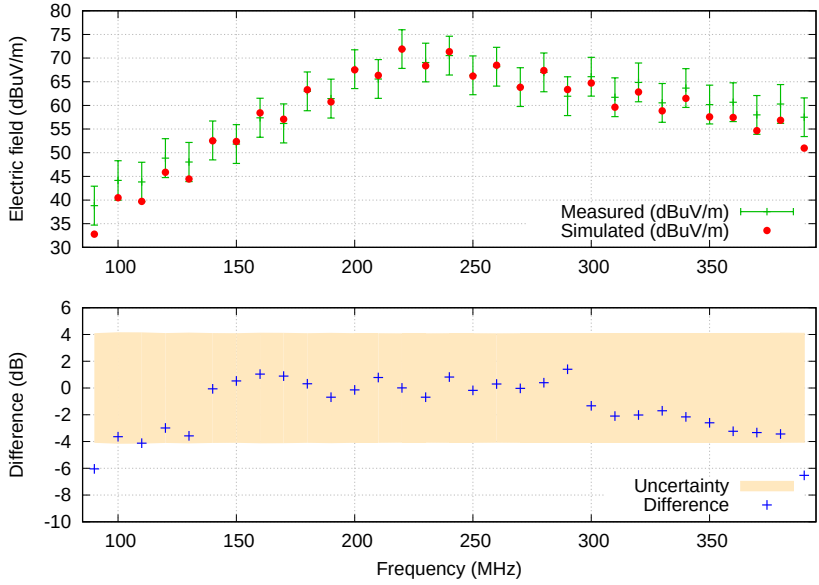

Figure 6.12: Transmitter at h=1m, receiver at h=1m, horizontal polarization.

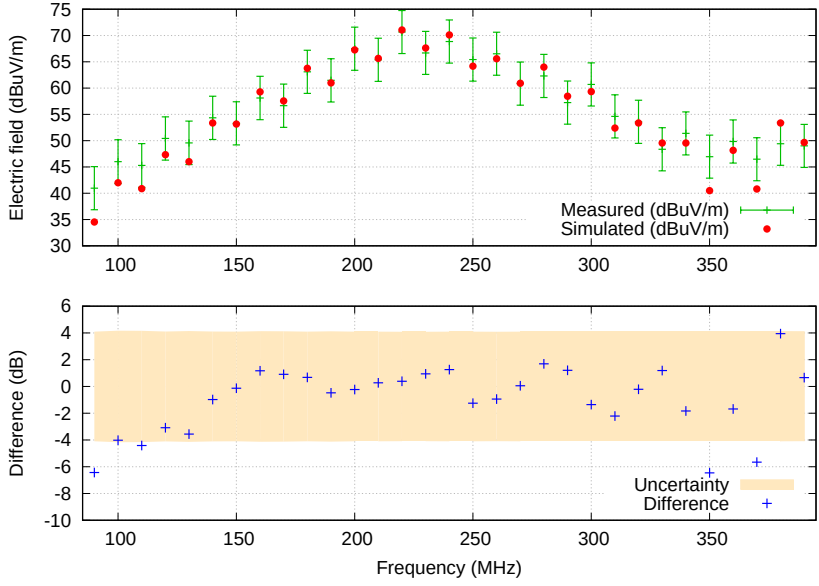

Figure 6.13: Transmitter at h=1m, receiver at h=1.5m, horizontal polarization.

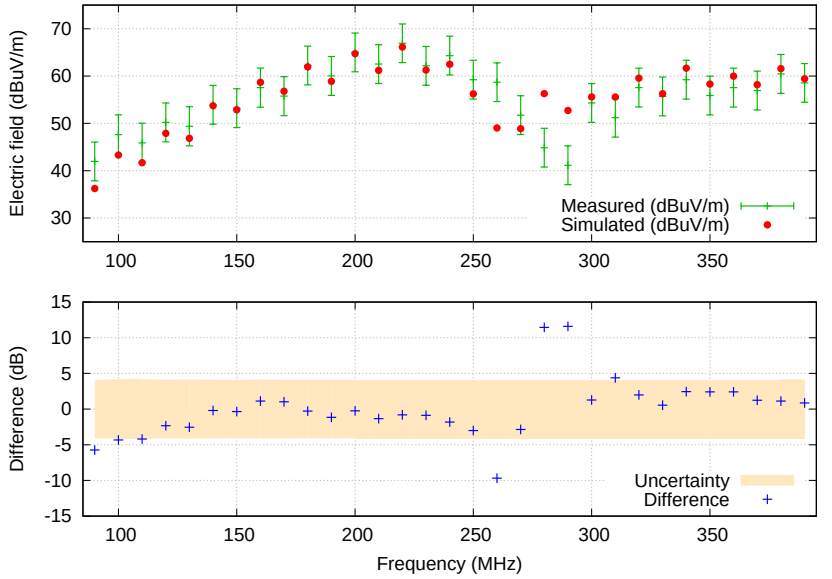

Figure 6.14: Transmitter at h=1m, receiver at h=2m, horizontal polarization.

MG2: transmitter at h=1.5m, horizontal polarization

In this group of measurements, the transmitting antenna was placed at an height of 1.5 meters and the measurements were taken at an height of 1, 1.5 and 2 meters.

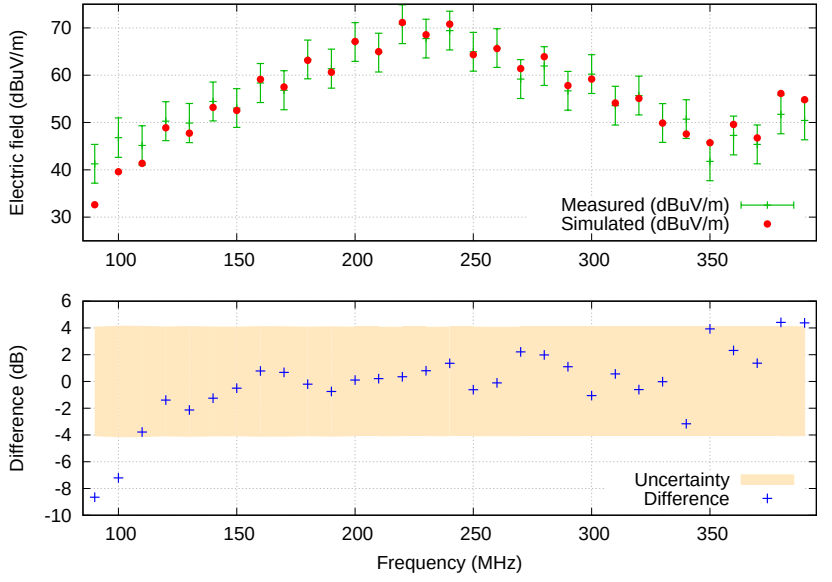

Figure 6.15: Transmitter at h=1.5m, receiver at h=1m, horizontal polarization.

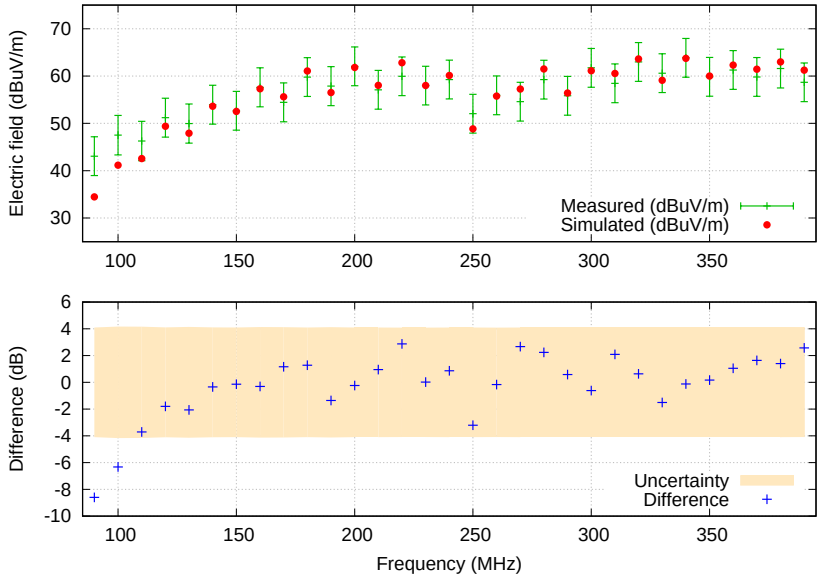

Figure 6.16: Transmitter at h=1.5m, receiver at h=1.5m, horizontal polarization.

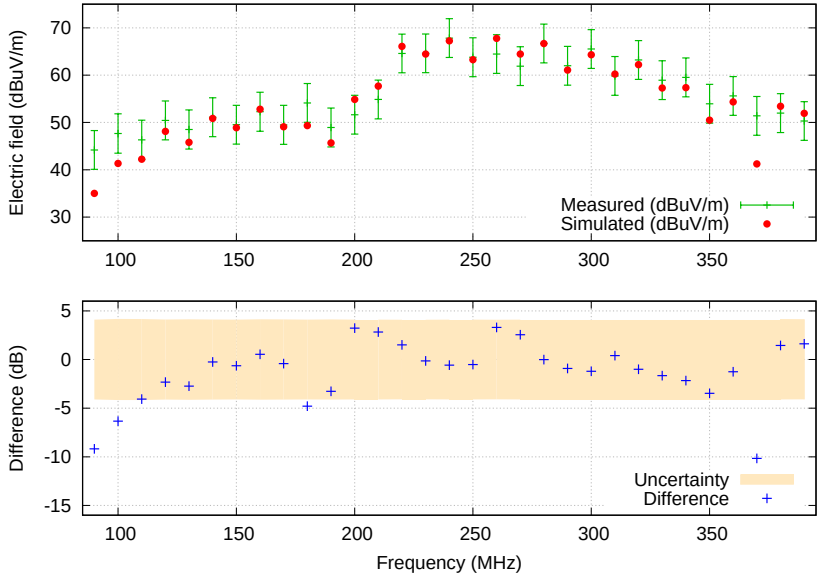

Figure 6.17: Transmitter at h=1.5m, receiver at h=2m, horizontal polarization.

MG3: transmitter at h=2m, horizontal polarization

In this group of measurements, the transmitting antenna was placed at an height of 2 meters and the measurements were taken at an height of 1, 1.5 and 2 meters.

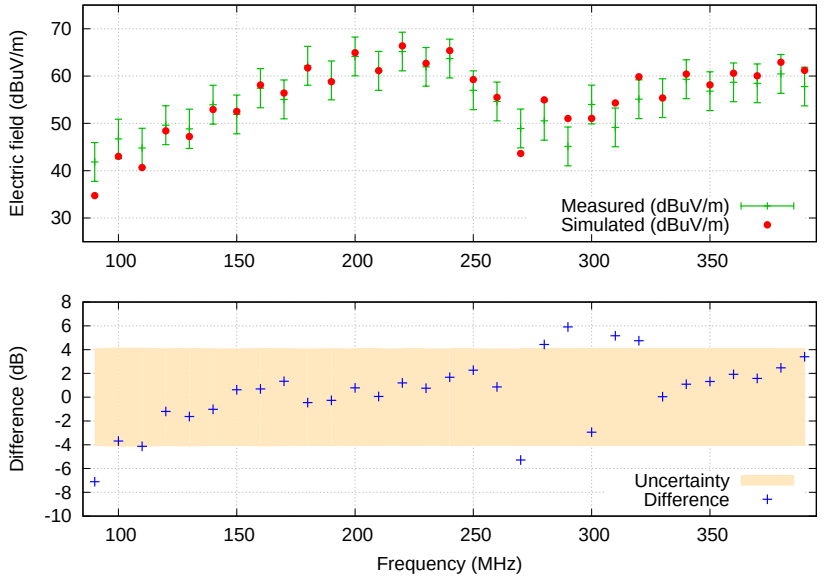

Figure 6.18: Transmitter at h=2m, receiver at h=1m, horizontal polarization.

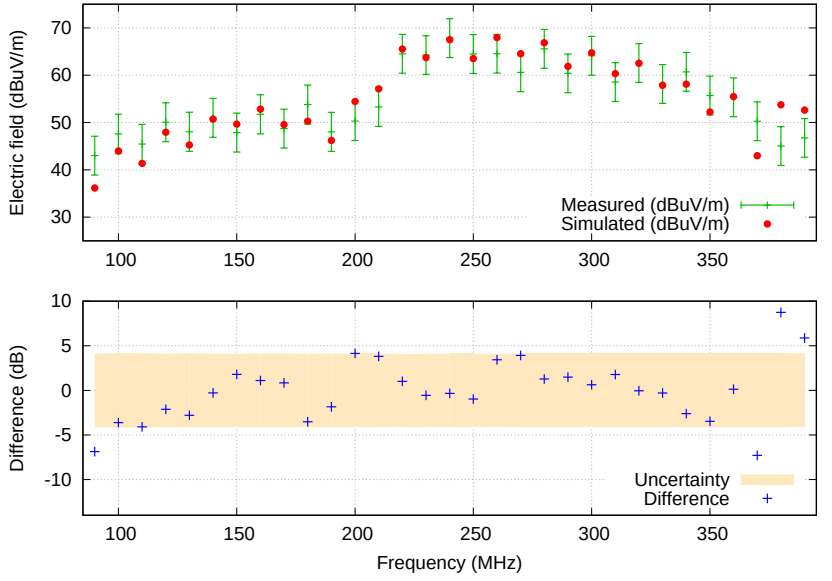

Figure 6.19: Transmitter at h=2m, receiver at h=1.5m, horizontal polarization.

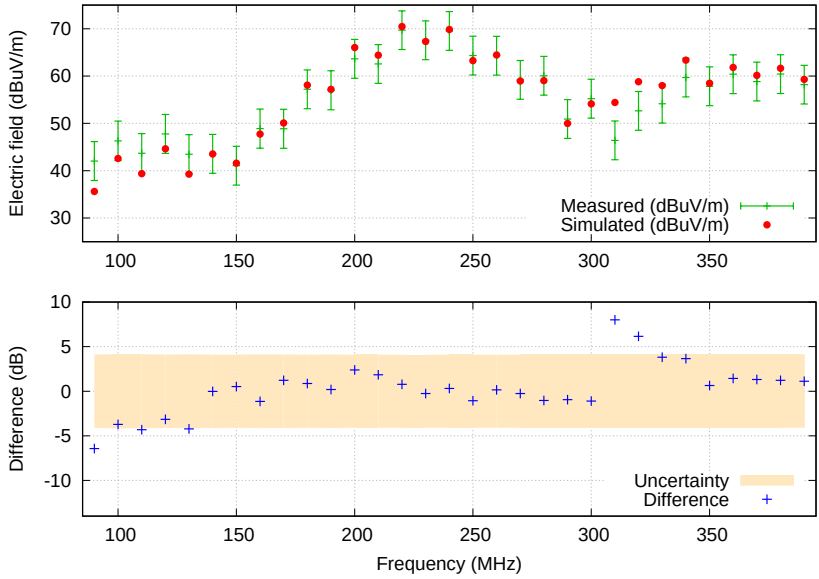

Figure 6.20: Transmitter at h=2m, receiver at h=2m, horizontal polarization.

Ground plane effect on dipole radiation pattern

It is well known [Bal05] that if a dipole is placed over a conductive plane in horizontal position, its radiation pattern is heavily distorted and the characteristic torus-shaped pattern becomes something more complex, with alternating zones of high field and low field. This effect is found both in the simulations and in the measurements, giving some confirmations about their correctness.

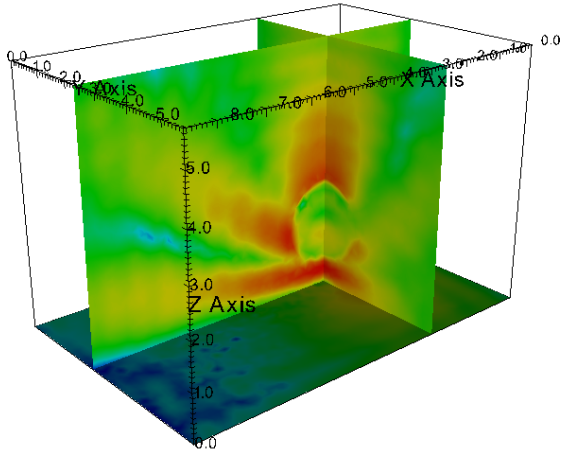

Figure 6.21: Sectional view of the electric field radiated by the equivalent dipole at $f = 230$ MHz, horizontal polarization. Distortion of the dipole radiation pattern due to the conductive floor is clearly visible.

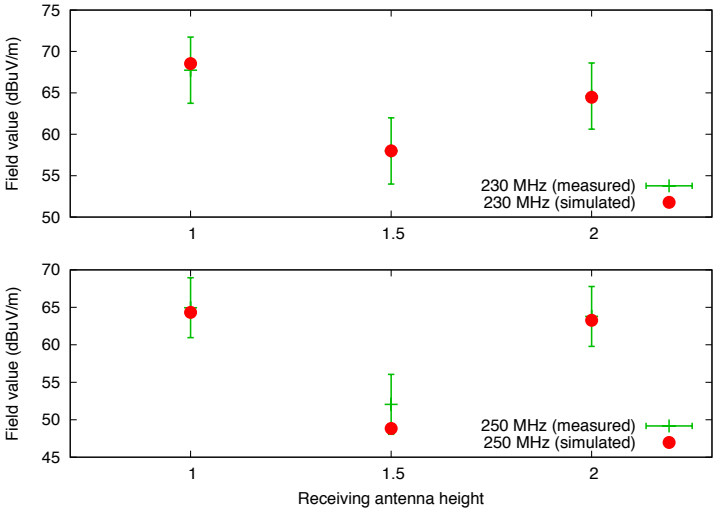

Figure 6.22: Simulated electric field and measured electric field are compared at different heights, $f = 230$ MHz and $f = 250$ MHz in horizontal polarization.

MG4: transmitter at h=1m, vertical polarization

In this group of measurements, the transmitting antenna was placed at an height of 1 meter and the measurements were taken at an height of 1, 1.5 and 2 meters.

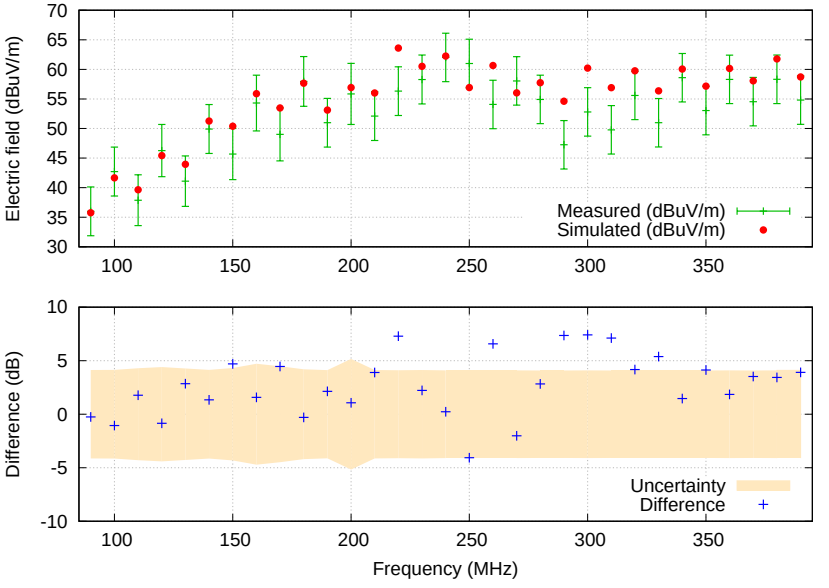

Figure 6.23: Transmitter at h=1m, receiver at h=1m, vertical polarization.

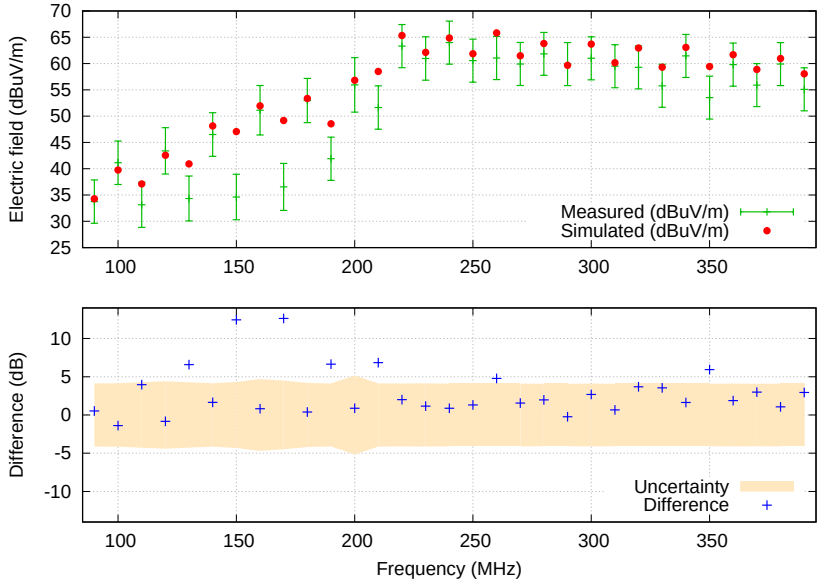

Figure 6.24: Transmitter at h=1m, receiver at h=1.5m, vertical polarization.

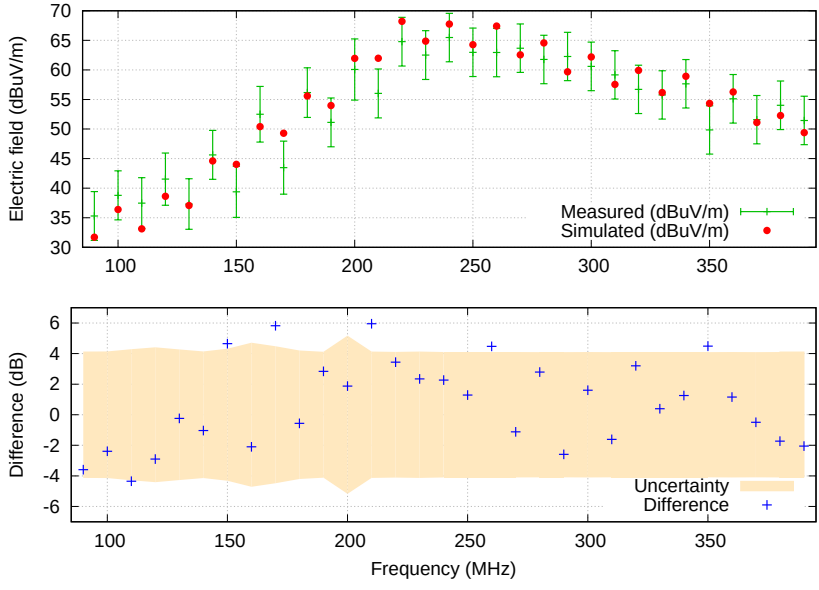

Figure 6.25: Transmitter at h=1m, receiver at h=2m, vertical polarization.

MG5: transmitter at h=1.5m, vertical polarization

In this group of measurements, the transmitting antenna was placed at an height of 1 meter and the measurements were taken at an height of 1, 1.5 and 2 meters.

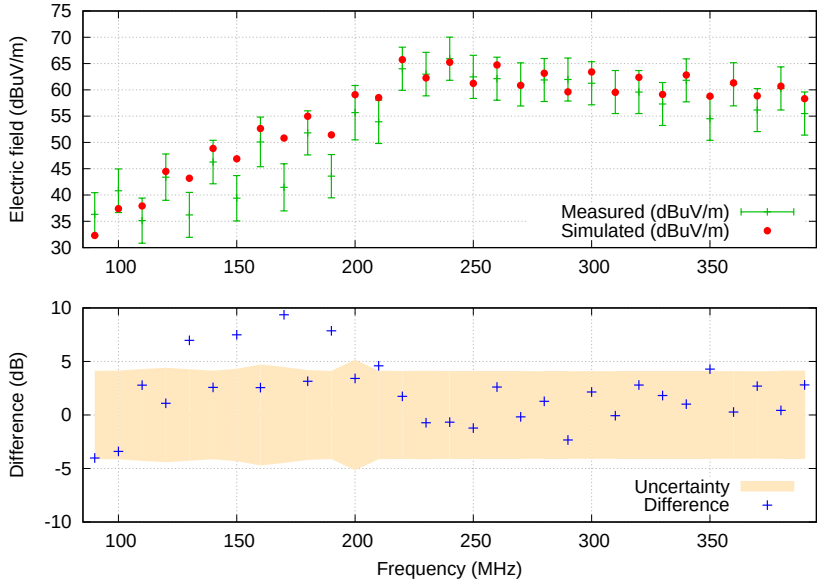

Figure 6.26: Transmitter at h=1.5m, receiver at h=1m, vertical polarization.

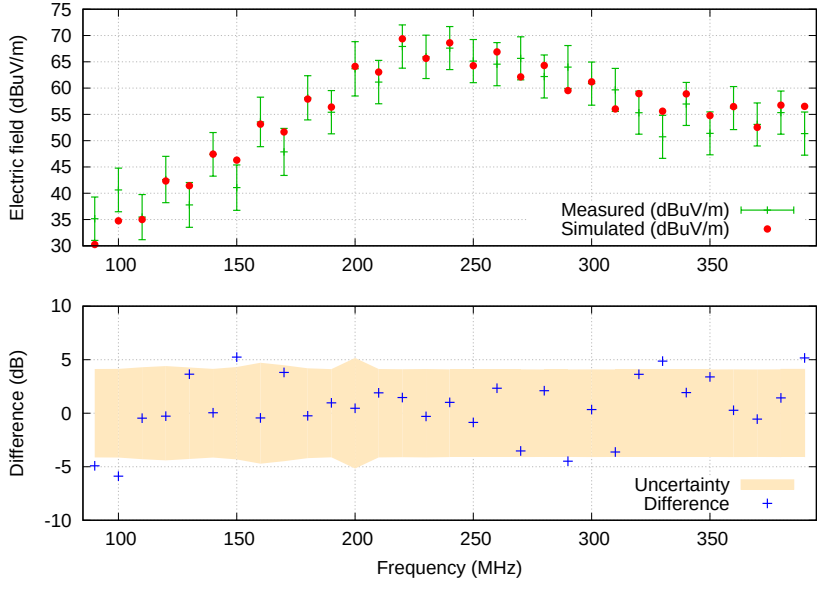

Figure 6.27: Transmitter at h=1.5m, receiver at h=1.5m, vertical polarization.

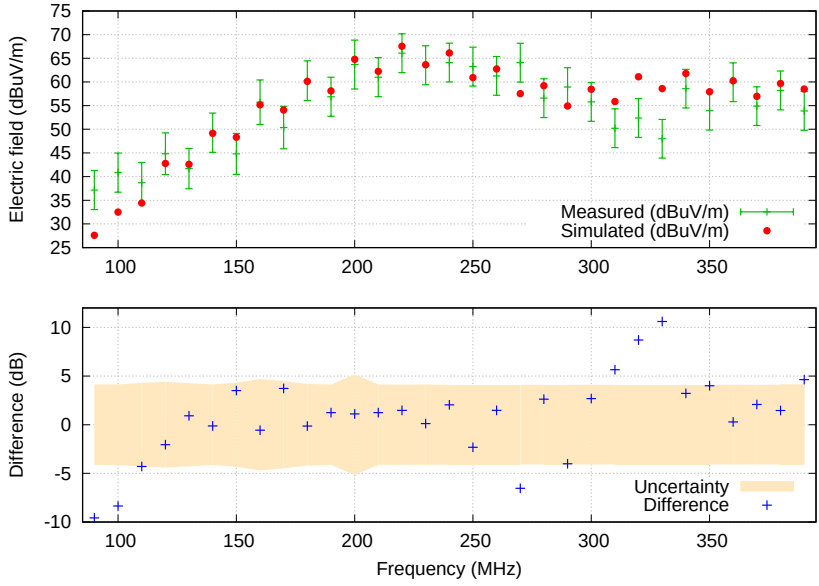

Figure 6.28: Transmitter at h=1.5m, receiver at h=2m, vertical polarization.

MG6: transmitter at h=2m, vertical polarization

In this group of measurements, the transmitting antenna was placed at an height of 2 meter and the measurements were taken at an height of 1, 1.5 and 2 meters.

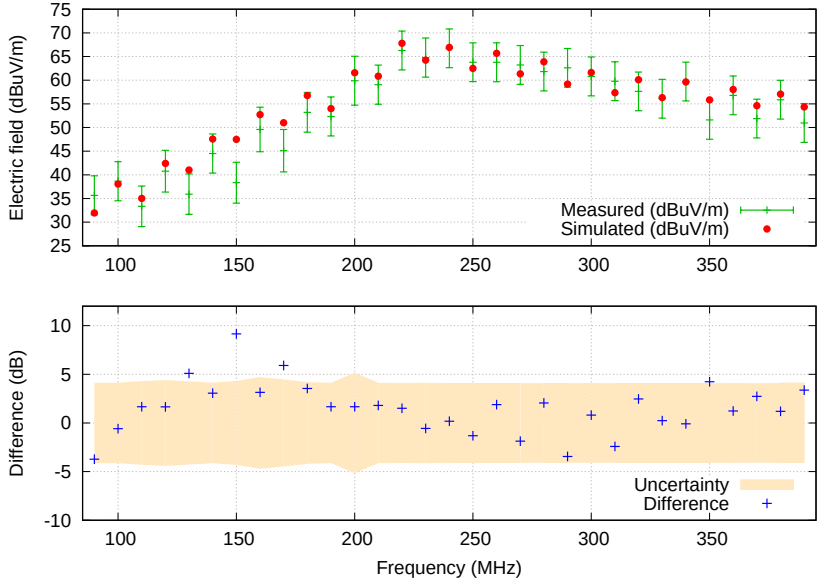

Figure 6.29: Transmitter at h=2m, receiver at h=1m, vertical polarization.

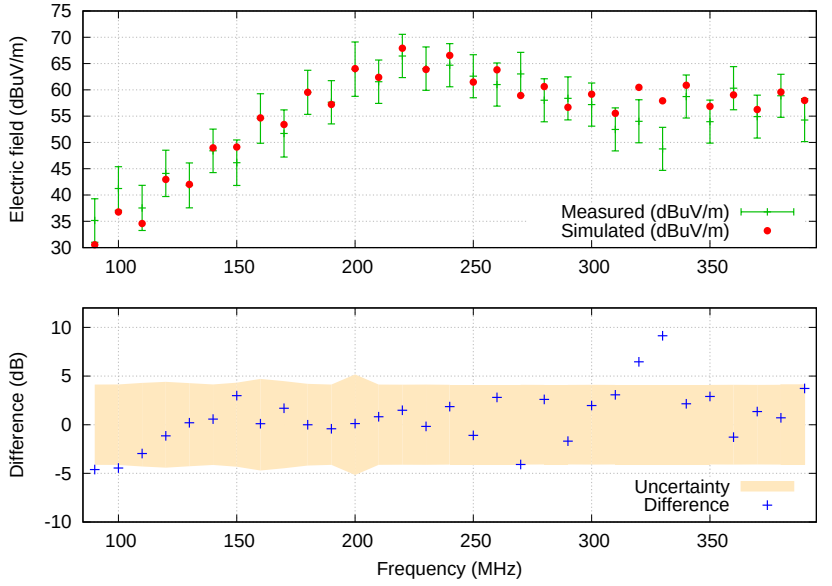

Figure 6.30: Transmitter at h=2m, receiver at h=1.5m, vertical polarization.

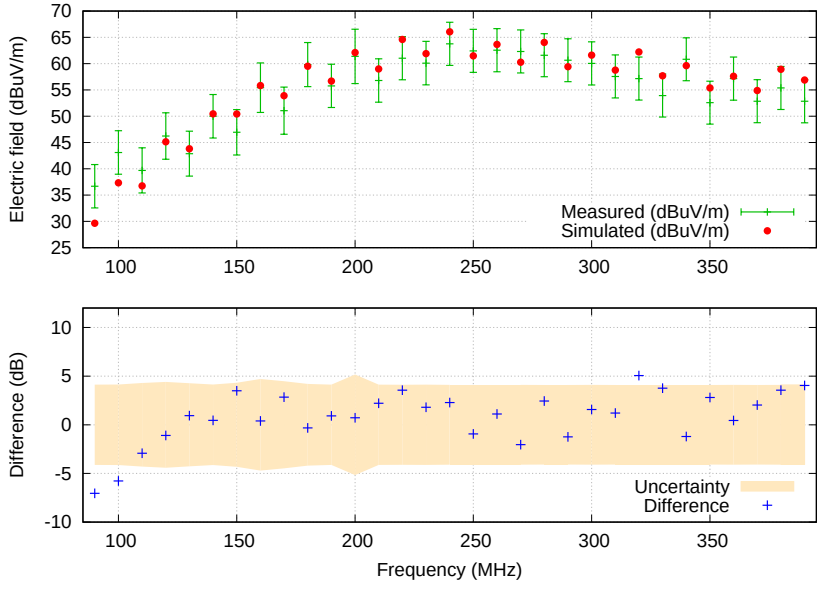

Figure 6.31: Transmitter at h=2m, receiver at h=2m, vertical polarization.

The experiment shown a good agreement between the simulations and the results, suggesting that the equivalent model idea could be a viable way to enable the simulation of large anechoic chambers. However, comparison is not satisfactory because it turns out that 1 measurement out of 5 don't agree with the simulation. We will return on this

issue in Section 6.5, after discussing the data of the second experiment.

6.4.6 Experiment 2: Automotive room

In this section, the data about the second experiment is presented. Figures show a comparison between measurements and simulation in the frequency range between 200 and 250 MHz, in steps of 10 MHz. This time on the x-axis there is a position and not a frequency, as in the previous experiment. The position is the distance between the receiving antenna and the grounding strips of the table (Fig. 6.8). In this second experiment we observe a quite good agreement between the simulations and the measurements. In particular, measurements confirmed the presence of a standing wave below the table, as predicted by the simulation. Also in this case, we find that the equivalent modeling is working as expected, providing reasonable results about the field configuration inside the anechoic chamber.

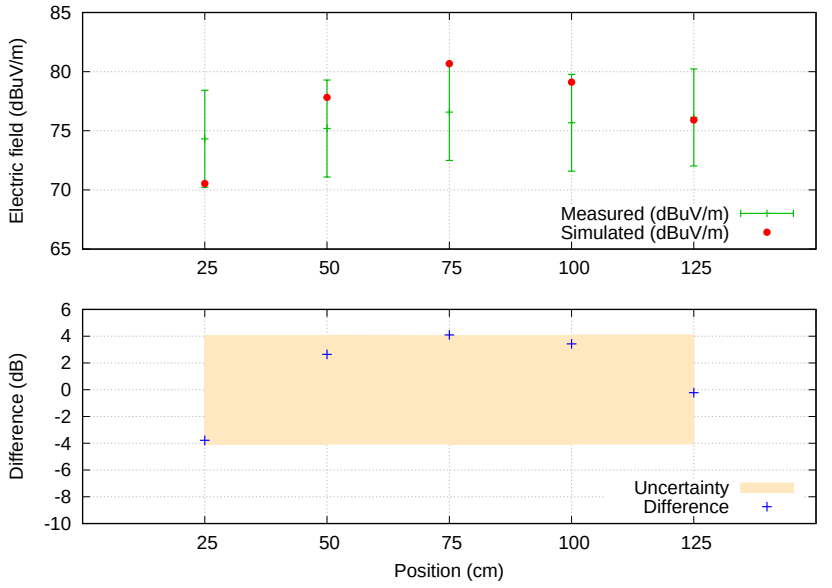

Figure 6.32: Measurements of the second experiment, taken at f=200MHz.

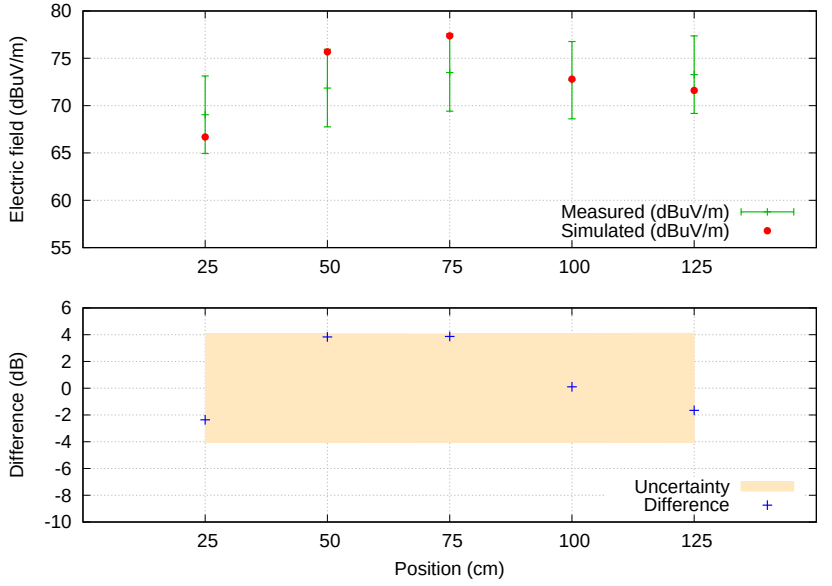

Figure 6.33: Measurements of the second experiment, taken at f=210MHz.

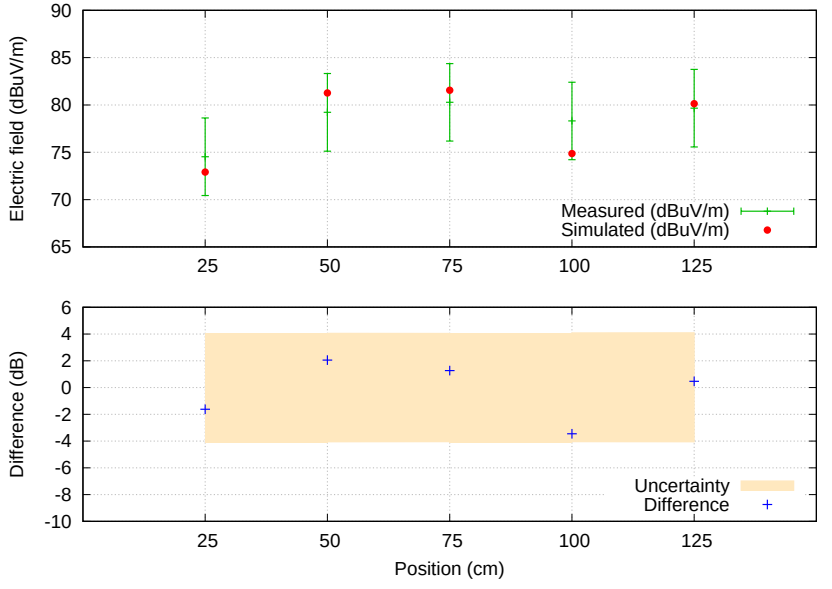

Figure 6.34: Measurements of the second experiment, taken at f=220MHz.

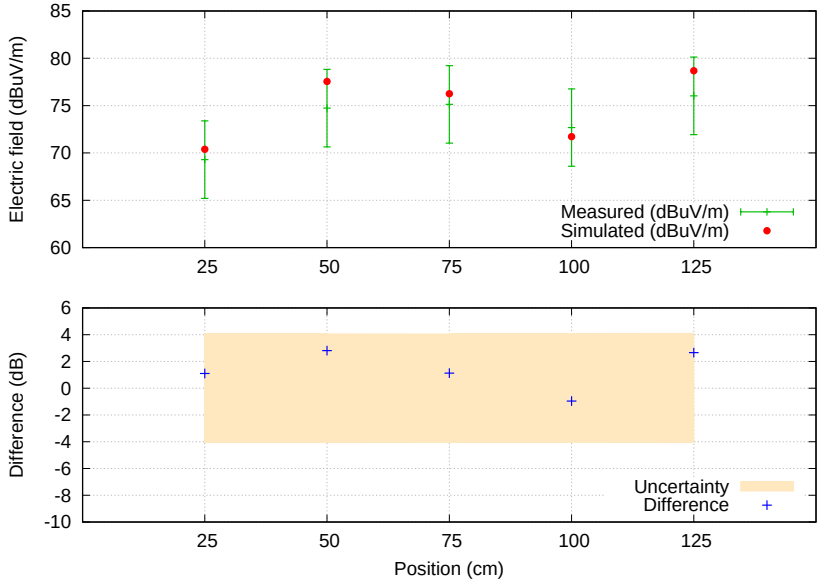

Figure 6.35: Measurements of the second experiment, taken at f=230MHz.

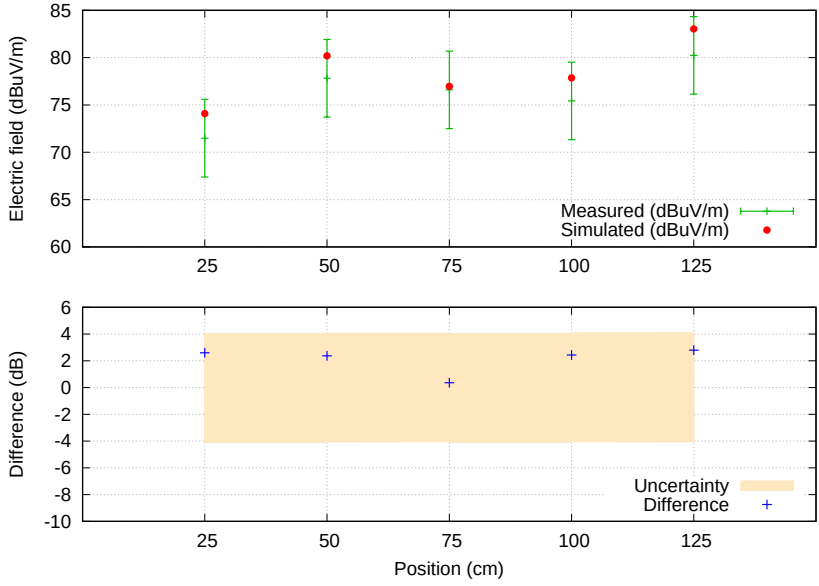

Figure 6.36: Measurements of the second experiment, taken at f=240MHz.

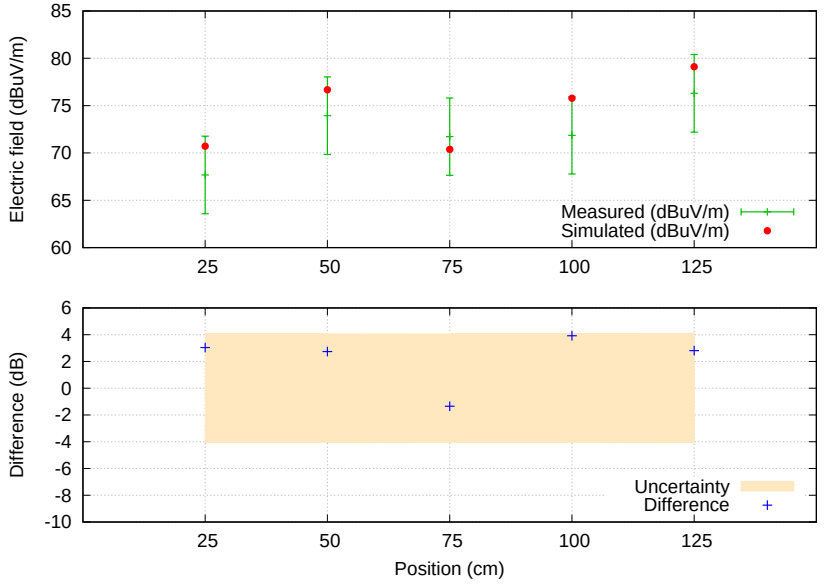

Figure 6.37: Measurements of the second experiment taken at f=250MHz.

6.5 On the discrepancies between simulations and measurements

Looking at the simulation data of the first experiment, there are results that fall outside the uncertainty band of the field measurement. In particular, 139 comparisons out of 558 (19.2%) don't agree on the field value. Sometimes the error is quite small, while sometimes is huge. Four main factors could explain the difference, in particular

- inaccuracy of the numerical simulation due to the huge simplifications involved,
- uncertainties in material parameters used in the equivalent wall model,
- uncertainties on simulation input (antenna current),
- errors in measurements.

We start our analysis by assuming that the models are accurate and that the material parameters are exact. We are thus expecting that the source of the simulation errors is either an incorrect model input or an incorrect measurement.

6.5.1 Uncertainty in model inputs

As explained before, antenna current is a measured quantity, used as a simulation input. As every measured quantity, this current has an associated uncertainty, which affects the result of the simulation. Our task now is to give an estimate of that uncertainty.

The electric field radiated by the dipole, calculated as in (4.29), can be rewritten in logarithmic form as

$$E_{\theta,dB} = 20\log(I_0) + 20\log(T), \tag{6.7}$$

where T accounts for all the multiplicative terms in (4.29). Moreover, as already detailed, the current I_0 is calculated as

$$I_0 = \sqrt{\frac{P_{fwd} - P_{rev}}{Z_{ant}}}, \tag{6.8}$$

where

$$Z_{ant} = Z_0 \frac{1+\Gamma}{1-\Gamma}, \tag{6.9}$$

with Γ denoting the reflection coefficient. Therefore, using (6.8) and (6.9) the antenna current can be written as

$$I_0 = \sqrt{\frac{P_i(1-\Gamma^2)(1-\Gamma)}{Z_0(1+\Gamma)}} = \sqrt{\frac{P_i}{Z_0}}(1-\Gamma), \tag{6.10}$$

and converting in logarithmic form

$$\begin{aligned} 20\log(I_0) &= 10\log(P_{fwd}) + 20\log(1-\Gamma) - 10\log(Z_0) \\ &= P_{fwd,dBm} - 30 + 20\log(1-\Gamma) - 10\log(Z_0). \end{aligned}$$

The sensitivity coefficients can now be calculated [CIS08a, Joi08] as

$$c_\Gamma = \frac{\partial(20\log I_0)}{\partial\Gamma} = -\frac{20}{1-\Gamma}\frac{1}{\ln(10)}, \tag{6.11}$$

$$c_p = \frac{\partial(20\log I_0)}{\partial P_{fwd,dBm}} = 1. \tag{6.12}$$

With these coefficients, the uncertainty of the radiated field can be computed as

$$u(E_{\theta,dB}) = u(I_{0,dB}) = \sqrt{c_p^2 u_p^2 + c_\Gamma^2 u_\Gamma^2}. \tag{6.13}$$

The calculated values for the sensitivity coefficients suggest a simple interpretation of the uncertainty on the radiated field. In particular, high uncertainty on electric field is expected if there is an high uncertainty on the input power or if the reflection coefficient is high. While the first contribute is intuitive, the second deserves some explanation. An high reflection coefficient means that the power delivered to the antenna feedpoint is very low and then (6.8), also the current at the antenna is very low. However, the lower the current, the higher is the accuracy needed in the power measurement, because forward power and reverse power values become very close. But, being the power measurement accuracy fixed, the uncertainty rises when Γ tends to 1. In our practical case, u_p and u_Γ have the values 0.5 and 0.01 respectively, and are derived

from the instrument specifications. Plugging all the data into the described formulae, the results in Figures (6.38), (6.39) and (6.40) are obtained. As shown, a great number of the discrepancies are explained by considering the uncertainty of the antenna input current. In particular, now only the 11.6% of comparisons disagree on the field value. However, other discrepancies remain to be explained.

6.5.2 Identifying measurement errors using simulation

Figures (6.38b), (6.38d) and (6.38f) among others show that something unexplained happened, since unacceptable discrepancies remained despite considering all the uncertainties. It was then decided to take a second round of measurements to check if it was possible to reproduce the phenomena. The exact setup of the first round was reproduced, but time constraints allowed to take measurements only in the configuration with the transmitting antenna at h=1m, vertical polarization. On this second round, measurements compared far better with the simulation (Figure 6.41). As in the first round, after placing the transmitting antenna in its final position inside the anechoic chamber, current at the feedpoint was measured and it was found matching the current measured at the previous round almost perfectly. Apart the new antenna current values, nothing was changed in the simulation. Measurements, on the other hand, yielded completely different results, indicating a flaw in the field measurement process of the previous round. Considering these new measurements,the disagreement with the simulation is now reduced to the 9.7% of the comparison points. This means that now only 1 comparison out of 10 does not agree, halving the initial failure rate.

6.6 Simulation as validation tool for the measurements

The 9.7% of mispredictions remains a quite large number, however it seems likely that the measurement of the field in the configuration with the transmitting antenna at h=1.5m, vertical polarization was affected by the same problems that affected the measurement in the configuration with the transmitting antenna at h=1m, vertical polarization. In any case, numerical simulation employing equivalents models proved to be a powerful tool to simulate electrically large anechoic chambers. Despite the huge simplifications our models proved to be quite accurate, giving meaningful results. This kind of tools can then be successfully used in predicting the outcome of specific measurements, helping to assess their correctness.

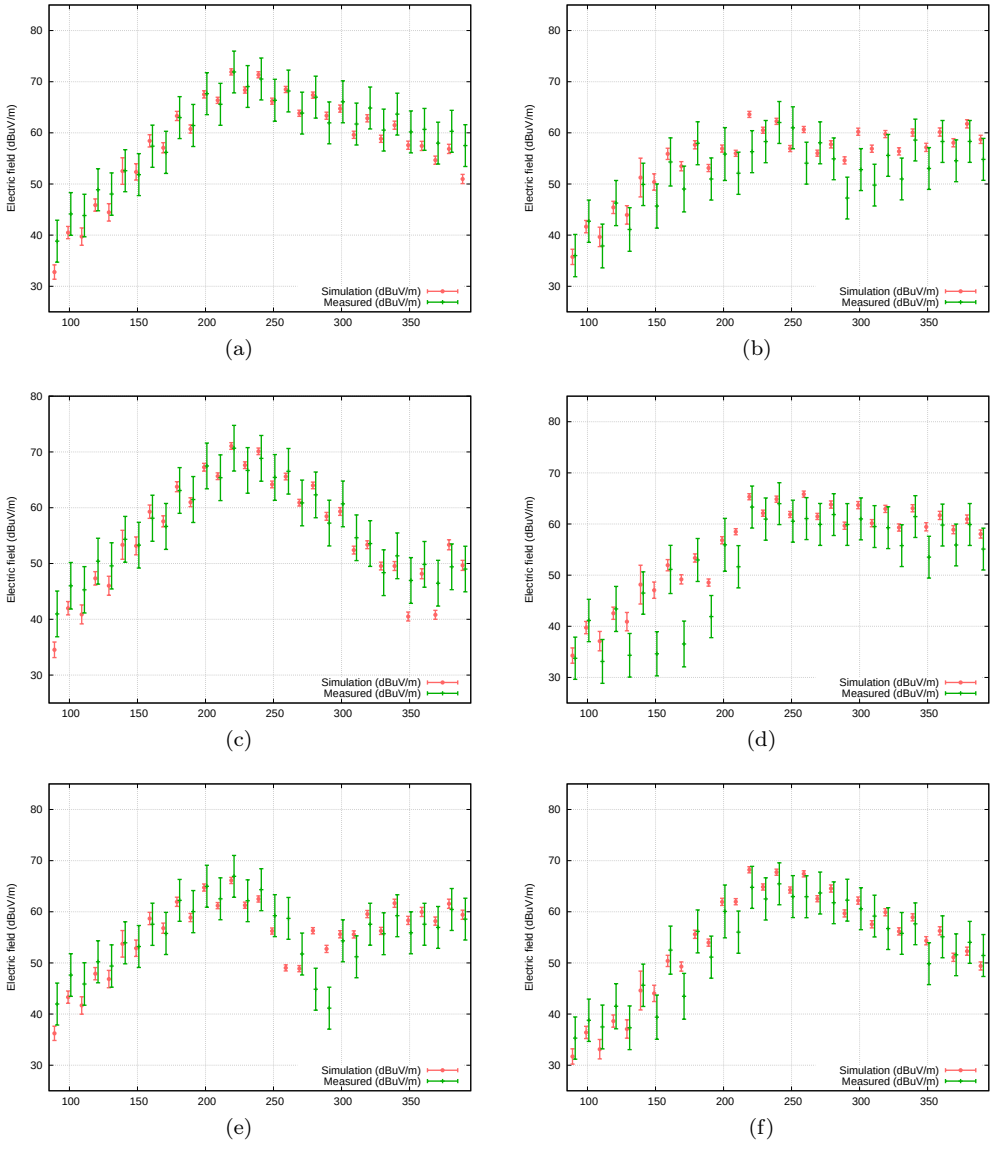

Figure 6.38: Simulations with associated uncertainty compared with measurements. The pictures show the data of the measurements taken with transmitting antenna at h=1m, horizontal polarization on the left and vertical polarization on the right. From top to bottom, receiver heights of 1m, 1.5m and 2m.

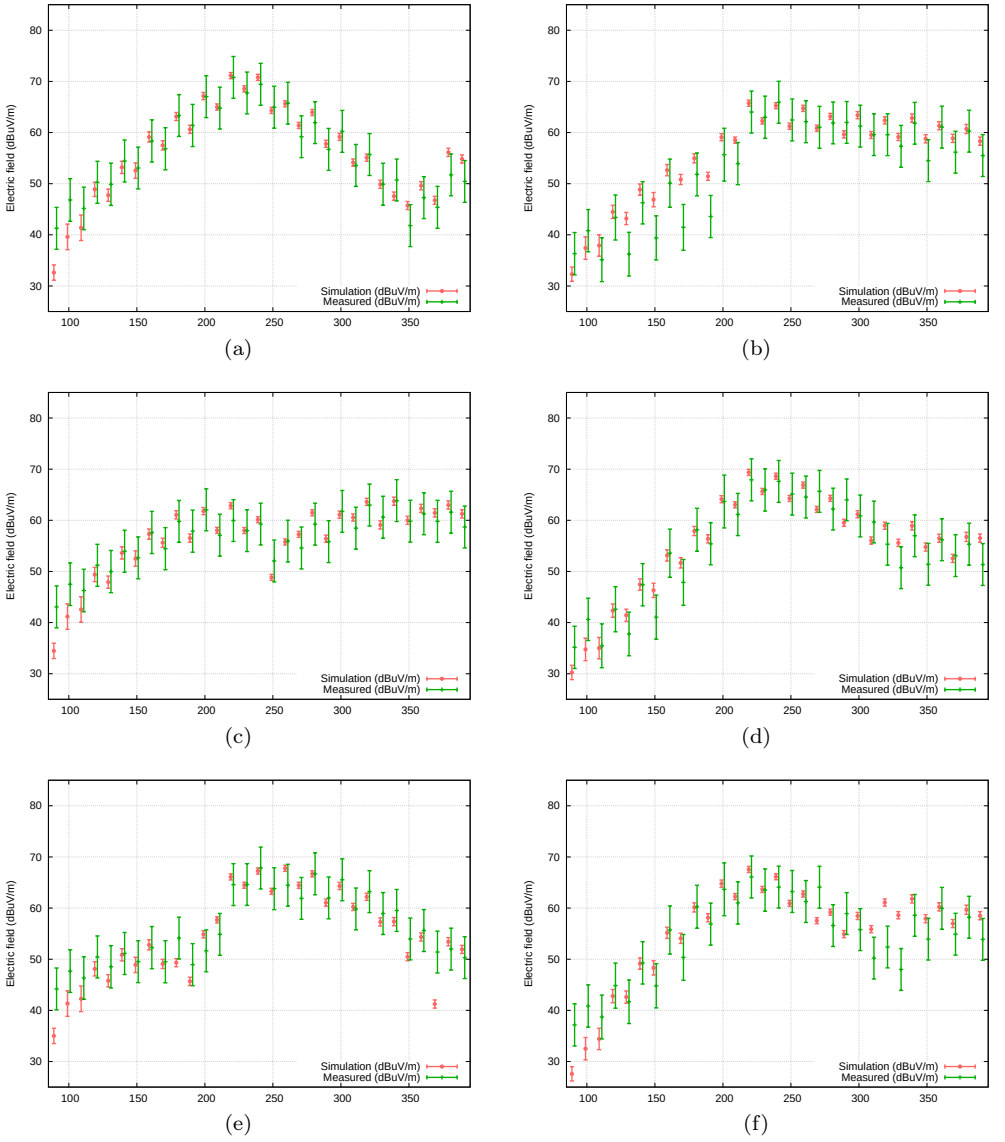

Figure 6.39: Simulations with associated uncertainty compared with measurements. The pictures show the data of the measurements taken with transmitting antenna at h=1.5m, horizontal polarization on the left and vertical polarization on the right. From top to bottom, receiver heights of 1m, 1.5m and 2m.

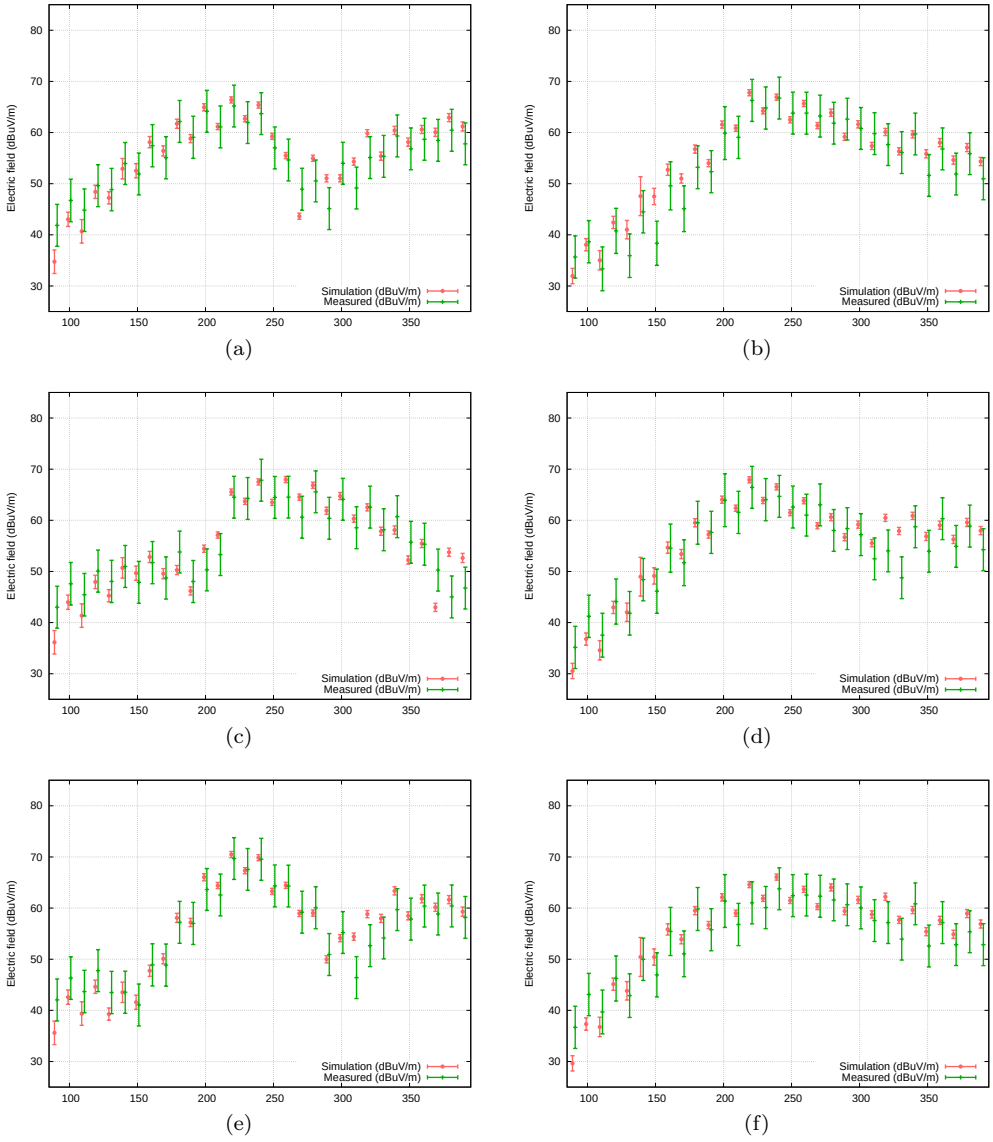

Figure 6.40: Simulations with associated uncertainty compared with measurements. The pictures show the data of the measurements taken with transmitting antenna at h=2m, horizontal polarization on the left and vertical polarization on the right. From top to bottom, receiver heights of 1m, 1.5m and 2m.

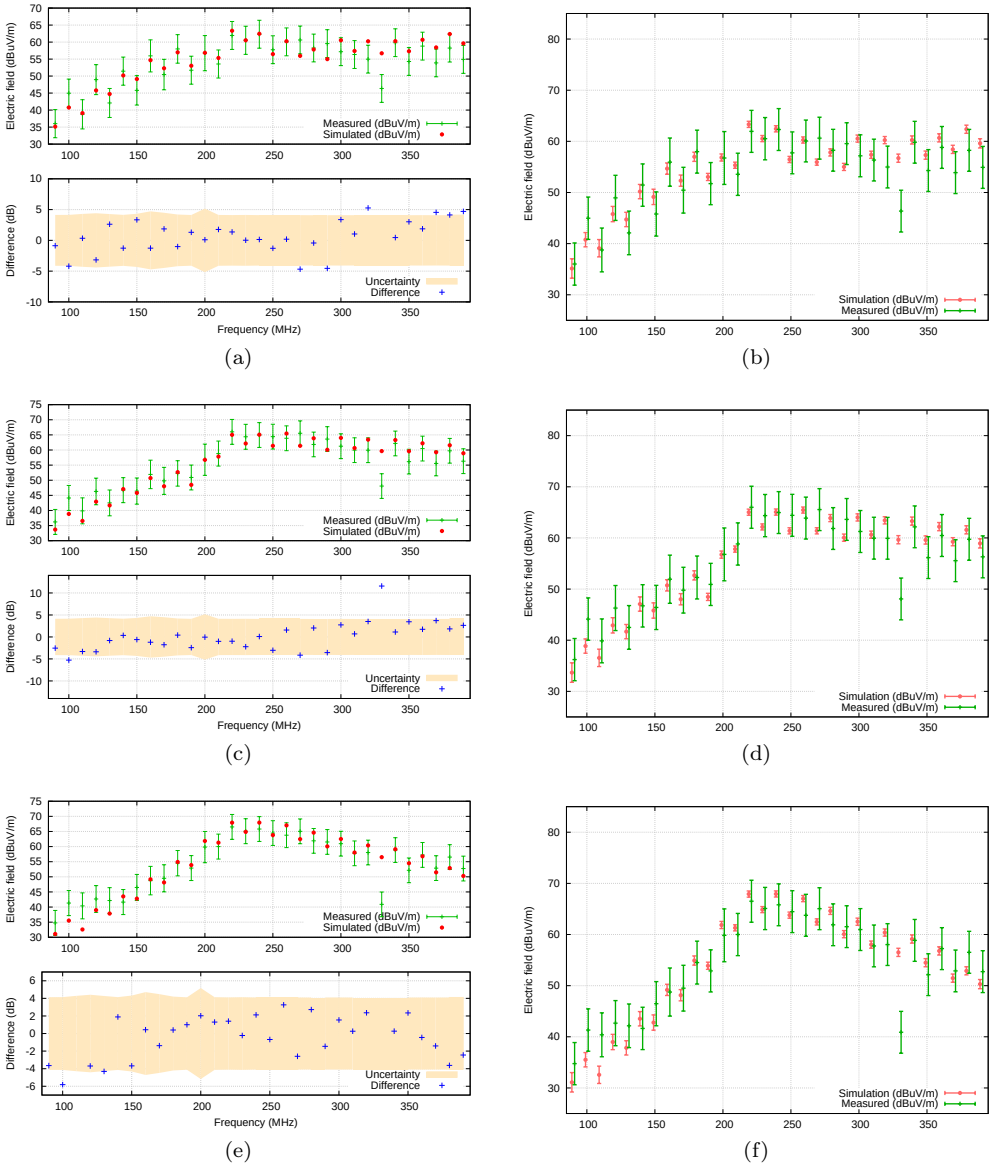

Figure 6.41: Second round of measurements at transmitter height = 1m, horizontal polarization on the left and vertical polarization on the right. From top to bottom, receiver heights of 1m, 1.5m and 2m.

7

The numerical code

All the research presented in this thesis was supported by a numerical code, named EMT, developed in the last three years. The code was developed out of the need of a platform to test the new numerical models, since existing codes either are based on FEM (Finite Element Method) or are closed-source, and thus unsuitable to our needs.

Development was driven by a number of objectives, dictated by common software engineering practices [Mar08]. Modularity was the first of them: the code is built around a number of modules interacting by means of simple and clearly defined interfaces. This allows to easily replace parts of the code if something needs to be changed, avoiding domino effects that could become problematic to manage. Modularity allows reusability, and a substantial part of EMT can be easily used as library in other codes. Extendability is another feature of the code: it should be simple to add new features, to add the ability to solve new problems or to add new numerical solvers, and EMT allows for this. Finally, performance was a main goal: the code must be fast and able to handle meshes with millions of elements easily, and thus great care was taken to design efficient algorithms and data structures, and to choose high performance libraries, like Armadillo [San10]. These objectives lead to only one possible choice for the implementation language, which is C++. Development started with C++11 but quickly moved to C++14 when the new standard was approved.

EMT is multi-platform, and builds exist for the three major operating systems, namely Mac OS X, Linux and Windows. It should compile easily also on FreeBSD and Solaris, however on these platforms some external libraries are not available, in particular Intel MKL. Moreover, the preferential operating system choice for running EMT is an UNIX-class operating system: Windows builds should work as expected, however not all features may be available.

Being a research code, EMT is more focused on giving a platform to experiment with DGA rather than on giving a fancy and usable user interface. The user has two ways to interact with the code: the first is a text-mode user interface, which allows to call the functions bound to it, while the second is to call EMT as a library. The commands for the text mode interface can be saved on text files, which constitute the *scripts*. Scripts drive the software in the various steps of simulation, from the loading of the mesh and

the parameters to the postprocessing.

This chapter is devoted to the description of the code. In a first part the general architecture is described, then a more programmer-oriented overview is given by describing step-by-step the implementation of a module.

7.1 Overview of the code

EMT is divided in several functional blocks, as depicted in Fig. 7.1. At the moment, the whole software consists in about 21000 lines of code. Despite being a quite small software, it would be impossible to describe it in full detail, so we will focus on a central component of EMT, the *module*.

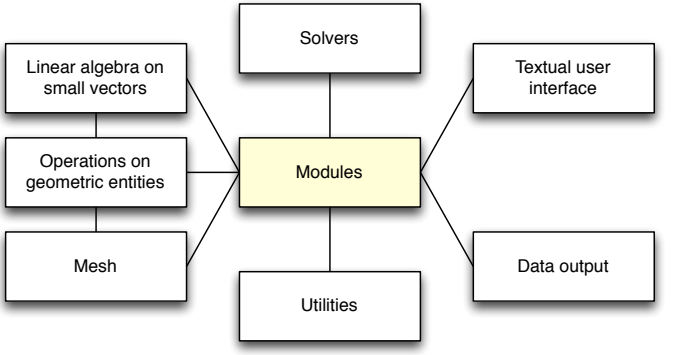

Figure 7.1: Functional blocks of the code.

Modules in EMT are the actual implementation of the physical problems we want to solve, and they make use of almost the full API provided by EMT. The most important ones are

- `fdprop`: Frequency domain wave propagation, implementing E- and H- field formulations
- `fdprop-av`: Frequency domain wave propagation, $\boldsymbol{a}$-V formulation
- `conduction`: Stationary conduction
- `electrostatics`: Electrostatics
- `geometry`: Operations related to meshes, like loading and unloading
- `test`: Module implementing sanity tests on data structures

The numerical solution of every problem involves more or less always the same steps, which can be summarized in reading geometry, reading boundary conditions, reading material parameters, assembling problem, solving it and postprocessing data. Modules implement all these steps and for this reason are a good starting point to understand the whole code.

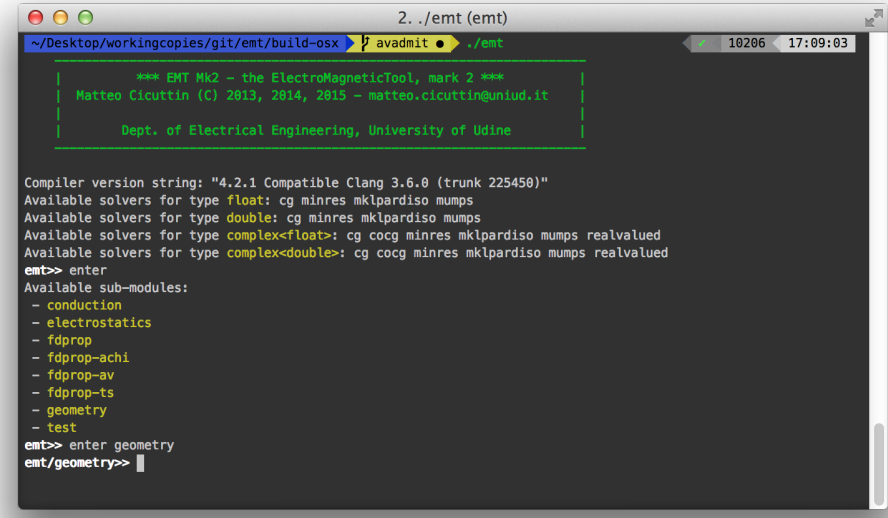

Figure 7.2: The code running. After startup a command prompt is presented, where the commands to setup the simulation can be given.

For simplicity on this chapter we will focus on the `conduction` module, because it is small, easy to understand and it uses a great number of the facilities available in the code, so it is quite useful in understanding the inner workings of EMT. The stationary conduction problem is derived from the following equations:

$$\nabla \cdot \boldsymbol{J} = 0, \tag{7.1}$$

$$\boldsymbol{E} = -\nabla V, \tag{7.2}$$

$$\boldsymbol{J} = \boldsymbol{\sigma}\boldsymbol{E}. \tag{7.3}$$

Combining them, we obtain the equation

$$-\nabla \cdot \boldsymbol{\sigma} \nabla V = 0, \tag{7.4}$$

which is the problem we are going to solve. Translating it in the discrete domain, we obtain (remember that $\tilde{\mathbf{D}} = -\mathbf{G}^T$)

$$\tilde{\mathbf{D}}\mathbf{M}_\sigma\mathbf{G}\mathbf{U} = \mathbf{0}. \tag{7.5}$$

The only boundary condition we will consider is the Dirichlet boundary condition, which is used to impose a potential on a specific domain boundary.

7.1.1 EMT scripts

We start our discussion by looking at a script:

```
enter geometry
    loadmesh scalefactor 1
    loadmesh netgen cube.mesh cube
exit

enter conduction
    setenv mesh cube
    setenv solver cg
    setenv domain1.material.sigma 100
    run
exit

exit
```

Listing 1: An EMT script.

The first command is `enter geometry`, which tells the command interpreter to switch to the context of the `geometry` module. Once there, some commands to handle the meshes are available. At the moment EMT supports only meshes generated by Netgen, and a mesh can be loaded by the user via command line using the `loadmesh` command. The command has the following syntax:

- `loadmesh <meshtype> <meshfile> <meshname>`: Load into memory a mesh of type `<meshtype>` from file `<meshfile>` and give it the name `<meshname>`. The only supported mesh type at the moment is `netgen`.
- `loadmesh scalefactor <scale>`: Specify the mesh units. If not specified, mesh is considered to be in meters. The `<scale>` parameter could be a numeric scale factor or one of the specifiers `mm`, `cm`, `dm`, `ft`, `in`.

After the command `loadmesh` is issued, the mesh is immediately loaded and placed in the *mesh store*, which is a kind of container for the meshes. This allows to have multiple meshes in memory at the same time and to use them in different modules. The geometry module context is then exited with the `exit` command and the `conduction` module is entered. There we encounter the `setenv` command, which is used to set a variable to a specific value. Its syntax is

- `setenv <variable> <value>`: The variable named `<variable>` is set to the value `<value>`.

Variables are organized in a hierarchical manner, entirely similar to the structure of a filesystem. Looking at Figure 7.3, we see that the variables we are setting are *local* to the conduction module and, in fact, their fully qualified names are `conduction.solver`, `conduction.mesh` and `conduction.domain1.material.sigma`. If, for example, we issue the command `setenv mesh cube` in the `fdprop` module, we are setting the variable `fdprop.mesh`, which is different.

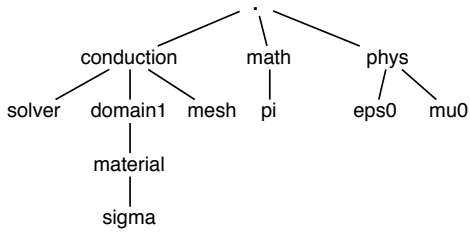

Figure 7.3: Hierarchical structure of the variables.

The three `setenv` commands we see in the text have the effect to make the conduction module use the mesh named "cube", to ask to use the conjugate gradient solver and to set the conductivity of the only subdomain of the mesh to the value 100 S/m. Finally, the `run` command triggers the call of the `run()` method of the module, which will be described later. What is missing from the script is the settings relative to the boundary conditions. In this module, to ease the explanation, the boundary conditions settings are hardcoded in the source code.

7.1.2 Mesh representation and operations on meshes

Before going ahead with our discussion and walking through the code of the module, we must take a little detour and look at how meshes are stored and which operations are available on them.

The first thing needed in a simulation is the geometry of the problem. Geometry can be specified in a multitude of ways and, once specified, a mesh has to be obtained. EMT does not have the ability to create meshes, so it expects an already meshed computational domain in the form of a specific mesh file. The mesh is read by a format-specific mesh parser, whose task is to translate the input file in actions to build the internal data structures. Internal data structures are contained in specific objects which are instances of the `mesh` class template. At the moment EMT can handle only tetrahedral meshes, however support for other types of meshes is easily added by providing the specific `mesh` template instance and relative functions.

Tetrahedral meshes are composed by nodes, edges, triangular surfaces and, of course, tetrahedral volumes, and in the code are represented by their respective class templates. A `tetrahedral_mesh` is then defined as

```
template<typename CoordT, typename IdxT>
using tetrahedral_mesh = mesh<CoordT, IdxT,
                              node<CoordT, IdxT>,
                              edge<CoordT, IdxT>,
                              triangle<CoordT, IdxT>,
                              tetrahedron<CoordT, IdxT>
                             >;
```

Listing 2: `mesh` template instantiation for tetrahedral meshes.

The template parameters `CoordT` and `IdxT` specify the types used for the representation of coordinates and for the representation of indices respectively.

At the moment EMT supports only meshes generated by Netgen, however support for other kind of meshes can be added by subclassing the `mesh_parser` class (Fig. 7.4). When the `read_mesh()` method is called, it starts reading the mesh file. Mesh elements are added to a `tetrahedral_mesh` by calling the corresponding methods. At the end of the process the new mesh is added to the appropriate `mesh_store`, which makes the new mesh available system-wide.

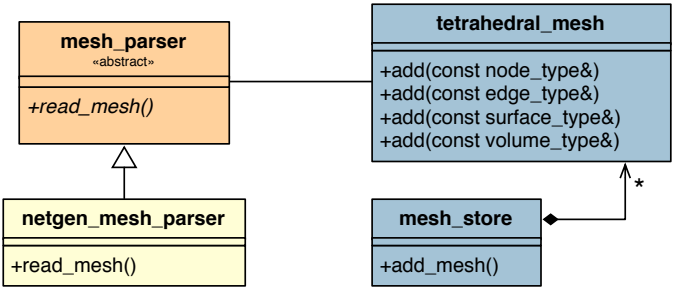

Figure 7.4: UML diagram of the classes involved in the handling of the meshes.

The `mesh` class template provides a number of methods to operate on the elements of the mesh, which will be described in this section.

Adding elements. When a parser reads a mesh file, it needs to add the geometric elements just read to the data structures. This is done by the `add` methods.

```
/* Add a single element */
void add(const volume_type&);

/* Add the range of elements specified by the two iterators */
void add(const typename std::vector<volume_type>::iterator,
         const typename std::vector<volume_type>::iterator);
```

Listing 3: Add methods for volumes. There are add methods available also for nodes, edges and surfaces.

In Listing 3 the signatures of the add methods for the volumes are shown. The first variant adds a single element, while the second variant adds a range. Add methods are available also for nodes, edges and surfaces.

Iterating the geometric elements. Geometric elements are iterated through specific iterators provided by the mesh. These iterators are returned by the methods `element_begin()` and `element_end()`, where `element` can be `nodes`, `edges`, `surfaces` or `volumes`.

```
1  for (auto itor = mesh.volumes_begin();
2       itor != mesh.volumes_end();
3       itor++)
4  {
5          auto vol = *itor;
6
7          /* Do whatever we want with the volume,
8           * for example calculate the barycenter */
9
10         point_type bar = barycenter(mesh, vol);
11 }
```

Listing 4: Example of cycling all elements to calculate their barycenter.

Obtaining information about boundaries and subdomains. It can be useful to

Finding clusters of volumes Sometimes is useful to know which volumes are attached to a node, to an edge or to a surface.

7.1.3 Declaration of a module

We can now return back to our module and look at how it is implemented. The module starts by declaring which boundary conditions are available. Our only boundary condition will be a Dirichlet condition, which we call `BC_POTENTIAL`. Moreover, `BC_NONE` and `BC_INVALID` must always be declared:

```
enum class conduction_bcs
{
  BC_NONE,
  BC_INVALID,
  BC_POTENTIAL
};
```

We then proceed to declaring the module class template, `conduction_module`, which is a subclass of `emt::ui::interactive`. This subclassing will allow to register the module as a textual user interface object, and enables the interaction between the user and the module. The module will contain its environment, a pointer to the mesh, the material parameters for each subdomain, the mapping between the boundaries and their boundary conditions, the linear system compressor and the linear system builders.

```
template<typename mesh_type, typename T>
class conduction_module : public emt::ui::interactive
{
  emt::env::environment                              _env;
  std::shared_ptr<mesh_type>                         _mesh;
  std::map<typename mesh_type::domain_id_type, T> _scalar_conductivities;
  boundary_mapper<mesh_type, conduction_bcs, T>   _boundary_mapper;
  system_compressor<T>                               _compressor;
  solvers::matrix_builder<T>                         _matbuilder;
  solvers::rhs_builder<T>                            _rhsbuilder;
```

7.1.4 Retrieving the mesh

The next task is to write a method which retrieves a mesh from the `mesh_store`. The mesh that will be used for the simulation is specified by the user in the environment variable `conduction.mesh`. The method reads that variable and checks if the specified mesh exists. If the mesh does not exists, a null pointer is returned. Moreover, if a mesh was not specified, the method tries to find the default mesh. Again, if the default mesh is not found, a null pointer is returned.

```
std::shared_ptr<mesh_type> get_mesh(void)
{
  std::string meshname = emt::env::getenv("mesh", _env);

  if ( meshname != "" && emt::geometry::mesh_exists<mesh_type>(meshname) )
    return emt::geometry::get_mesh<mesh_type>(meshname);

  if ( emt::geometry::mesh_exists<mesh_type>("default") )
  {
```

```
26      std::cout << red << "WARNING: " << nocolor;
27      std::cout << "specified mesh not found, using default" << std::endl;
28      return emt::geometry::get_mesh<mesh_type>(meshname);
29    }
30
31    return nullptr;
32  }
```

7.1.5 Retrieving the material parameters

The material parameters (σ) are specified by the user using some environment variables. For example, if the mesh is composed by two subdomains numbered 1 and 2, their conductivities are specified in the variables `domain1.material.sigma` and `domain2.material.sigma`. The task of the next method we must implement is to retrieve these variables:

```
33  bool get_material_parameters(void)
34  {
35    auto doms = _mesh->domains();
36    bool success = true;
37
38    for (auto& d : doms)
39    {
40      std::stringstream ss;
41      ss << "domain" << d.first << ".material.sigma";
42
43      std::string varname = ss.str();
44      std::string value = emt::env::getenv(varname, _env);
45
46      if (value == "")
47      {
48        std::cout << "Conductivity of domain " << d.first;
49        std::cout << " not set (" << varname << ")" << std::endl;
50        success = false;
51      }
52
53      _scalar_conductivities[d.first] = strtot<T>(value);
54    }
55
56    return success;
57  }
```

7.1.6 Boundary conditions

The task of the method that sets up boundary conditions reduces to building two arrays. The first array is an array of booleans that tells if a specific node is part of a boundary where a Dirichlet condition is applied, while the second array holds the values of the boundary condition (in our case the potential). Arrays are declared and initialized (lines 60-64) then, for each boundary, the elements are iterated and arrays are filled with the appropriate values. Finally, the arrays are used to initialize the linear system compressor (lines 88-89).

```
58 bool detect_dirichlet_conditions(void)
59 {
60   std::vector<bool>   is_dirichlet;
61   std::vector<T>      bc_value;
62
63   is_dirichlet.resize( _mesh->nodes_size() );
64   bc_value.resize( _mesh->nodes_size() );
65
66   auto boundaries = _mesh->boundaries();
67
68   for (auto& b : boundaries) {
69     auto bc = _boundary_mapper.get_bc(b.first);
70
71     switch (bc.bc_type) {
72       case conduction_bcs::BC_POTENTIAL:
73         for (auto itor = b.second.begin();
74              itor != b.second.end(); itor++) {
75           auto pts = (*itor).point_ids();
76           for (auto& pt : pts) {
77             is_dirichlet.at(pt) = true;
78             bc_value.at(pt) = bc.bc_value;
79           }
80         }
81         break;
82
83         default:
84           ;
85     }
86   }
87
88   _compressor.clear();
89   _compressor.init(is_dirichlet, bc_value);
90
91   return true;
92 }
```

The linear system compressor is a simple class which gives some aid when we need to apply the Dirichlet boundary conditions to the linear system. This kind of condition is imposed by removing from the matrix the rows corresponding to the elements where a Dirichlet BC is applied, and by moving the columns corresponding to the same elements to the right hand side, changing their sign and multiplying them by the value of the boundary condition. In this way a matrix smaller than the original one is obtained, and we call that matrix *compressed matrix*. The compressor is then responsible to provide the mapping between the elements of the starting matrix and the elements of the compressed matrix, and it is very useful during problem assembly.

7.1.7 Problem assembly

The methods described until now, despite being essential to successfully run a simulation, were just methods to gather data from somewhere and to put it in the right data structures. The method that does the problem assembly, on the other hand, is maybe one of the most interesting. Apart the initial declarations and initializations (lines 95-103), the for cycle (lines 105-126) iterates all the mesh elements, builds the local matrices $\mathbf{G}$ and $\mathbf{M}_\sigma$ (lines 115-118) and copies the computed data to the global linear system. Note how EMT (compare line 118 with 7.5), thanks to the flexibility of C++, allows to directly translate the equations in code.

```
93  bool assemble_problem(void)
94  {
95    _matbuilder.set_matrix_size( _compressor.system_size() );
96    auto matrix_assembly_lambda = [&](size_t i, size_t j, T val) {
97      _matbuilder.add_value(i, j, val);
98    };
99
100   _rhsbuilder.resize( _compressor.system_size() );
101   auto rhs_assembly_lambda = [&](size_t pos, T val) {
102     _rhsbuilder.add_value(pos, val);
103   };
104
105   for (auto itor = _mesh->volumes_begin();
106        itor != _mesh->volumes_end();
107        itor++)
108   {
109     auto vol = *itor;
110
111     auto nodes_l2g = vol.point_ids();
112
113     T sigma_vol = _scalar_conductivities.at( _mesh->domain_of(vol) );
114
115     auto G      = geometry::grad_matrix<T>(*_mesh, vol);
116     auto mSigma = geometry::edge_matrix(*_mesh, vol, sigma_vol);
117
```

```
118     arma::Mat<T> mLocal = -(trans(G) * mSigma * G);
119
120
121     for (size_t i = 0; i < nodes_l2g.size(); i++)
122       for (size_t j = 0; j < nodes_l2g.size(); j++)
123         _compressor.assemble(nodes_l2g[i], nodes_l2g[j],
124                              mLocal(i,j),
125                              matrix_assembly_lambda,
126                              rhs_assembly_lambda);
127   }
128   return true;
129 }
```

Note the use of the compressor (line 123): we ask it to `assemble()` the entries of our local matrix, which in the global uncompressed matrix would be at the positions `nodes_l2g[i]` and `nodes_l2g[j]`, by using the two lambda functions provided as fourth and fifth argument. The compressor then calls back the two lambdas, but with indices remapped to the compressed matrix.

7.1.8 Problem solution, numerical solvers

EMT is about modularity, and the interface to the solvers is no exception. The decoupling between numerical solvers and other parts of code is obtained through a *solver factory*. The `solver_factory` is a class that, by means of the *factory method* [GHJV94] `get_solver()` (Fig. 7.5), creates objects which type cannot be known in advance (i.e. at compile-time). In our case this means that, when writing a module, a programmer has just to make sure he received *a* solver from the system; the system *will* provide the right one, which is the one requested by the user via the `setenv solver cg` command. From the programmer's point of view, this means also that to add a solver, *no code* inside EMT has to be touched: it is sufficient to subclass `solver` and implement `initialize()` and `solve()`.

However, this is only half of the picture. Each solver expects to have the matrix and the right hand side in a specific format, for example CSR, CSC, COO and so on, but we don't want to expose these details to the clients. Here, the `matrix_builder` and `rhs_builder` we encountered in Section 7.1.7 come into play. These classes provide the method `add_value()`, which expects a row index, a column index and a value in the matrix case, while an index and a value in the rhs case. During the assembly phase, computed entries are passed to the builders, which store them in some internal format. Then, during the solution phase, the solver is asked to `initialize()` with the `matrix_bulder` and the `rhs_builder` used in the previous step. The call is then dispatched to the `initialize()` method of the correct solver, which transforms the internal format of the builders in the solver-specific format.

Thanks to this structure, clients have *no knowledge* about the various solvers interfaced to EMT and, as long as a solver is present, each module can automatically make use of it.

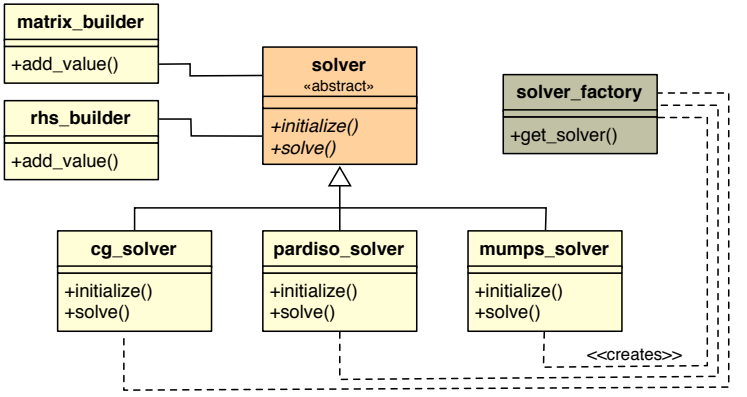

Figure 7.5: UML diagram of the classes implementing the solvers.

```
130 bool solve(void)
131 {
132   /* Solution phase */
133   std::string solver_name = emt::env::getenv("solver", _env);
134
135   if ( solver_name == "" ) {
136     std::cout << "Solver not set, cannot continue" << std::endl;
137     return false;
138   }
139
140   /* Try to get the solver specified by the user */
141   std::shared_ptr<emt::solvers::solver<T>> solver;
142
143   try {
144     solver = emt::solvers::get_factory<T>()->create(solver_name);
145   }
146
147   catch (...) {
148     /* Invalid solved specified, handle the situation */
149     return false;
150   }
151
152   /* Note: we know _nothing_ about the solver */
153
154   /* Initialize it... */
155   solver->initialize(_matbuilder, _rhsbuilder);
156
157   std::vector<T> solution;
158   solution.resize(_compressor.system_size());
159
```

```
160  /* ...and call it. */
161  solver->solve(solution);
```

7.1.9 Postprocessing

Postprocessing is needed to recover the physical fields from the degrees of freedom computed as solution. In the case of the `conduction` module, we want to recover the fields $\boldsymbol{E}$ and $\boldsymbol{J}$ from the potentials V. Fields are recovered using (7.2) and (7.3), which in the discrete domain become $\mathbf{U} = -\mathbf{G}\mathbf{V}$ and $\tilde{\mathbf{I}} = \mathbf{M}_\sigma \mathbf{U}$. Once $\mathbf{U}$ and $\tilde{\mathbf{I}}$ are computed tetrahedron by tetrahedron, they can be interpolated by using the appropriate basis functions, which are the primal edge functions for $\mathbf{U}$ and the dual face functions for $\tilde{\mathbf{I}}$. Note how, also in this case, discrete equations are directly translated to code.

```
162  /* Postprocessing phase */
163
164  std::vector<T> sol(_mesh->nodes_size());
165  _compressor.expand(solution.begin(), solution.end(), sol.begin());
166
167  emt::dataio::silo silo;
168  silo.create("conduction.silo");
169  silo.export_mesh(*_mesh);
170
171  emt::dataio::silo_nodal_variable<T> potential("potential", sol);
172  silo.export_variable(_mesh->name(), potential);
173
174  std::vector<vec3<T>> E_vals, J_vals;
175  E_vals.reserve( _mesh->volumes_size() );
176  J_vals.reserve( _mesh->volumes_size() );
177
178  for (auto itor = _mesh->volumes_begin();
179       itor != _mesh->volumes_end();
180       itor++)
181  {
182    auto vol = *itor;
183
184    auto G = geometry::grad_matrix<T>(*_mesh, vol);
185    auto V = geometry::nodal_quantities(*_mesh, vol, sol);
186    arma::Col<T> U = -G*V;
187
188    auto E = geometry::primal_edge_interpolator(*_mesh, vol, U);
189    E_vals.push_back( geometry::vec_avg(E) );
190
191    T sigma_vol = _scalar_conductivities.at(_mesh->domain_of(vol) );
192
193    auto mSigma = geometry::edge_matrix(*_mesh, vol, sigma_vol);
```

```
194
195     arma::Col<T> I = mSigma*U;
196
197     auto J = geometry::dual_face_interpolator(*_mesh, vol, I);
198     J_vals.push_back( geometry::vec_avg(J) );
199
200   }
201
202   emt::dataio::silo_zonal_variable<vec3<T>> E("E", E_vals);
203   silo.export_variable(_mesh->name(), E);
204
205   emt::dataio::silo_zonal_variable<vec3<T>> J("J", J_vals);
206   silo.export_variable(_mesh->name(), J);
207
208   silo.close();
209
210   return true;
211 }
```

7.1.10 Data export

EMT exports data in various formats, however the most useful one is PDB. PDB files are created through the SILO library and visualized with the VisIt software. The SILO library is abstracted through the `silo` class, which makes data export quite easy. To export the simulation data, a `silo` object has to be created (line 167). Then, through the `create()` method, a PDB database is created and initialized (line 168). The next step is to export the mesh to the database, by calling `export_mesh()` (line 169). We are now ready to add the data to the output database.

SILO recognizes two kinds of variables, namely the *nodal variables*, which are associated to the nodes of the mesh, and the *zonal variables*, which are associated to the volumes of the mesh. An example of a nodal variable is the potential on the nodes of a mesh, while an example of a zonal variable is the electric field on a volume of the mesh. They are represented in EMT by the `silo_nodal_variable` and `silo_zonal_variable` class templates. The constructor of these two classes accepts a name and an array of values as parameters (lines 171, 202 and 205): the name will be displayed in VisIt, while the array of values contains the variable values for each node or for each volume. As a final step, variables are exported to the database by means of the method `export_variable()` (lines 172, 203 and 206) and the database is closed by calling `close()` (line 208).

7.1.11 Putting all together

In the previous sections a number of methods needed to setup the simulation were discussed. However, these methods must be called in some way, and this is the purpose of the `run()` method that we are about to discuss. This method is directly bound to

the `run` command in the script: issuing `run` at the command line has the effect to call `run()` in the module, which in turn calls all the methods we described previously.

Before doing anything, however, we must set the boundary conditions up. Boundary conditions are stored in objects of type `boundary_mapper`. Two methods are important here, namely `create_bc()` and `associate_bc()`. The first method is used to create a boundary condition, give it a value and associate a name to it (lines 214-215). That name will then be used to associate the condition to the actual boundaries using the method `associate_bc()` (lines 218-219). In this example module, the boundary conditions are hardcoded for ease of explanation, however the methods of the boundary mapper are usually bound to some kind of boundary condition database, which in turn allows the user to specify the boundary conditions in the script.

```
212 bool run(const std::vector<std::string>& args)
213 {
214   _boundary_mapper.create_bc("10V", conduction_bcs::BC_POTENTIAL, 10);
215   _boundary_mapper.create_bc("0V", conduction_bcs::BC_POTENTIAL, 0);
216
217   /* 'typename' suppressed for space reasons */
218   _boundary_mapper.associate_bc(mesh_type::boundary_id_type(3), "10V");
219   _boundary_mapper.associate_bc(mesh_type::boundary_id_type(6), "0V");
220
221   _mesh = get_mesh();
222   if (_mesh == nullptr) {
223     std::cout << "Unable to get a mesh" << std::endl;
224     return false;
225   }
226
227   if ( !get_material_parameters() ) {
228     std::cout << "Error while looking up material parameters" << std::endl;
229     return false;
230   }
231
232   if ( !detect_dirichlet_conditions() ) {
233     std::cout << "Error while applying boundary conditions" << std::endl;
234     return false;
235   }
236
237   if ( !assemble_problem() ) {
238     std::cout << "Error assembling problem" << std::endl;
239     return false;
240   }
241
242   if ( !solve() ) {
243     std::cout << "Error while solving" << std::endl;
244     return false;
245   }
```

```
246
247   return true;
248 }
```

7.2 Discussion

In the previous section some details about the implementation of a module for EMT were presented. The module that solves the stationary conduction problem was analyzed in detail, discussing all the methods that need to be implemented to solve this particular problem. The resulting module is less than 250 lines of code, which means that any programmer with an average C++ knowledge should have no trouble in writing his own module. Obviously this requires a minimal confidence with the whole EMT structure, however the API should be sufficiently high-level to isolate the programmer from most of the implementation details.

8

Conclusions

This thesis investigated some novel numerical techniques to simulate electrically large anechoic chambers. As detailed in Chapter 3, this kind of problem is quite difficult from the numerical point of view and requires some care to be solved. The proposal of this thesis is to use equivalent models, simplifying the geometrical structure of the numerical models that are to be simulated.

The development of the mentioned equivalent models required a prior extension of the DGA method with a number of features not available before, in particular the Plane Wave condition and the equivalent antenna. The plane wave condition allowed to study the *unit cell*, which is a small piece of anechoic wall with microwave absorbers and ferrite tiles. The unit cell then allowed to model an entire anechoic wall as an equivalent impedance. The equivalent antenna, on the other hand, permits to insert into the simulated anechoic chambers antennas with specific characteristics, modeled as equivalent radiating spheres.

The proposed models, as detailed in Chapter 6, discard lots of geometric information and thus introduce significant approximations. Despite that, they preserve a very good degree of accuracy, accuracy that was verified with an extensive set of measurements, comprising 558 comparisons with the simulations. Simulations agreed with the measurements in more than the 90% of the cases, thus confirming that this kind of simulation can be successfully employed to evaluate the performance of large anechoic chambers. Moreover, we remark that in one of the cases where discrepancies were high, simulation allowed to detect that measurements were flawed. This opens the possibility to do a rather unusual thing, which is the validation of the measurements using simulation. Because accurate RF measurements are quite difficult to do and require carefully controlled sites, once simulation is correctly set up it can be of great help in verifying their correctness.

Simulation is a great tool also to evaluate the field uniformity inside an anechoic chamber: the presence of objects like tables or antenna masts can introduce unwanted and unforeseen field distortions, effects almost impossible to detect only with measurements.

The prediction of the field configuration inside anechoic chambers is only one of the

possibilities to apply simulation to electromagnetic compatibility problems, and there are many research areas on this topic still open or just at their beginning. In Chapter 5, the $\boldsymbol{a}$-V formulation was introduced: this is the starting point to study immunity problems, both radiated and conducted. By coupling the electromagnetic field simulation with the circuit simulation, it can be possible to evaluate the effect of an incident electromagnetic field on the electronics of the device under test. This can be particularly significant in testing automobile parts. For example, car lights are usually tested for immunity by placing them in an anechoic chamber and by irradiating them with a prescribed field: the light should not turn off or present glitches. Simulation can be used to predict this kind of phenomena and solve or mitigate them before doing the actual testing.

Some numerical and theoretical points need also to be investigated, in particular domain decomposition and model order reduction. Domain decomposition is useful to enable the simulation of anechoic chambers at higher frequencies, while model order reduction can be applied to do fast frequency sweeps without the need to compute the solution of the problem at each frequency. The topic of complementarity is also not closed: the main question is why there are no bilateral energy bound.

By providing the tools to simulate large anechoic chambers, this thesis only scratched the surface of the electromagnetic simulation applied to electromagnetic compatibility. In the future years, thanks to the availability of powerful hardware and more sophisticated numerical techniques, this will be a rich research field.

IV

Appendices

A

Quaternions

Quaternions are an extension of complex numbers and were discovered and first described in 1843 by Sir William Rowan Hamilton. Quaternions find applications in theoretical and applied mathematics, mechanics, computer graphics, computer vision, flight dynamics, orbital mechanics, special relativity and more [CZPM92, DL96, Muk02, Jac03, AC04, CS10], since they provide, among other things, a simple formalism to describe rotations in 3-dimensional space. Moreover, when employed for rotations, they have many advantages over other techniques like rotation matrices or Euler angles. In particular, rotations by quaternions are easy to combine, don't suffer from the gimbal lock problem, are numerically more stable than rotation matrices and could be computationally cheaper. Despite all the advantages, few people knows about the existence of quaternions. Since quaternions are used in EMT and are essential in the interaction with the user, in this appendix a brief introduction will be given. However, only details useful for running the code are discussed, an in-depth explanation can be found in [Vin11]. Wikipedia also has good articles on the topic.

A.1 Basic definitions

Quaternions are based on the fundamental identity which relates their *three imaginary units* $\boldsymbol{i}, \boldsymbol{j}, \boldsymbol{k}$

$$\boldsymbol{i}^2 = \boldsymbol{j}^2 = \boldsymbol{k}^2 = \boldsymbol{ijk} = -1. \tag{A.1}$$

The set $\mathbb{H} = \{(a, b, c, d) \,|\, a, b, c, d \in \mathbb{R}\}$ of quaternions is a 4-dimensional vector space over the real numbers. If a basis for $\mathbb{R}^4$ is chosen, being $1, \boldsymbol{i}, \boldsymbol{j}$ and $\boldsymbol{k}$ its elements, each element of $\mathbb{H}$ can be uniquely written as a linear combination of the elements of that basis as $\boldsymbol{q} = a1 + b\boldsymbol{i} + c\boldsymbol{j} + d\boldsymbol{k}$. The element 1 is the identity element of $\mathbb{H}$ and thus its elements are usually written as $\boldsymbol{q} = a + b\boldsymbol{i} + c\boldsymbol{j} + d\boldsymbol{k}$. A quaternion of the type $a + 0\boldsymbol{i} + 0\boldsymbol{j} + 0\boldsymbol{k}$ is called *real*, while one of the type $0 + b\boldsymbol{i} + c\boldsymbol{j} + d\boldsymbol{k}$ is called *pure imaginary*. Moreover, a is called *scalar part* while $b\boldsymbol{i} + c\boldsymbol{j} + d\boldsymbol{k}$ is called *vector part*.

Three operations are defined on $\mathbb{H}$, namely the addition, the scalar multiplication and the quaternion multiplication. Given two quaternions $\boldsymbol{q}_1, \boldsymbol{q}_2$ we define the addition

$$\boldsymbol{q}_1 + \boldsymbol{q}_2 = a_1 + a_2 + (b_1 + b_2)\boldsymbol{i} + (c_1 + c_2)\boldsymbol{j} + (d_1 + d_2)\boldsymbol{k} \tag{A.2}$$

and the product by a scalar s

$$\boldsymbol{q}s = s\boldsymbol{q} = as + bs\boldsymbol{i} + cs\boldsymbol{j} + ds\boldsymbol{k}. \tag{A.3}$$

There is also the *quaternion multiplication* or *Hamilton multiplication*, which is defined between elements of $\mathbb{H}$ and is noncommutative

$$\begin{aligned}\boldsymbol{q}_1\boldsymbol{q}_2 = {} & a_1a_2 + a_1b_2\boldsymbol{i} + a_1c_2\boldsymbol{j} + a_1d_2\boldsymbol{k} \\ & + b_1a_2\boldsymbol{i} + b_1b_2\boldsymbol{i}^2 + b_1c_2\boldsymbol{i}\boldsymbol{j} + b_1d_2\boldsymbol{i}\boldsymbol{k} \\ & + c_1a_2\boldsymbol{j} + c_1b_2\boldsymbol{j}\boldsymbol{i} + c_1c_2\boldsymbol{j}^2 + c_1d_2\boldsymbol{j}\boldsymbol{k} \\ & + d_1a_2\boldsymbol{k} + d_1b_2\boldsymbol{k}\boldsymbol{i} + d_1c_2\boldsymbol{k}\boldsymbol{j} + d_1d_2\boldsymbol{k}^2,\end{aligned} \tag{A.4}$$

or, rearranging

$$\begin{aligned}\boldsymbol{q}_1\boldsymbol{q}_2 = {} & a_1a_2 - b_1b_2 - c_1c_2 - d_1d_2 \\ & + (a_1b_2 + b_1a_2 + c_1d_2 - d_1c_2)\boldsymbol{i} \\ & + (a_1c_2 - b_1d_2 + c_1a_2 + d_1b_2)\boldsymbol{j} \\ & + (a_1d_2 + b_1c_2 - c_1b_2 + d_1a_2)\boldsymbol{k}.\end{aligned} \tag{A.5}$$

Moreover, we define the conjugate of the quaternion $\boldsymbol{q} = a + b\boldsymbol{i} + c\boldsymbol{j} + d\boldsymbol{k}$ to be

$$\boldsymbol{q}^* = a - b\boldsymbol{i} - c\boldsymbol{j} - d\boldsymbol{k}, \tag{A.6}$$

the norm

$$||q|| = \sqrt{\boldsymbol{q}\boldsymbol{q}^*} = \sqrt{a^2 + b^2 + c^2 + d^2}, \tag{A.7}$$

and the inverse

$$\boldsymbol{q}^{-1} = \frac{\boldsymbol{q}^*}{||\boldsymbol{q}||^2}. \tag{A.8}$$

Finally, the unit quaternion $\hat{q}$ is defined as

$$\hat{\boldsymbol{q}} = \frac{\boldsymbol{q}}{||\boldsymbol{q}||}. \tag{A.9}$$

A.2 Rotations using quaternions

A rotation around the unit vector $\hat{\boldsymbol{u}}$ by an angle θ can be represented by the unit quaternion

$$\hat{\boldsymbol{q}} = e^{\frac{\theta}{2}(u_x\boldsymbol{i} + u_y\boldsymbol{j} + u_z\boldsymbol{k})} = \cos\frac{\theta}{2} + (u_x\boldsymbol{i} + u_y\boldsymbol{j} + u_z\boldsymbol{k})\sin\frac{\theta}{2}. \tag{A.10}$$

If, abusing the notation, we identify a vector $\boldsymbol{p} \in \mathbb{R}^3$ with the quaternion $\boldsymbol{p} = 0 + p_x\boldsymbol{i} + p_y\boldsymbol{j} + p_z\boldsymbol{k}$, rotation can be actually done by means of the *conjugation* of $\boldsymbol{p}$ by $\boldsymbol{q}$

$$\boldsymbol{p}' = \hat{\boldsymbol{q}}\boldsymbol{p}\hat{\boldsymbol{q}}^{-1} \tag{A.11}$$

Example: Given the vector $\boldsymbol{v} = (1, 0, 0)$, rotate it by $\frac{\pi}{2}$ radians around the z axis.

The z axis is represented by the unit vector $\boldsymbol{k}$ and, since we want a rotation of $\frac{\pi}{2}$, our rotation quaternion $\hat{\boldsymbol{q}}$ will be

$$\hat{\boldsymbol{q}} = e^{\frac{\pi}{4}\boldsymbol{k}} = \frac{\sqrt{2}}{2} + \frac{\sqrt{2}}{2}\boldsymbol{k}. \tag{A.12}$$

The rotation is computed as

$$\boldsymbol{v}' = \hat{\boldsymbol{q}}\boldsymbol{v}\hat{\boldsymbol{q}}^{-1} = \hat{\boldsymbol{q}}\boldsymbol{v}\left(\frac{\sqrt{2}}{2}, 0, 0, -\frac{\sqrt{2}}{2}\right) = \hat{\boldsymbol{q}}\left(0, \frac{2}{\sqrt{2}}, \frac{2}{\sqrt{2}}, 0\right) = \tag{A.13}$$

$$= \left(\frac{\sqrt{2}}{2}, 0, 0, \frac{\sqrt{2}}{2}\right)\left(0, \frac{2}{\sqrt{2}}, \frac{2}{\sqrt{2}}, 0\right) = (0, 0, 1, 0) \tag{A.14}$$

As expected, we obtained $\boldsymbol{v}' = (0, 1, 0)$, which is an unit vector directed along y.

Rotations are easily combined: given two rotation quaternions $\hat{\boldsymbol{q}}_1$ and $\hat{\boldsymbol{q}}_2$, the quaternion representing the overall rotation is obtained computing the product $\hat{\boldsymbol{q}}_t = \hat{\boldsymbol{q}}_2\hat{\boldsymbol{q}}_1$ (note that the last rotation comes first). Then, the actual rotation of $\boldsymbol{p}$ is made by computing $\boldsymbol{p}' = \hat{\boldsymbol{q}}_t\boldsymbol{p}\hat{\boldsymbol{q}}_t^{-1}$. Finally, rotations are easily undone: if we computed $\boldsymbol{p}' = \hat{\boldsymbol{q}}\boldsymbol{p}\hat{\boldsymbol{q}}^{-1}$, it is possible to get back $\boldsymbol{p}$ computing $\boldsymbol{p} = \hat{\boldsymbol{q}}^{-1}\boldsymbol{p}'\hat{\boldsymbol{q}}$.

A.3 Quaternions in the code

```
radiator halfwavedipole 2
enter radiator
    set current 1.26e-4
    set length 0.587/2
    set position 2.565 2.3 1.5
    set rotation add pi/2 0 1 0
    set rotation add 1.28 0 0 1
exit
```

Listing 5: Example script where the prototype dipole is rotated using quaternions.

As already stated, quaternions are used in EMT to rotate the simulated dipole. In a script, a dipole is added with the command `radiator <type> <subdomain>`. Then, the `radiator` context is entered and an arbitrary number of rotations can be added with the command `set rotation add`, which is used to specify a rotation quaternion (example script below). Rotations are then combined and used to rotate the field computed with the expressions (4.29) and (4.30), which assume the dipole oriented along z.

B

Measurement data

In this appendix the raw data obtained by the measurements is provided. The first three tables contain the data of the measurements done with the transmitting antenna in horizontal polarization, while the following three tables contain the data of vertical polarization. Receiving antenna was placed at a distance of 3 meters in horizontal polarization and measurements were taken at heights of 1 meter, 1.5 meters and 2 meters. Each table has the following columns:

- MHz: frequency of the measurement in MHz,
- Power: power measured at the output of the comb generator in dBm,
- Re(Z): real part of the transmitting antenna impedance in Ohm,
- Im(Z): imaginary part of the transmitting antenna impedance in Ohm,
- M 1m: field measurement with receiving antenna at h=1m in $dB\mu V/m$,
- S 1m: simulation result at h=1m in $dB\mu V/m$,
- M 1.5m: field measurement with receiving antenna at h=1.5m in $dB\mu V/m$,
- S 1.5m: simulation result at h=1.5m in $dB\mu V/m$,
- M 2m: field measurement with receiving antenna at h=2m in $dB\mu V/m$,
- S 2m: simulation result at h=2m in $dB\mu V/m$,

B.1 Raw data of the Measurement Group 1

Table B.1: Measurement data of the first group: transmitting antenna at h=1m, horizontal polarization.

MHz	Power	Re(Z)	Im(Z)	M 1m	S 1m	M 1.5m	S 1.5m	M 2m	S 2m
90	-31.88	207.41	-575.22	38.82	32.78	40.97	34.54	41.96	36.23
100	-27.91	234.90	-529.82	44.14	40.50	46.01	41.99	47.63	43.31
110	-32.00	136.54	-532.79	43.83	39.71	45.29	40.88	45.88	41.68
120	-28.23	196.07	-494.60	48.87	45.88	50.42	47.34	50.22	47.89
130	-31.86	120.24	-504.11	48.03	44.45	49.58	46.02	49.39	46.84
140	-28.35	47.42	-404.56	52.59	52.53	54.34	53.36	53.93	53.73
150	-31.91	53.76	-327.49	51.83	52.36	53.29	53.16	53.21	52.87
160	-28.48	61.27	-279.39	57.39	58.43	58.12	59.29	57.56	58.68
170	-32.29	59.82	-244.00	56.19	57.08	56.65	57.56	55.76	56.79
180	-28.39	53.45	-206.33	62.98	63.30	63.09	63.77	62.23	61.95
190	-32.91	51.28	-164.84	61.44	60.75	61.47	60.99	60.03	58.87
200	-28.70	49.39	-126.87	67.66	67.52	67.49	67.26	64.99	64.74
210	-32.90	46.83	-83.94	65.58	66.36	65.38	65.65	62.54	61.20
220	-28.89	55.47	-37.58	71.90	71.91	70.67	71.06	66.93	66.12
230	-32.90	68.92	2.85	69.06	68.37	66.69	67.63	62.16	61.28
240	-29.20	87.10	39.78	70.53	71.35	68.85	70.11	64.32	62.50
250	-32.90	103.76	67.66	66.37	66.19	65.43	64.18	59.24	56.23
260	-29.50	114.20	99.05	68.18	68.48	66.53	65.59	58.71	49.03
270	-33.05	131.43	133.17	63.86	63.83	60.86	60.91	51.74	48.88
280	-29.57	148.29	158.60	66.98	67.38	62.31	64.00	44.86	56.30
290	-33.20	155.33	189.31	61.95	63.35	57.25	58.46	41.15	52.74
300	-29.98	164.54	236.66	66.07	64.74	60.69	59.33	54.32	55.60
310	-33.54	203.86	287.10	61.72	59.62	54.62	52.41	51.20	55.57
320	-30.21	257.90	299.11	64.86	62.84	53.58	53.37	57.57	59.55
330	-33.75	270.35	297.50	60.54	58.84	48.36	49.55	55.71	56.26
340	-30.49	268.19	323.88	63.66	61.50	51.38	49.55	59.23	61.67
350	-33.73	281.42	373.08	60.18	57.58	46.96	40.50	55.89	58.31
360	-30.55	328.79	433.85	60.68	57.45	49.85	48.17	57.56	59.97
370	-33.55	432.17	375.79	57.99	54.66	46.47	40.81	56.94	58.18
380	-30.71	371.26	415.54	60.30	56.86	49.41	53.36	60.45	61.57
390	-33.27	433.79	468.76	57.51	50.98	49.01	49.67	58.56	59.42

B.2 Raw data of the Measurement Group 2

Table B.2: Measurement data of the second group: transmitting antenna at h=1.5m, horizontal polarization.

MHz	Power	Re(Z)	Im(Z)	M 1m	S 1m	M 1.5m	S 1.5m	M 2m	S 2m
90	-31.88	314.98	-717.15	41.27	32.62	43.07	34.47	44.19	35.01
100	-27.91	183.26	-771.83	46.81	39.60	47.51	41.18	47.67	41.34
110	-32.00	85.34	-524.85	45.16	41.38	46.27	42.56	46.32	42.25
120	-28.23	121.56	-447.47	50.28	48.89	51.20	49.40	50.44	48.12
130	-31.86	128.11	-413.23	49.88	47.75	49.97	47.91	48.52	45.79
140	-28.35	116.90	-393.08	54.44	53.19	53.96	53.62	51.12	50.87
150	-31.91	67.41	-353.88	53.06	52.56	52.66	52.52	49.53	48.89
160	-28.48	80.47	-284.13	58.35	59.13	57.62	57.31	52.27	52.81
170	-32.29	71.67	-248.67	56.82	57.50	54.45	55.61	49.50	49.08
180	-28.39	69.33	-218.41	63.33	63.13	59.79	61.07	54.13	49.33
190	-32.91	51.28	-177.88	61.38	60.63	57.88	56.52	48.94	45.67
200	-28.70	52.29	-132.30	67.02	67.13	62.05	61.81	51.64	54.86
210	-32.90	51.16	-90.74	64.78	64.99	57.09	58.04	54.86	57.69
220	-28.89	53.54	-47.52	70.78	71.13	59.96	62.83	64.59	66.09
230	-32.90	59.23	-3.43	67.74	68.54	57.98	58.00	64.61	64.47
240	-29.20	73.23	40.99	69.43	70.79	59.26	60.12	67.83	67.25
250	-32.90	91.78	74.82	64.95	64.33	52.05	48.84	63.79	63.27
260	-29.50	103.54	107.28	65.74	65.63	55.93	55.76	64.47	67.77
270	-33.05	118.54	142.85	59.18	61.39	54.59	57.26	61.90	64.45
280	-29.57	140.02	173.71	61.94	63.92	59.25	61.49	66.70	66.69
290	-33.20	156.89	200.18	56.70	57.80	55.83	56.41	61.99	61.07
300	-29.98	175.90	226.12	60.23	59.17	61.74	61.12	65.53	64.32
310	-33.54	189.70	242.48	53.57	54.13	58.46	60.55	59.83	60.23
320	-30.21	195.56	266.14	55.70	55.09	62.98	63.61	63.21	62.21
330	-33.75	209.67	297.15	49.90	49.88	60.61	59.10	58.94	57.28
340	-30.49	231.56	325.06	50.72	47.56	63.86	63.74	59.53	57.36
350	-33.73	249.30	343.13	41.80	45.73	59.83	60.00	53.96	50.49
360	-30.55	284.54	376.38	47.27	49.59	61.28	62.33	55.61	54.35
370	-33.55	307.03	335.77	45.38	46.75	59.81	61.45	51.40	41.24
380	-30.71	313.72	353.36	51.72	56.13	61.59	62.99	51.98	53.42
390	-33.27	281.39	340.02	50.44	54.82	58.69	61.26	50.31	51.92

B.3 Raw data of the Measurement Group 3

Table B.3: Measurement data of the third group: transmitting antenna at h=2m, horizontal polarization.

MHz	Power	Re(Z)	Im(Z)	M 1m	S 1m	M 1.5m	S 1.5m	M 2m	S 2m
90	-31.88	158.46	-680.82	41.85	34.74	43.01	36.15	42.04	35.61
100	-27.91	195.71	-552.19	46.72	43.03	47.59	43.98	46.31	42.59
110	-32.00	116.82	-586.15	44.81	40.68	45.45	41.36	43.68	39.37
120	-28.23	149.68	-459.25	49.61	48.41	50.07	47.95	47.77	44.62
130	-31.86	153.91	-451.38	48.85	47.23	48.05	45.26	43.49	39.27
140	-28.35	73.47	-431.17	53.95	52.93	50.98	50.70	43.55	43.53
150	-31.91	69.19	-335.78	51.90	52.53	47.87	49.66	41.06	41.59
160	-28.48	75.29	-294.63	57.43	58.12	51.73	52.83	48.89	47.75
170	-32.29	66.74	-253.79	55.07	56.41	48.72	49.56	48.86	50.08
180	-28.39	61.72	-216.36	62.17	61.72	53.80	50.28	57.21	58.08
190	-32.91	53.67	-173.46	59.08	58.81	48.03	46.19	57.00	57.19
200	-28.70	54.53	-128.48	64.15	64.93	50.31	54.45	63.64	66.03
210	-32.90	57.45	-89.70	61.10	61.16	53.30	57.12	62.56	64.41
220	-28.89	59.35	-49.84	65.18	66.38	64.52	65.53	69.69	70.47
230	-32.90	64.83	-8.39	61.95	62.70	64.27	63.71	67.56	67.31
240	-29.20	70.91	34.48	63.70	65.38	67.84	67.50	69.54	69.85
250	-32.90	89.54	76.36	56.99	59.26	64.48	63.51	64.33	63.27
260	-29.50	103.89	106.70	54.63	55.49	64.53	67.96	64.30	64.45
270	-33.05	118.77	140.46	48.92	43.64	60.61	64.53	59.20	58.95
280	-29.57	135.27	167.14	50.54	54.97	65.57	66.85	60.06	59.03
290	-33.20	140.18	195.06	45.13	51.04	60.39	61.88	50.92	49.98
300	-29.98	153.84	242.45	53.99	51.05	64.11	64.74	55.22	54.12
310	-33.54	188.91	261.42	49.15	54.32	58.55	60.33	46.41	54.42
320	-30.21	202.62	274.44	55.11	59.86	62.58	62.53	52.65	58.81
330	-33.75	217.05	295.52	55.34	55.38	58.15	57.86	54.16	57.98
340	-30.49	221.13	318.27	59.33	60.42	60.71	58.10	59.70	63.36
350	-33.73	240.53	347.92	56.81	58.13	55.71	52.24	57.84	58.48
360	-30.55	281.69	353.31	58.68	60.60	55.33	55.46	60.39	61.83
370	-33.55	272.29	340.79	58.47	60.05	50.27	42.98	58.84	60.16
380	-30.71	260.34	358.13	60.45	62.92	45.02	53.76	60.42	61.65
390	-33.27	260.82	390.94	57.79	61.19	46.75	52.63	58.18	59.30

B.4 Raw data of the Measurement Group 4

Table B.4: Measurement data of the first group: transmitting antenna at h=1m, vertical polarization.

MHz	Power	Re(Z)	Im(Z)	M 1m	S 1m	M 1.5m	S 1.5m	M 2m	S 2m
90	-31.88	204.08	-576.82	36.00	35.75	33.75	34.28	35.30	31.71
100	-27.91	233.08	-529.38	42.72	41.66	41.14	39.75	38.79	36.40
110	-32.00	119.93	-534.36	37.88	39.65	33.13	37.10	37.48	33.13
120	-28.23	197.98	-496.70	46.27	45.42	43.39	42.55	41.53	38.63
130	-31.86	116.39	-511.46	41.10	43.95	34.33	40.91	37.32	37.08
140	-28.35	31.19	-399.87	49.92	51.26	46.50	48.15	45.63	44.60
150	-31.91	49.84	-314.84	45.69	50.39	34.62	47.06	39.39	44.04
160	-28.48	63.14	-268.08	54.31	55.89	51.12	51.94	52.50	50.40
170	-32.29	66.07	-232.44	49.01	53.47	36.54	49.17	43.47	49.29
180	-28.39	65.72	-197.61	57.96	57.66	52.97	53.36	56.16	55.60
190	-32.91	64.85	-164.78	50.98	53.12	41.90	48.55	51.13	53.97
200	-28.70	56.30	-131.41	55.85	56.92	55.94	56.82	60.07	61.94
210	-32.90	50.28	-83.91	52.10	56.00	51.64	58.49	56.02	61.97
220	-28.89	62.38	-40.38	56.32	63.61	63.32	65.33	64.77	68.21
230	-32.90	71.66	-3.77	58.29	60.51	60.96	62.12	62.51	64.85
240	-29.20	82.39	24.10	62.02	62.25	63.98	64.86	65.47	67.74
250	-32.90	83.91	61.14	60.99	56.93	60.55	61.86	62.97	64.26
260	-29.50	93.36	104.19	54.07	60.65	61.06	65.84	62.94	67.41
270	-33.05	113.52	142.79	58.05	56.03	59.92	61.48	63.67	62.55
280	-29.57	131.89	176.76	54.92	57.75	61.84	63.81	61.76	64.55
290	-33.20	157.66	205.11	47.25	54.61	59.90	59.67	62.27	59.68
300	-29.98	174.93	225.71	52.81	60.22	61.00	63.69	60.59	62.19
310	-33.54	191.28	257.39	49.78	56.90	59.50	60.16	59.16	57.55
320	-30.21	221.22	272.76	55.59	59.76	59.28	62.96	56.71	59.91
330	-33.75	235.12	283.28	50.98	56.37	55.77	59.31	55.77	56.16
340	-30.49	242.44	300.77	58.59	60.06	61.45	63.08	57.65	58.91
350	-33.73	254.05	324.32	53.03	57.16	53.52	59.45	49.85	54.34
360	-30.55	272.56	355.52	58.31	60.16	59.80	61.68	55.11	56.27
370	-33.55	313.04	338.44	54.54	58.06	55.90	58.89	51.59	51.10
380	-30.71	300.86	361.88	58.32	61.76	59.90	60.96	54.02	52.29
390	-33.27	325.01	371.46	54.81	58.72	55.10	58.04	51.45	49.40

B.5 Raw data of the Measurement Group 5

Table B.5: Measurement data of the first group: transmitting antenna at h=1.5m, vertical polarization.

MHz	Power	Re(Z)	Im(Z)	M 1m	S 1m	M 1.5m	S 1.5m	M 2m	S 2m
90	-31.88	330.58	-700.31	36.32	32.30	35.16	30.25	37.16	27.59
100	-27.91	212.24	-759.80	40.81	37.41	40.63	34.75	40.85	32.50
110	-32.00	102.76	-528.33	35.13	37.92	35.46	35.00	38.70	34.41
120	-28.23	134.92	-451.02	43.39	44.48	42.61	42.34	44.84	42.79
130	-31.86	140.08	-416.73	36.22	43.19	37.78	41.43	41.69	42.60
140	-28.35	132.20	-395.99	46.27	48.85	47.40	47.44	49.28	49.15
150	-31.91	81.56	-370.03	39.39	46.88	41.07	46.31	44.80	48.31
160	-28.48	82.53	-298.40	50.10	52.65	53.57	53.13	55.72	55.16
170	-32.29	70.46	-258.41	41.46	50.82	47.86	51.67	50.36	54.08
180	-28.39	66.66	-221.59	51.82	54.97	58.15	57.91	60.27	60.13
190	-32.91	52.00	-178.49	43.58	51.44	55.41	56.38	56.87	58.11
200	-28.70	53.35	-129.74	55.67	59.08	63.67	64.13	63.68	64.79
210	-32.90	58.40	-88.65	53.93	58.52	61.14	63.04	61.01	62.25
220	-28.89	61.63	-47.48	64.01	65.75	67.91	69.37	66.08	67.55
230	-32.90	70.53	-6.82	62.99	62.26	65.94	65.64	63.53	63.65
240	-29.20	80.25	31.55	65.92	65.25	67.61	68.62	64.10	66.14
250	-32.90	94.07	69.50	62.46	61.24	65.13	64.27	63.24	60.92
260	-29.50	111.48	103.59	62.12	64.73	64.55	66.88	61.28	62.75
270	-33.05	125.64	129.08	61.03	60.85	65.66	62.14	64.08	57.54
280	-29.57	135.54	158.82	61.88	63.16	62.20	64.30	56.58	59.20
290	-33.20	144.39	191.04	61.97	59.63	64.00	59.52	58.93	54.92
300	-29.98	159.61	229.85	61.25	63.40	60.85	61.19	55.79	58.47
310	-33.54	193.02	257.47	59.59	59.52	59.66	56.04	50.22	55.87
320	-30.21	217.28	262.44	59.58	62.38	55.32	58.95	52.39	61.09
330	-33.75	219.87	269.23	57.31	59.13	50.73	55.60	48.00	58.61
340	-30.49	213.55	295.41	61.81	62.82	56.98	58.91	58.58	61.80
350	-33.73	225.48	327.32	54.50	58.78	51.39	54.78	53.93	57.93
360	-30.55	249.00	352.02	61.06	61.33	56.20	56.48	59.95	60.24
370	-33.55	265.37	340.45	56.16	58.86	53.09	52.54	54.89	56.97
380	-30.71	261.21	392.20	60.27	60.70	55.33	56.76	58.21	59.67
390	-33.27	287.87	366.17	55.50	58.31	51.35	56.52	53.88	58.51

B.6 Raw data of the Measurement Group 6

Table B.6: Measurement data of the first group: transmitting antenna at h=2m, vertical polarization.

MHz	Power	Re(Z)	Im(Z)	M 1m	S 1m	M 1.5m	S 1.5m	M 2m	S 2m
90	-31.88	175.35	-659.38	35.67	31.94	35.15	30.54	36.68	29.64
100	-27.91	214.14	-545.65	38.65	38.06	41.23	36.78	43.10	37.33
110	-32.00	133.23	-567.36	33.35	35.02	37.54	34.58	39.69	36.76
120	-28.23	167.00	-456.51	40.77	42.42	44.11	42.96	46.23	45.13
130	-31.86	165.12	-457.70	35.92	41.01	41.82	42.02	42.88	43.82
140	-28.35	77.74	-430.11	44.50	47.56	48.40	48.97	49.99	50.45
150	-31.91	76.23	-334.72	38.35	47.50	46.14	49.13	46.94	50.43
160	-28.48	83.01	-296.76	49.58	52.73	54.56	54.66	55.43	55.83
170	-32.29	73.31	-256.87	45.11	51.02	51.71	53.40	51.06	53.90
180	-28.39	68.41	-219.46	53.21	56.76	59.53	59.53	59.82	59.50
190	-32.91	58.86	-179.83	52.34	54.01	57.64	57.22	55.77	56.68
200	-28.70	54.09	-134.73	59.89	61.56	63.93	64.04	61.38	62.10
210	-32.90	53.83	-90.90	59.06	60.86	61.55	62.37	56.79	59.00
220	-28.89	59.52	-44.29	66.28	67.79	66.44	67.92	61.03	64.59
230	-32.90	72.30	-4.07	64.79	64.23	64.04	63.87	60.10	61.90
240	-29.20	82.67	30.56	66.74	66.92	64.68	66.54	63.77	66.06
250	-32.90	91.95	68.15	63.80	62.49	62.59	61.49	62.43	61.49
260	-29.50	108.64	104.36	63.79	65.68	61.01	63.82	62.55	63.66
270	-33.05	124.54	134.79	63.22	61.35	63.02	58.93	62.32	60.28
280	-29.57	138.11	159.26	61.83	63.88	58.02	60.62	61.60	64.04
290	-33.20	143.43	192.34	62.62	59.17	58.38	56.69	60.65	59.41
300	-29.98	163.42	234.04	60.80	61.61	57.20	59.17	60.04	61.61
310	-33.54	196.13	249.03	59.79	57.37	52.47	55.54	57.56	58.76
320	-30.21	205.68	260.29	57.64	60.11	54.02	60.48	57.16	62.22
330	-33.75	212.14	279.06	56.08	56.32	48.77	57.91	53.93	57.69
340	-30.49	216.30	305.47	59.72	59.63	58.73	60.88	60.83	59.62
350	-33.73	229.64	338.68	51.61	55.84	53.95	56.85	52.58	55.39
360	-30.55	274.69	354.54	56.80	58.03	60.32	59.04	57.16	57.60
370	-33.55	266.08	338.83	51.89	54.62	54.91	56.26	52.85	54.88
380	-30.71	254.15	362.46	55.87	57.06	58.87	59.58	55.37	58.93
390	-33.27	258.98	398.92	50.96	54.34	54.25	57.98	52.85	56.89

Bibliography

[AC04] D. Andreis and E. S. Canuto. Orbit dynamics and kinematics with full quaternions. In *American Control Conference, 2004. Proceedings of the 2004*, pages 3660–3665 vol.4. IEEE, 2004.

[Age07] US National Security Agency. TEMPEST: A signal problem, 2007.

[AK07] B. Auchmann and S. Kurz. The pairing matrix in discrete electromagnetism. *The European Physical Journal Applied Physics*, 39(2):133–141, June 2007.

[Bal05] C. A. Balanis. *Antenna theory (Third edition).* Wiley, 2005.

[Bas03] U. Basu. Perfectly matched layers for time-harmonic elastodynamics of unbounded domains: theory and finite-element implementation. *Computer Methods in Applied Mechanics and Engineering*, 192(11-12):1337–1375, March 2003.

[Ber94] J. P. Berenger. A perfectly matched layer for the absorption of electromagnetic waves. *Journal of Computational Physics*, 114(2):185–200, 1994.

[BO08] N. Bell and L. N. Olson. Algebraic multigrid for k-form Laplacians. *Numerical Linear Algebra with Applications*, 15(2-3):165–185, 2008.

[Bon15] J Bonelle. *Compatible Discrete Operator schemes on polyhedral meshes for elliptic and Stokes equations.* PhD thesis, Université Paris-Est, January 2015.

[Bos98a] A. Bossavit. *Computational electromagnetism. Variational formulations, Complementarity, Edge elements.* Academic Press, 1998.

[Bos98b] A. Bossavit. On the geometry of electromagnetism : (4): Maxwell's house. *Journal of the Japan Society of Applied Electromagnetics*, 6(4):318–326, December 1998.

[Bos01] A. Bossavit. 'Generalized Finite Differences' in Computational Electromagnetics. *Progress In Electromagnetics Research*, 32:45–64, 2001.

[BP81] G. J. Burke and A. J. Poggio. Numerical Electromagnetics Code (NEC) - Method of Moments. 1981.

[CBC+14] C. F. M. Carobbi, A. Bonci, M. Cati, C. Panconi, M. Borsero, and G. Vizio. Design, Preparation, Conduct, and Result of a Proficiency Test of Radiated Emission Measurements. *IEEE Transactions on Electromagnetic Compatibility*, 56(6):1251–1261, 2014.

[CCC+15a] S. Chialina, M. Cicuttin, L. Codecasa, G. Solari, R. Specogna, and F. Trevisan. Modeling of anechoich chambers with equivalent materials and equivalent sources. *IEEE Transactions on Electromagnetic Compatibility, In press*, 2015.

[CCC+15b] S. Chialina, M. Cicuttin, L. Codecasa, R. Specogna, and F. Trevisan. Plane Wave Excitation for Frequency Domain Electromagnetic Problems by Means of Impedance Boundary Condition. *IEEE Transactions on Magnetics*, 51(3), 2015.

[CCST16a] M. Cicuttin, L. Codecasa, R. Specogna, and F. Trevisan. Complementary discrete geometric h-field formulation for wave propagation problems. *IEEE Transactions on Magnetics*, 52(3), 2016.

[CCST16b] M. Cicuttin, L. Codecasa, R. Specogna, and F. Trevisan. Excitation by scattering/total field decomposition and Uniaxial PML in the geometric formulation. *IEEE Transactions on Magnetics*, 52(3), 2016.

[CDST10] L. Codecasa, P. Dular, R. Specogna, and F. Trevisan. Time-Domain Geometric Eddy-Current A Formulation for Hexahedral Grids. *IEEE Transactions on Magnetics*, 46(8):3301–3304, 2010.

[CGG+13] M. Chanaud, L. Giraud, D. Goudin, J. J. Pesqué, and J. Roman. A parallel full geometric multigrid solver for time harmonic maxwell problems. 2013.

[Che14] W. C. Chew. Vector Potential Electromagnetics with Generalized Gauge for Inhomogeneous Media: Formulation (Invited Paper). *Progress In Electromagnetics Research*, 149:69–84, 2014.

[CIS08a] CISPR 16-4-2:2011 Specification for radio disturbance and immunity measuring apparatus and methods - Part 4-2: Uncertainties, statistics and limit modelling - Measurement instrumentation uncertainty, 2008.

[CIS08b] IEC CISPR25:2008 - Vehicles, boats and internal combustion engines - Radio disturbance characteristics - Limits and methods of measurement for the protection of on-board receivers, 2008.

[Cod14] L. Codecasa. Refoundation of the Cell Method Using Augmented Dual Grids. *IEEE Transactions on Magnetics*, 50(2):497–500, February 2014.

[Col] R. E. Collin. *Foundations for Microwave Engineering.* McGraw-Hill.

[CS08] L. Codecasa and R. Specogna. Discrete constitutive equations over hexahedral grids for eddy-current problems. *CMES: Computer Modeling ...*, 2008.

[CS10] V Chrisitianto and F. Smarandache. A derivation of Maxwell equations in quaternion space. *Progress in Physics*, 2:23–27, 2010.

[CST07] L. Codecasa, R. Specogna, and F. Trevisan. Symmetric Positive-Definite Constitutive Matrices for Discrete Eddy-Current Problems. *IEEE Transactions on Magnetics*, 43:510–515, February 2007.

[CST10a] L. Codecasa, R. Specogna, and F. Trevisan. A new set of basis functions for the discrete geometric approach. *Journal of Computational Physics*, 229(1):7401–7410, September 2010.

[CST10b] L. Codecasa, R. Specogna, and F. Trevisan. Constitutive Relations for Discrete Geometric Approach Over Hexahedral Grids. *IEEE Transactions on Magnetics*, 46(8):3077–3080, July 2010.

[CST12] L. Codecasa, R. Specogna, and F. Trevisan. Discrete Geometric Formulation of Admittance Boundary Conditions for Frequency Domain Problems Over Tetrahedral Dual Grids. *IEEE Transactions on Antennas and Propagation*, 60(8):3998–4002, 2012.

[CT05] L. Codecasa and F. Trevisan. Piecewise uniform bases and energetic approach for discrete constitutive matrices in electromagnetic problems. *International Journal for Numerical Methods in Engineering*, 65(4):548–565, 2005.

[CW02] M. Clemens and T. Weiland. Regularization of eddy-current formulations using discrete grad-div operators. *IEEE Transactions on Magnetics*, 38(2):569–572, March 2002.

[CZPM92] J. M. Cooke, M. Zyda, D. R. Pratt, and R. B. McGhee. NPSNET: Flight Simulation Dynamic Modeling Using Quaternions. *Presence*, 1(4):404–420, 1992.

[DL96] S. De Leo. Quaternions and special relativity. *Journal of Mathematical Physics*, 37(6):2955–2968, June 1996.

[DS10] P. Dlotko and R. Specogna. Efficient Cohomology Computation for Electromagnetic Modeling. *Cmes-Computer Modeling in Engineering & Sciences*, 60(3):247–278, May 2010.

[GHJV94] E. Gamma, R. Helm, R. Johnson, and J. Vlissides. *Design Patterns: Elements of Reusable Object-Oriented Software*. Addison Wesley, 1994.

[GTB94] N. A. Golias, T. D. Tsiboukis, and A. Bossavit. Constitutive Inconsistency - Rigorous Solution of Maxwell Equations Based on a Dual Approach. *IEEE Transactions on Magnetics*, 30(5):3586–3589, September 1994.

[Hol83] R. Holland. Finite-difference solution of maxwell's equations in generalized nonorthogonal coordinates. *Nuclear Science, IEEE Transactions on*, 30(6):4589–4591, 1983.

[ISO05] ISO/IEC 17025:2005 - General requirements for the competence of testing and calibration laboratories, 2005.

[ISO08] ISO 11452:2012 - Component test methods for electrical disturbances from narrowband radiated electromagnetic energy, 2008.

[Jac03] P. M. Jack. Physical Space as a Quaternion Structure, I: Maxwell Equations. A Brief Note. *arXiv.org*, page 7038, July 2003.

[Joi08] Joint Committee for Guides in Metrology. Guide to the expression of uncertainty in measurement. 2008.

[JY07] Chen J. and Wen Y. Simulation of the field uniformity of anechoic chamber. In *Microwave, Antenna, Propagation and EMC Technologies for Wireless Communications, 2007 International Symposium on*, pages 1349–1352, August 2007.

[LT06] B. Lee and C. Tong. A novel algebraic multigrid-based approach for Maxwell's equations. *Preprint UCRL-JC-218750*, 2006.

[Mar08] R. C. Martin. *Clean code - A Handbook of Agile Software Craftmanship*. Prentice Hall, 2008.

[Mat97] C. Mattiussi. An analysis of finite volume, finite element, and finite difference methods using some concepts from algebraic topology. *Journal of Computational Physics*, 133(2):289–309, 1997.

[Max91] J. C. Maxwell. *A treatise on electricity and magnetism*. Clarendon Press, 1891.

[Mid03] M. Midrio. *Campi Elettromagnetici*. SGEditoriali, 2003.

[MK14] I. Munteanu and R. Kakerow. Simulation Methodology for the Assessment of Field Uniformity in a Large Anechoic Chamber. *IEEE Transactions on Magnetics*, 50(2):213–216, 2014.

[MNN09] F. Musy, A. Napov, and Y. Notay. Krylov-based algebraic multigrid for edge elements. In *Proceedings of the ...*. HAL - CCSD, 2009.

[Muk02] R. Mukundan. Quaternions: From classical mechanics to computer graphics, and beyond. In *Proceedings of the 7th Asian Technology ...*, 2002.

[MYW14] Y. Ma, J. Yu, and Y. Wang. A novel unsplit perfectly matched layer for the second-order acoustic wave equation. *Ultrasonics*, 54(6):1568–1574, August 2014.

[NAS95] NASA. Electronic Systems Failures and Anomalies Attributed to Electromagnetic Interference. Reference Publication no. 1374, 1995.

[Not10] Y. Notay. An Aggregation-Based Algebraic Multigrid Method. *Electronic Transactions on Numerical Analysis*, 37:123–146, 2010.

[NSAA09] H. Nornikman, P.J. Soh, A.A.H. Azremi, and M.S. Anuar. Performance simulation of pyramidal and wedge microwave absorbers. In *Modelling Simulation, 2009. AMS '09. Third Asia International Conference on*, pages 649–654, May 2009.

[Pap88] C.H. Papas. *Theory of electromagnetic wave propagation*. Dover, 1988.

[PGHS15] Y. Paquay, C. Geuzaine, M. Hasan, and R. Sabariego. Reduced order model for accounting for high frequency effects in power electronic components. *Magnetics, IEEE Transactions on*, PP(99):1–1, 2015.

[RBF88] J. Rikabi, C. F. Bryant, and E. M. Freeman. Error-Based Derivation of Complementary Formulations for the Eddy-Current Problem. *IEEE Proceedings A - Science Measurement and Technology*, 135(4):208–216, April 1988.

[RQ10] Z. Ren and H. Qu. Investigation of the Complementarity of Dual Eddy Current Formulations on Dual Meshes. *IEEE Transactions on Magnetics*, 46(8):3161–3164, August 2010.

[San10] C. Sanderson. Armadillo: An Open Source C++ Linear Algebra Library for Fast Prototyping and Computationally Intensive Experiments. Technical report, NICTA, 2010.

[SF13] W. Shin and S. Fan. Accelerated solution of the frequency-domain Maxwell's equations by engineering the eigenvalue distribution of the operator. *Optics Express*, 21(19):22578–18, 2013.

[Smu90] P. Smulders. The threat of information theft by reception of electromagnetic radiation from RS-232 cables. *Computers & Security*, 9(1):53–58, February 1990.

[Spe10] R. Specogna. Complementary geometric formulations for electrostatics. *International Journal for Numerical Methods in Engineering*, 86(8):1041–1068, December 2010.

[Spe13] R. Specogna. Extraction of VLSI Multiconductor Transmission Line Parameters by Complementarity. *IEEE Transactions on Very Large Scale Integration (VLSI) Systems*, 22(1):146–154, December 2013.

[Spe15] R. Specogna. One Stroke Complementarity for Poisson-Like Problems. *IEEE Transactions on Magnetics*, 51(3):1–4, April 2015.

[SST08] R. Specogna, S. Suuriniemi, and F. Trevisan. GeometricT-Ω approach to solve eddy currents coupled to electric circuits. *International Journal for Numerical Methods in Engineering*, 74:101–115, April 2008.

[SSW02] R. Schuhmann, P. Schmidt, and T. Weiland. A new whitney-based material operator for the finite-integration technique on triangular grids. *Magnetics, IEEE Transactions on*, 38(2):409–412, March 2002.

[ST08] R. Specogna and F. Trevisan. Eddy-Currents Computation With T-Omega Discrete Geometric Formulation for an NDE Problem. *IEEE Transactions on Magnetics*, 44:698–701, June 2008.

[SW98] R. Schuhmann and T. Weiland. Stability of the fdtd algorithm on nonorthogonal grids related to the spatial interpolation scheme. *Magnetics, IEEE Transactions on*, 34(5):2751–2754, September 1998.

[Swa08] D.D. Swanson. Analysis of mil-std-461e and mil-std-461f re102 test setup configurations below 100 mhz. In *Electromagnetic Compatibility, 2008. EMC 2008. IEEE International Symposium on*, pages 1–11, August 2008.

[Syn57] J. L. Synge. *The Hypercircle in Mathematical Physics*. Cambridge University Press, 1957.

[Taf98] A. Taflove. *Advances in Computational Electrodynamics*. Artech House Publishers, 1998.

[TK06] F. Trevisan and L. Kettunen. Geometric interpretation of finite-dimensional eddy-current formulations. *International Journal for Numerical Methods in Engineering*, 67(13):1888–1908, 2006.

[TKB99] T. Tarhasaari, L. Kettunen, and A. Bossavit. Some realizations of a discrete Hodge operator: a reinterpretation of finite element techniques [for EM field analysis]. *IEEE Transactions on Magnetics*, 35(3):1494–1497, May 1999.

[Ton75] E. Tonti. On the formal structure of physical theories, 1975.

[Ton00] E. Tonti. Formulazione finita dell'elettromagnetismo partendo dai fatti sperimentali, 2000.

[Ton01] E. Tonti. A direct discrete formulation of field laws: The cell method. *CMES- Computer Modeling in Engineering and ...*, 2001.

[Ton06] E. Tonti. *Gradiente, Rotore, Divergenza*. Pitagora Editrice Bologna, 2006.

[Ton14] E. Tonti. Why starting from differential equations for computational physics? *Journal of Computational Physics*, 257:1260–1290, January 2014.

[TV03] F. Trevisan and F. Villone. *Modelli Numerici per Campi e Circuiti*. SGE Editoriali, 2003.

[TVT+15] B. Thierry, A. Vion, S. Tournier, M. El Bouajaji, D. Colignon, N. Marsic, X. Antoine, and C. Geuzaine. GetDDM: an Open Framework for Testing Optimized Schwarz Methods for Time-Harmonic Wave Problems. 2015.

[VE85] W. Van Eck. Electromagnetic radiation from video display units: an eavesdropping risk? *Computers & Security*, 4(4):269–286, December 1985.

[Vin11] J. Vince. *Quaternions for computer graphics*. Springer, 2011.

[Wei01] T. Weiland. Discrete electromagnetism with the finite integration technique. *Progress In Electromagnetics Research*, 2001.